UNIVERSITY OF CALIFORNIA, SAN DIEGO

Performance of steel-polymer and ceramic-polymer layered composites and concrete under high strain rate loadings

A dissertation submitted in partial satisfaction of the
requirements for the degree
Doctor of Philosophy

in

Engineering Sciences (Mechanical Engineering)

by

Ahsan Samiee

Committee in charge:

Professor Siavouche Nemat-Nasser, Chair
Professor Philip E. Gill
Professor Eric Lauga
Professor Tom Liu
Professor Hidenori Murakami

2010

The dissertation of Ahsan Samiee is approved, and it is acceptable in quality and form for publication on microfilm and electronically:

_____

_____

_____

_____

_____
Chair

University of California, San Diego

2010

DEDICATION

To my parents: Forough and Ahmad

EPIGRAPH

"Human being are members of a whole,

In creation of one essence and soul.

If one member is afflicted with pain,

Other members uneasy will remain.

If you've no sympathy for human pain,

The name of human you cannot retain!"

by Saadi (12th century Persian poet), translated by M. Aryanpoor

picture from the entrance of the United Nations building in New York

TABLE OF CONTENTS

LIST OF FIGURES

LIST OF TABLES

ACKNOWLEDGEMENTS

First and foremost, I would like to express my deepest appreciation to my advisor, Professor Sia Nemat-Nasser, for his great support and incredible inspiration. I thank him for his invaluable lessons in research and most importantly, in life. I am extremely grateful to Mr. Jon Isaacs for the extensive amount of time, effort, and expertise he has contributed to my research. He was incredibly supportive at the hardest of times, and he made my stay at CEAM an enjoyable and memorable experience. I would also like to acknowledge my committee members, Professors Philip Gill, Eric Lauga, Thomas Liu, and Hidenori Murakami, for their insight.

I would like to especially thank Lauri Jacobs-Cohantz for her constant help during my Ph.D. studies. I sincerely appreciate the collaborations and help of my fellow CEAM members: Christian Nielsen, Dr. Ankit Srivastava, Dr. Alireza Amirkhizi, Dr. Kristin Schaaf, Dr. Mahmoud R. Amini and Aref Tehranian. Without their help and support, the completion of this work would not have been possible.

Chapter 2 is prepared for publication by A. Samiee, A. V. Amirkhizi and S. Nemat-Nasser. The dissertation author is the primary investigator and author of this chapter.

Chapter 3 is prepared for publication by A. Samiee, J. Isaacs and S. Nemat-Nasser. The dissertation author is the primary investigator and author of this chapter.

Chapter 5 is prepared for publication by A. Samiee, A. Srivastava and S. Nemat-Nasser. The dissertation author is the primary investigator and author of this chapter.

Chapter 6 is prepared for publication by A. Samiee, J. Isaacs, J. Magallanes and S. Nemat-Nasser. The dissertation author is the primary investigator and author of this chapter.

With the exception of chapters 5 and 6, this work has been supported by the ONR grant N00014-06-1-0340 to the University of California, San Diego. The work of chapter 6 was funded by Karagozian & Case (K&C) Company. I gratefully acknowledge the contribution of Mr. Joe Magallanes from K&C to this project.

And finally, I would like to thank my family and friends who have always been there for me, whenever I needed help. I am grateful for their support, and all the love and happiness we share.

VITA

2003	Bachelor of Science in Mechanical Engineering, Sharif University of Technology, Tehran, Iran
2006	Master of Science in Mechanical Engineering, Villanova University, Villanova, PA
2010	Business Technology Creation Certificate University of California, San Diego — Extension
2010	Doctor of Philosophy in Engineering Sciences (Mechanical Engineering), University of California, San Diego

PUBLICATIONS

JOURNALS

R. Theilmann, T. J. Arai, A. Samiee, D. Dubowitz, S. Hopkins, R. Buxton, K. G. Prisk. Quantitative MRI measurement of lung density must account for the change in T_2^* with lung inflation. *Journal of Magnetic Resonance Imaging*, 30(3):527-534, 2009.

PROCEEDINGS

A. Samiee, A. Amirkhizi, S. Nemat-Nasser. Performance of polymer-steel bi-layers under blast.*SEM Annual Conference & Exposition on Experimental and Applied Mechanics*, Indianapolis, IN, 2010.

A. Samiee, J. Isaacs, S. Nemat-Nasser. A Numerical and Experimental Study of High Strain-rate Compression and Tension Response of Concrete. *SEM Annual Conference & Exposition on Experimental and Applied Mechanics*, Indianapolis, IN, 2010.

A. Samiee, J. Issacs, S. Nemat-Nasser. Performance of polymer-steel sandwich structures under impact loadings. *International Conference on Computational & Experimental Engineering and Sciences*, Las Vegas, NV, 2010

A. Samiee, J. Isaacs, and S. Nemat-Nasser. Ballistic performance of polyurea-coated armor grade ceramic tiles. *Proc. SPIE*, 7644, 76441Y, 2010.

A. Samiee, J. Isaacs, and S. Nemat-Nasser. Performance of polymer-steel sandwich structures under blast loads. *Proc. SPIE*, 7287, 72872E, 2009.

A. Samiee and M. Raulli. Reliability based design optimization of magneto-structural problems. *The 7th World Congress on Computational Mechanics*, Los Angeles, CA, 2006.

STUDYFIELDS

Major Field: **Engineering Sciences (Mechanical Engineering)**

Studies in **Solid Mechanics**
Professors S. Nemat-Nasser, H. Murakami and S. Santhanam

Minor Field: **Numerical Methods**

Studies in **FEM and CFD**
Professors H. Murakami, D. Benson, R. Hoffman, T. Bewley and G. Jones

Studies in **Numerical Methods and Optimization**
Professors P. Gill, T. Bewley, C. Pozrikidis and M. Raulli

Other Fields:

Studies in **Biomedical Imaging and Lung Physiology**
Professors T. Liu, S. Hopkins and R. Rizi

Studies in **Entrepreneurship and Marketing**
Dr. A. Zack, Mr. T. Somasundaram, Dr. D. Connolly, Dr. S. Eremenko and Mr. B. Hawkins

ABSTRACT OF THE DISSERTATION

Performance of steel-polymer and ceramic-polymer layered composites and concrete under high strain rate loadings

by

Ahsan Samiee

Doctor of Philosophy in Engineering Sciences (Mechanical Engineering)

University of California, San Diego, 2010

Professor Siavouche Nemat-Nasser, Chair

In this thesis, experimental and numerical techniques are employed to investigate the possibility of improving the impact- and blast-resistance of composite structures. Finite element models are developed to study the dynamic response and large deformation of steel-polyurea bi-layers. A Split Hopkinson Pressure Bar (SHPB) setup is used to perform impact tests on steel-polyurea-steel sandwich structures. The SHPB experiments are simulated by FEM to explore the deformation history, failure, and fracture of these structures. Penetration tests are conducted to assess the ballistic performance of steel- and ceramic-polyurea layered

composites. In addition, an approximate solution to the problem of wave propagation in cylindrical layered composites is analytically obtained. A semi-analytical method for dispersion correction of traveling waves in layered cylinders is developed and verified by FEM. The SHPB is also employed to characterize the high strain rate behavior of concrete in compression and tension. A finite element model is developed to address confusions about sample size and friction effects.

Chapter 1

Introduction

1.1 Background

Steel plates and metal sheets have been essential elements of major industries offering a broad range of applications in automotive, aerospace, defense, marine, and heavy industries, to name a few. Vehicle bodies, ship hulls, aircraft fuselages and wings, pressure vessel shells, and many other components of the modern industrial world are manufactured from sheets of metal based alloys. Steel plates have been employed to strengthen, reinforce, and cover the core of structures, protecting them from expected or unexpected external forces and loads. In many cases, sophisticated flaw detection procedures are routinely carried out on these parts to avoid possible catastrophic events (e.g. in the case of airplanes).

The substantial role of the metal sheets in reinforcement and structural protection has motivated many researchers in structural, mechanical and material sciences to investigate the performance and deformation of steel plates subjected to various types of loading, aiming towards stronger and lighter alloys and configurations. Numerous kinds of metal based alloys have been developed to improve the

mechanical properties of metal sheets and steel plates. Additionally, the advent of composite materials and structures has opened a new horizon of opportunities in designing more effective and reliable protective shells and structures. Various experimental, theoretical, and numerical studies have been conducted to characterize the dynamic response and fracture of the steel plates under impulsive loadings.

In a two-part review article, Nurick and Martin [2, 3] have summarized the theoretical and experimental attempts prior to 1988, which focused on the deformation of steel plates subjected to impulsive loadings. The early theoretical methods only considered the *bending action* and failed to predict large deformations [4, 5]. Better estimates emerged when the *stretching action* was taken into account [6, 7]. In these studies, various mode shapes were assumed and the final deflection profile of the deformed steel plate was sought using a variety of approaches; *e.g.* energy methods, eigenvalue solutions of boundary value problems, etc. Further experimental attempts revealed different failure modes of simply clamped steel plates subjected to impulsive loadings [8, 9].

The deflection, failure, and fracture performance of the steel plates subjected to impulsive loadings can be improved by adding highly dissipative materials to the system. Xue and Hutchinson [10] have noticed an increase in the necking limits and energy absorption of metal-polymer circular bi-layers subjected to quasi-static and dynamic loadings. In a systematic experimental and numerical study, Amini *et. al.* [11, 12, 13, 14] reported a significant improvement to the performance of steel plates with 1 mm thickness and 3-inch diameter, when coated with polyurea on the back side (opposite to the load-receiving side). Xue *et. al.* [15] have conducted penetration tests on steel-polyurea composites using flat and pointed projectiles. Supported by their numerical calculations, they reported an enhancement in energy absorption when a layer of polyurea is placed on the

back. They also did not notice any significant benefit for steel-polyurea-steel sandwich composites. In a numerical effort, Bahei-El-Din *et. al.* [16] added a polyurea inter-layer into a sandwich structure and reported a significant improvement in the response of the structure to blast loads.

In this thesis, experimental and numerical techniques are employed to further investigate the performance of steel-polyurea composites of various configurations,*i.e.* bi-layers, sandwich structures, and layered composites, subjected to ballistic and impulsive loadings. Additionally, penetration tests have been conducted to investigate the ballistic performance of ceramic-polyurea composites. This thesis also addresses the propagation of impulsive pulses in layered composites.

1.2 Tools and Methodology

In this study, we have used various experimental and numerical tools. The explicit Finite Element Method (FEM) is extensively employed for our numerical simulations. A commercially available software package, LS-DYNA, was adopted as our FEM solver to carry out the computations. LS-DYNA's user-defined material model capabilities have allowed us to use our in-house material models for the polyurea (developed by Amirkhizi *et. al.* [17]) and the *DH-36* steel (developed by Nemat-Nasser and Guo [18]). FEM models have been mostly generated using Altair® Hypermesh. Some models have been manually created by codes written in Matlab. Post-processing of FEM results has been carried out using LS-PrePost and our in-house codes, which have been written using Python and Matlab.

We have used a 3-inch Split Hopkinson Pressure Bar (SHPB) setup to perform impact experiments on steel-polyurea-steel sandwich structures. Our experiments on ceramic-polyurea and steel-polyurea layered composites have been

performed at UCSD/CEAM's gas gun laboratory that can create high-velocity impacts ($\sim$ 900 m/s in our case).

1.3 Goals and Achievements

1.3.1 Improving the impact-resistance of steel plates

In a comprehensive numerical study, we have shown that polyurea can improve the impact-resistance of steel plates when coated on the back (not the load-receiving side). Although different in dimensions, our results agree with the results reported by other researchers [11, 12, 13, 14].

1.3.2 Better protection against blast and impact

Our experimental and numerical study on steel-polyurea-steel composites reveals that this sandwich structure can provide better protection against impulsive loadings than comparable steel-only systems. We have observed that the steel plate on the back acts as a sacrificial layer and fractures, while the steel plate on the front remains intact. The steel-only structure fractured when subjected to the same impulsive loading.

1.3.3 Improving the blast-resistance of layered-composites

We have performed penetration tests on ceramic-polyurea and steel-polyurea layered composites to investigate their ballistic performance. We have observed that the ballistic-resistance of steel plates and ceramic tiles improved when coated by polyurea. However, the enhancement is not as significant as the improvements reported by other researchers (see the article by Sarva *et. al.* [19]).

1.3.4 Filtering high-frequency content of pressure pulses

In a semi-analytical effort, we have solved the problem of wave propagation in layered cylindrical bars. This structure can effectively filter certain ranges of frequency content of the traveling pulse. We have employed FEM to verify the accuracy of our solution.

1.3.5 Characterizing the high strain rate response of concrete in tension and compression

Split Hopkinson Pressure Bar is employed to conduct experiments on concrete under compression and tension. The rate-dependency of concrete is observed and reported. FEM models have been developed to clarify the confusions about sample size and friction effects.

1.4 Manuscript Organization

This manuscript is organized in the following manner. In chapter 2, the FEM simulations on circular steel-polyurea bi-layers are presented. The steel plates have a diameter of 1.0 m and the thickness of 1.0 cm. Various thicknesses of polyurea are considered, and the effect of polyurea thickness on the performance of the resulting bi-layers is investigated. For each thickness of polyurea, three scenarios are modeled: 1) polyurea cast on the front (load-receiving side), 2) polyurea cast on the back, and, 3) no polyurea, with an increase in the steel plate thickness to match the areal density of the corresponding bi-layers.

Chapter 3 presents the experimental and numerical attempts to investigate the performance of steel-polyurea-steel composites subjected to impulsive loadings.

A Hopkinson bar setup is employed to carry out experiments on circular sandwich samples with 3-inch diameters. The thickness of each steel plate is 1 mm and the thickness of the polyurea layer is 3.8 mm. The entire experimental process is simulated in LS-DYNA to investigate the deformation history and fracture modes in depth. Finally, an axi-symmetric finite element model is presented that focuses on sandwich structures with larger dimensions.

Chapter 4 details our penetration tests on ceramic-polyurea and steel-polyurea layered composites. In these experiments, $\frac{1}{2}$-inch ceramic tiles coated with polyurea are penetrated by flat-ended projectiles with velocities of approximately 900 m/s. The kinetic energy reduction of the projectiles are measured as a metric to evaluate the ballistic performance of the composites. The same experimental procedure is also carried out on steel-polyurea layered composites. Samples with various thicknesses of steel and polyurea are fabricated and tested.

In chapter 5, an approximate solution to the wave propagation problem in layered cylindrical bars is presented. The dispersion curve for an example problem is calculated. A numerical procedure is proposed to correct for dispersion effects occurring in the layered medium. The solution is then compared to the results of the FEM simulation of the example to verify the accuracy and validity of the presented approach.

In Chapter 6, I report the results from our unconfined compression and tension tests on concrete samples. A Split Hopkinson Pressure Bar setup is employed to carry out the compression experiments. Proposed by Mr. Jon Isaacs, the experimental setup was modified for the tension experiments. Finite elements models are also presented in this chapter addressing issues such as sample size and friction effects.

Chapter 2

Performance of Steel-Polyurea Bi-layers Subjected to Impulsive Loadings

In this chapter, we present results from our numerical simulations of the dynamic response and deformation of 1-meter diameter circular DH-36 steel plates and steel-polyurea bi-layers, subjected to impulsive loadings. Different thicknesses of polyurea are considered, and the effect of polyurea thickness on the performance of the steel plates under high-rate loadings is investigated. For each polyurea thickness, we have simulated three cases: 1) polyurea cast on the front face (load-receiving side); 2) polyurea cast on the back face; and, 3) no polyurea but an increase in steel-plate thickness, such that the areal density remains the same in all three cases. Two types of loading are applied to the polyurea-steel system: (1) direct application of pressure on the bi-layer system, (2) application of pressure through a separate medium (polyurethane or water); where the differences are demonstrated and discussed throughout the scope of the present manuscript. For the

numerical simulations, we have used physics-based and experimentally-supported temperature- and rate-sensitive constitutive models for steel and polyurea.

Results from the simulations reveal that in all cases, polyurea cast on the back face demonstrates superior performance relative to the other two cases. The differences become more pronounced as polyurea thickness (and the corresponding steel-plate thickness) becomes greater. Also, the differences become less pronounced when direct pressure is applied.

2.1 Introduction

The dynamic response of steel plates and metal sheets to high-rate loadings has been a topic of interest for many years. Numerous applications of steel plates in defense, marine, aviation and car industries have called for a thorough investigation on the failure and fracture of steel plates under various types of loading. Numerous analytical, experimental and numerical approaches have been employed to comprehend the details of this problem.

The first experimental and theoretical attempts to address this problem emerged when Taylor [20] and Richardson and Kirkwood [21] investigated the plastic deformation of thin steel plates subjected to underwater explosions. These attempts were followed by experimentalists who carried out tests on circular membranes [22, 23, 24]. These approaches were mainly focused on measuring and predicting the final deflection profile of the circular plates. For more detailed discussion on the development of this topic, the reader is referred to the reviews published on dynamic plastic behavior of steel plates by Nurick and Martin [25, 24].

Early attempts considered only bending effects that could only predicted small deflections. When the steel plate experiences large deformations, however,

the dynamic response is associated with excessive stretching of the membrane. Several methods have been proposed to solve the resulting initial-boundary value problem. Some researchers have assumed several mode shapes and equated the dissipated strain energy to the initial kinetic energy to obtain the final deflection profile [26]. Others have proposed and solved eigenvalue problems to calculate the stationary mode shapes [27]. Wierzbicki and Nurick [28] combined the mode shape and eigenvalue solutions to arrive to a good match to experimental results. Lee and Wierzbicki [29, 30] predicted the transient response and fracture of thin plates to explosive loading with various spacial and temporal distributions, and intensity of applied loads by analytical and numerical methods.

The advances in numerical techniques such as Finite Element Method (FEM) have largely contributed to the understanding of many real-world problems. In the case of dynamic response of steel plates, analytical methods make various simplifying assumptions on governing equations, types of loading, boundary conditions, plastic response of materials, etc. Nevertheless, an FEM model can treat all the non-linearities with a measurable error margin while solving governing equations without ignoring any term. Balden and Nurick [31] employed FEM to simulate the post-failure motion of steel plates subjected to blast loading. Neuberger et al. [32] estimated the spring-back of circular clamped armor steel plates subjected to spherical air-blast loading.

It has been shown that coating steel plates with layers of energy dissipating materials (such as polymers) can improve the impact resistance of steel plates. In an extensive experimental and numerical study, Amini et al. [33, 34, 35, 36] have shown that steel plates with a layer of *polyurea* coated on the back (with respect to the impulsive loading) delays the necking and fracture; unlike front coated plates where the shock is magnified and failure is promoted. In that study, only 3-inch

diameter circular steel plates with 1-mm thickness were considered, and the conclusions were limited to that scale. Polyurea is a well-known reaction and abrasion resistant polymer and has been extensively used in coating industry (e.g. tunnels, bridges, roofs, truck beds, etc.). In addition to its coating applications, polyurea has demonstrated exceptional mechanical and chemical properties leading to its applications in armor and automotive industries. For example, polyurea has been employed to increase the resistance of military armor to ballistic loads [37]. Xue and Hutchinson [38] have investigated the neck retardation and enhanced energy absorption in metal-polyurea bi-layers. Amirkhizi et al. [39] have systematically studied the viscoelastic properties of polyurea over a wide range of strain rates and temperatures. Based on this study, a pressure, temperature, and strain-rate sensitive model has been developed and implemented into LS-DYNA, a commercial finite element package.

In this numerical study, the dynamic response of circular steel plates with and without a layer of polyurea to impulsive loadings is investigated. Different thicknesses of polyurea are considered, and the position of polyurea with respect to impulsive loading is also alternated; i.e. polyurea is either placed on the side facing the loading, or on the opposite side of the plate. The finite element simulations are conducted by LS-DYNA, with user-defined material models. For polyurea, the model by Amirkhizi et al. [39] is employed and for steel plates, we used DH-36 Naval structural steel characterized by Nemat-Nasser and Guo [40]. In section (2.3.2), a complete description of these material models are presented.

2.2 Problem Description

In this section, the details of the proposed problem are described. This numerical example is designed to address the possibility of improving the impact-resistance of steel plates by using highly dissipative materials such as polyurea.

2.2.1 Circular steel plates subjected to impulsive loadings

When a circular plate is subjected to impulsive loadings, it deforms axi-symmetrically and is typically shaped into a bowl before the failure/fracture occurs. Figure (2.1) illustrates a rough estimation of the steel plate deformation. The experimental observations suggest that three different failure modes can occur [41, 42]: large inelastic deformation and fracture at point A due to excessive tension (Mode I); tearing at the edge (points B and C) due to shearing (Mode II); or tension (Mode III). Failure modes II and III are contingent upon the edge conditions and the methods by which the edges are fixed. Therefore, these failure modes can be altered or eliminated by thickening the edges or designing different edge shapes. We focus our attention on the first failure mode, and compare different cases based upon their resistance to the first failure mode.

2.2.2 Geometry and boundary assumptions

A numerical problem is designed and proposed to serve as a framework for our study on polyurea-steel bi-layer composites. Figure (2.2), which is an axi-symmetric view of a 3D model, illustrates the details of the proposed problem. A 3 cm layer of polyurea is placed on a circular steel plate of diameter $1.4m$. In our simulations, we vary the position of polyurea with respect to the steel plate and its thickness. We refer to the side of the steel plate receiving the pressure pulse as

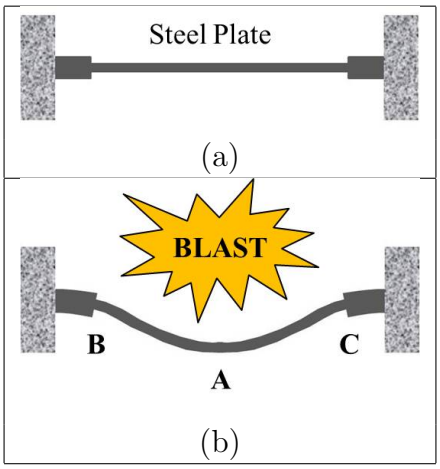

Figure 2.1: Typical deformation of circular steel plates subjected to axi-symmetric blast loads: (a) the circular steel plate cross-section before deformation, (b) the circular steel plate after the blast, shaped into a bowl; failure Mode I occurs at point A due to excessive tension. Failure Modes II and III occur at points B and/or C.

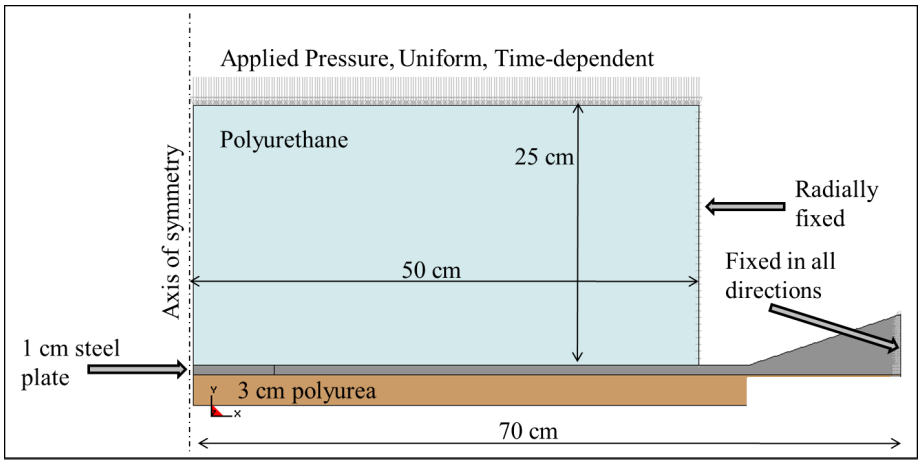

Figure 2.2: Axi-symmetric view of the proposed 3D model. The time-varying impulsive load (uniform here) is applied to the top of the polyurethane that is radially confined. The steel plate is designed to have a wedge-shape edge to avoid undesirable failure modes. In this figure, polyurea is placed on the back face.

the *front face*, and the side which does not face the loading as the *back face*. For example, in figure (2.2), polyurea is placed on the back face. This bi-layer system of polyurea and steel plate is subjected to an impulsive load with a defined shape and time-history. In this study, the time-varying pressure pulse is applied to the system in two ways:

- Indirect: The pressure pulse is applied to a medium with a relatively low impedance (*polyurethane* in figure 2.2). The pressure pulse is transmitted to the bi-layer system through this medium. Such medium ensures capturing the physics behind the impact phenomenon and wave interactions. In section (2.4.3), *water* is used instead of polyurethane and the differences resulting from this substitution are described.

- Direct: The pressure pulse is directly applied to the bi-layer system. The shape of the pressure pulse can be uniform or non-uniform. In this study, a Gaussian distribution for the pressure pulse is assumed, which will be discussed in section (2.4.4).

The polyurethane is radially fixed. As a result, the pressure pulse travels through the polyurethane without loosening its uniformity in shape. The circular steel plate is designed such that it experiences the highest stresses and tension at the central regions, leading to the first mode of failure explained in section (2.2.1). More specifically, the edge of the steel plate is designed to be wedge-shaped. The outer edge of the wedge is fixed both translationally and rotationally. The polyurea layer is extended to the inner edge of the wedge, and no constraint is applied to its edges.

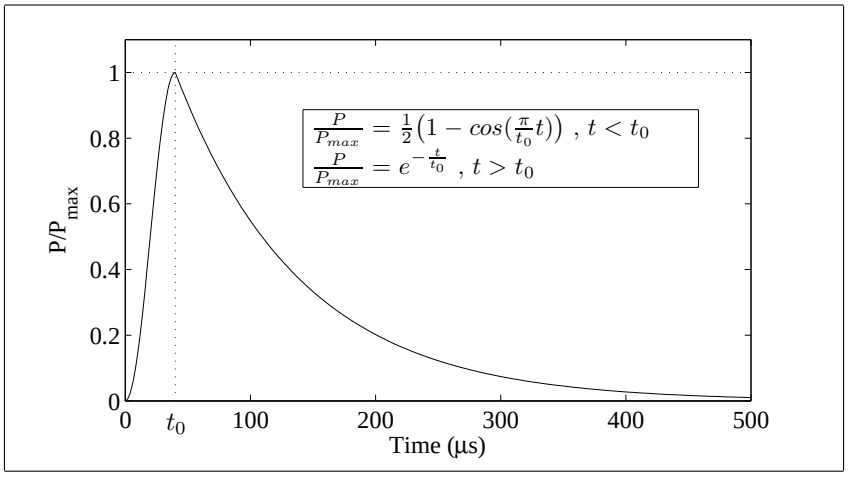

Figure 2.3: The time-history of the pressure pulse applied to the polyurethane. The pressure rises within $40\mu s$ and exponentially declines with a decay constant of $40\mu s$.

2.2.3 Impulsive loading: time-varying pressure pulse

The impulsive pulse applied to the bi-layer system is assumed to vary in time as depicted below:

$$\frac{P}{P_{max}} = p_t(t) = \frac{1}{2}\left(1 - cos(\pi\frac{t}{t_0})\right) \qquad for\ t < t_0 \qquad (2.1)$$

$$\frac{P}{P_{max}} = p_t(t) = e^{-\frac{t}{t_0}} \qquad for\ t > t_0 \qquad (2.2)$$

where, t_0 is the rise-time, and P_{max} is the maximum pressure. Figure (2.3) illustrates the time-history of the applied pressure pulse.

2.3 Numerical Simulations

In the following section, the finite element model, material models and the simulated cases are explained in detail.

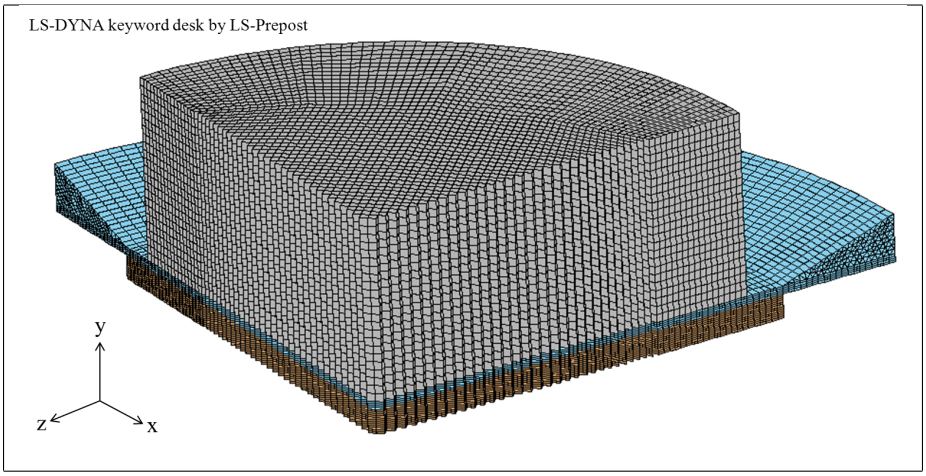

Figure 2.4: The finite element mesh: 8-node brick elements are used in all parts; except for the wedge part for which 6-node wedge elements are used. The mesh is refined so that an element-size independent solution is achieved.

2.3.1 Finite element model

The proposed problem is numerically modeled and analyzed in an explicit finite element framework. LS-DYNA, a commercially available software package well-established in impact engineering, is employed as the FEM solver. Figure (2.4) illustrates the elements from one quarter of the 3D model. All parts have 8-node Lagrangian brick elements; except the wedge, for which 6-node Lagrangian wedge elements are used.

2.3.2 Material models

For the polyurea, an experimentally-based material model is used, which is pressure- and temperature-sensitive and has been developed and tested by Amirkhizi et al. [39]. This model is based upon incremental updates of stress components and assumes linear viscoelasticity at each time increment. It calculates the bulk and shear moduli at each step based upon the state variables (i.e. temperature, pres-

sure and strain rate). In other words, it explicitly computes the following hereditary integral:

$$\boldsymbol{\sigma}(t) = \int_{-\infty}^{t} (3K(t-\tau)\mathbf{E}^1 + 2G(t-\tau)\mathbf{E}^2) : \mathbf{D}(\tau)d\tau \tag{2.3}$$

where, K and G are the bulk and shear moduli, respectively; and $\mathbf{D}$ is the deformation-rate tensor. Fourth-order tensors, $\mathbf{E}^1$ and $\mathbf{E}^2$ are simple known tensors from isotropic elasticity that separate the deviatoric and dilatational parts of the elasticity tensor. For bulk deformations, the model assumes the following:

$$tr(\boldsymbol{\sigma}) = 3\kappa\frac{lnJ}{J} \tag{2.4}$$

$$J = det(\mathbf{F}) = |\frac{\partial x}{\partial X}| \tag{2.5}$$

where, J is the Jacobian of the deformation tensor, and κ is a experimentally obtained bulk modulus that depends linearly on temperature:

$$\kappa(T) = \kappa(T_{ref}) + m(T - T_{ref}) \tag{2.6}$$

where, T_{ref} is the reference temperature. The deviatoric part of equation (2.3) is written as:

$$\boldsymbol{\sigma}^{'}(t) = \int_{0}^{t} G(\tau, T, P)\mathbf{D}^{'}(\tau)d\tau \tag{2.7}$$

where, $\mathbf{D}^{'}$ is the deviatoric part of the deformation-rate tensor, and $G(\tau, T, P)$ is extracted from the time-temperature-pressure master curve for polyurea. A four-term ($n = 4$) Prony series defines the relaxation function:

$$G(\tau, T, P) = \frac{T(\tau)}{T_{ref}} 2G_{ref}\left(\xi(t) - \xi(\tau)\right) \tag{2.8}$$

$$G_{ref}(t) = G_{\infty}\left(1 + \sum_{i=1}^{n} p_i e^{-t/q_i}\right) \tag{2.9}$$

where, p_i and q_i are Prony series coefficients, and ξ is a reduced time and is related to time as:

$$\xi(t) = \int_0^t \frac{d\tau}{a_T(\tau)} \tag{2.10}$$

$$a_T = 10^{\frac{A(T-C_{tp}P-T_{ref})}{B+T-C_{tp}P-T_{ref}}} \tag{2.11}$$

where, P is pressure, C_{tp} is a time-pressure coefficient and A, B and T_{ref} are parameters given by Knauss [43] for polyurea. The temperature, T, at each time step is evaluated assuming that: (a) the dissipated work is entirely transformed into heat, (b) the heat is trapped inside the material, and (c) the heat only accounts for temperature changes:

$$\frac{\partial T}{\partial t} = \frac{1}{C_v}\frac{\partial W_d}{\partial t} \tag{2.12}$$

where, C_v is the heat capacity at constant volume, and W_d is the dissipated work. The dissipated work is evaluated as below:

$$\frac{\partial W_d}{\partial t} = G_\infty \frac{T(t)}{T_{ref}} \sum_{i=1}^{n} \frac{p_i}{q_i} \boldsymbol{\epsilon}_d^i(t) : \boldsymbol{\epsilon}_d^i(t) \tag{2.13}$$

where,

$$\boldsymbol{\epsilon}_d^i(t) = \int_0^t e^{-(\xi(t)-\xi(\tau))/q_i} \mathbf{D}'(\tau) d\tau \tag{2.14}$$

Table (2.1) lists the numerical values used for the parameters in polyurea material model. This polyurea material model shows a reliable match to experimental results [39].

A physics-based material model is available for DH-36 Naval structural steel. Nemat-Nasser and Guo [40] have conducted a series of experiments on this material and reported that the DH-36 steel is strongly temperature and strain rate dependent; with temperature sensitivity greater for temperatures below 400K and very low above that. Based on the dislocation theory, and with an insight

Table 2.1: Numerical values of the parameters in the polyurea material model used for the simulations.

$T_{ref}(K)$	A	B	$C_{tp}(K/GPa)$
273	-10	107.54	7.2
$C_v(J/mm^3/K)$	$m(GPa/K)$	κ_{ref}	G_∞
1.997×10^{-3}	-0.015	4.948	0.0224
p_1	p_2	p_3	p_4
0.8458	1.686	3.594	4.342
q_1	q_2	q_3	q_4
463.4	0.06407	1.163×10^{-4}	7.321×10^{-7}

from experimental data, a physically based model is developed by Nemat-Nasser and Isaacs [44], Nemat-Nasser et. al. [45] and Nemat-Nasser and Guo [46], applied to several polycrystalline metals. This model expresses the flow stress (effective stress), τ, as a function of temperature, T, effective plastic strain, γ, and effective plastic strain rate, $\dot{\gamma}$,

$$\tau = \tau_a^0 \gamma^{n_1} + \tau^0 \left\{ 1 - \left[\frac{-kT}{G_0} \left(\ln \frac{\dot{\gamma}}{\dot{\gamma}_0} + \ln \left(1 + a(T)\gamma^{\frac{1}{2}} \right) \right) \right]^{\frac{1}{p}} \right\}^{\frac{1}{p}} \left(1 + a(T)\gamma^{\frac{1}{2}} \right)$$

$$, for T \leq T_c \tag{2.15}$$

$$\tau = c_0 + c_1^{n_1} \qquad , for T \geq T_c \tag{2.16}$$

$$a(T) = a_0 \left[1 + \left(\frac{T}{T_m} \right)^2 \right] \tag{2.17}$$

where, G_0 is the total energy of the shift-range barrier to the motion of dislocations, and k is the Boltzmann constant. Remaining constants are the material properties that can be derived by comparison to experimental data. These constants are derived by Nemat-Nasser and Guo [40] for DH-36 and are used in our simulations.

The polyurethane is modeled by the Moony-Rivlin rubber material model

[47] which is based on a strain energy function:

$$W = A(I_1 - 3) + B(I_2 - 3) + C(\frac{1}{I_3^2} - 1) + D(I_3 - 1)^2 \tag{2.18}$$

where, A and B are user defined constants; whereas C and D are derived from A and B. $I_1 - I_3$ are derived from invariants of the right Cauchy-Green tensor. The stress update is then given by [48]

$$J\sigma_i = \lambda_i \frac{\partial W}{\partial \lambda_i} \tag{2.19}$$

where, λ_i's represent uniform dilatation. Our inputs to this model are shear modulus $G = 16MPa$, Poisson's ratio $\nu = 0.495$ and the density $\rho = 1.19g/cc$.

2.3.3 Finite element model details

The finite element mesh was generated in Altair Hypermesh. An input file suitable for LS-DYNA was prepared for an explicit finite element analysis. The mesh was refined to achieve element-size independent results.

The pressure time-history curve was defined and LS-DYNA keyword, LOAD_SEGMENT_SET_ID, was used to apply the pressure on top of the polyurethane ($-y$ direction in our model). The model uses the LS-DYNA contact option, CONTACT_AUTOMATIC_SURFACE_TO_SURFACE_TITLE,
to model the interactions between the polyurethane and the bi-layer system.

The outer nodes of the polyurethane column was radially fixed; i.e. $u_x = u_z = 0$. The outer nodes of the steel plate and the wedge were also fixed in all directions. The Flanagan-Belytschko integration hourglass-control algorithm is used to eliminate zero-energy modes.

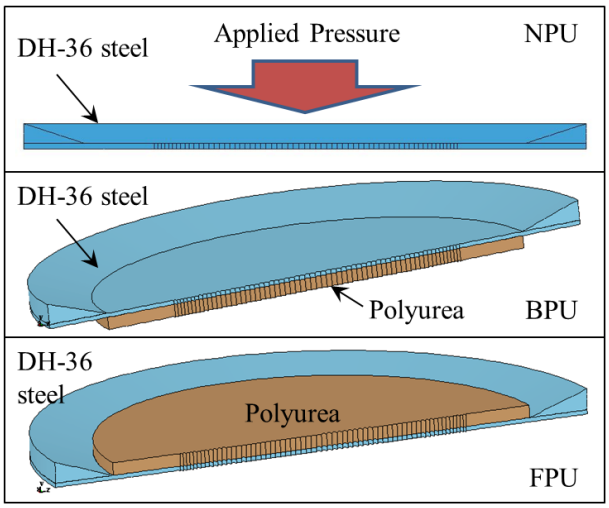

Figure 2.5: Simulated cases based on position of the polyurea with respect to applied pressure: NPU (no polyurea), BPU (polyurea on the back face) and FPU (polyurea on the front face). Different thicknesses of polyurea are considered for each case. Table (2.2) lists all the simulated cases.

2.3.4 Simulated cases with polyurethane and uniform pressure

In this study, the main goal is to determine to what extend placing a layer of polyurea on a steel plate affects its performance when subjected to impulsive loadings. The effect of polyurea thickness on overall response of the bi-layer system to impulsive loadings is also investigated. Therefore, the following cases are simulated (figure 2.5):

- BPU (Polyurea on the back face): Polyurea is placed on the side of the steel plate opposite to the loading. Four cases with different polyurea thicknesses are simulated: 1 cm, 2 cm, 3 cm and 4 cm. The thickness of steel is maintained at 1 cm for all the cases.

- FPU (Polyurea on the front face): Polyurea is placed on the side of the

Table 2.2: The geometry and applied pressure specifications for all the simulated cases. In these cases, polyurethane parts are employed as the pressure transmitting media. A uniform pressure is applied to the top of the polyurethane. Parameters, P_{max}, and, t_0, are defined in section (2.2.3).

Configuration	Steel Thickness	Polyurea Thickness	Pressure Type	P_{max} (MPa)	$t_0(\mu s)$
NPU (NO PU)	1.14 cm	0.0 cm	Uniform, Indirect	200	40
BPU (PU-Back)	1.0 cm	1.0 cm	Uniform, Indirect	200	40
FPU (PU-Front)	1.0 cm	1.0 cm	Uniform, Indirect	200	40
NPU (NO PU)	1.28 cm	0.0 cm	Uniform, Indirect	200	40
BPU (PU-Back)	1.0 cm	2.0 cm	Uniform, Indirect	200	40
FPU (PU-Front)	1.0 cm	2.0 cm	Uniform, Indirect	200	40
NPU (NO PU)	1.42 cm	0.0 cm	Uniform, Indirect	200	40
BPU (PU-Back)	1.0 cm	3.0 cm	Uniform, Indirect	200	40
FPU (PU-Front)	1.0 cm	3.0 cm	Uniform, Indirect	200	40
NPU (NO PU)	1.56 cm	0.0 cm	Uniform, Indirect	200	40
BPU (PU-Back)	1.0 cm	4.0 cm	Uniform, Indirect	200	40
FPU (PU-Front)	1.0 cm	4.0 cm	Uniform, Indirect	200	40

steel plate which receives blast loading. Four cases with different polyurea thicknesses are simulated: 1 cm, 2 cm, 3 cm and 4 cm. The thickness of steel is maintained at 1 cm for all the cases.

- NPU (No polyurea): In this case, no polyurea is placed on the steel plate. The thickness of steel plate, however, is increased such that the same areal density as the corresponding BPU and FPU cases is attained: 1.14 cm, 1.28 cm, 1.42 cm and 1.56 cm.

In table (2.2), the simulation specifications for all the cases are listed. The pressure is uniform in all the cases, and a polyurethane part is used to transmit the load to the bi-layer system.

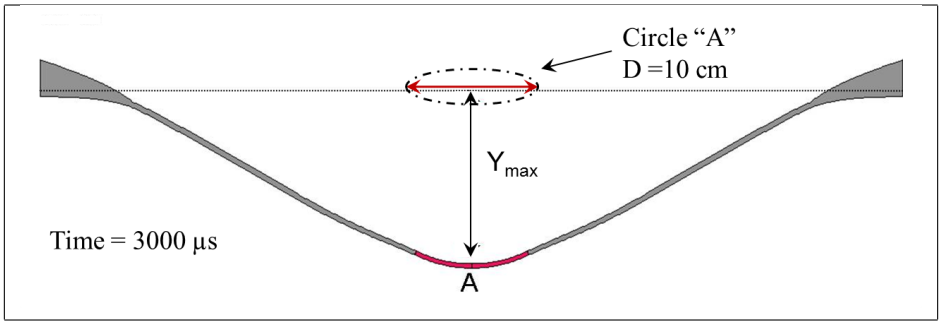

Figure 2.6: The steel plate after deformation. To compare the performance of the steel plates subjected to impulsive loadings, volume average of effective plastic strain in circle A is calculated for each case.

2.4 Results

In this section, the results from the simulations of section (2.3.4) are presented. In section (2.4.1), the metric that we used to compare different cases is introduced and described. In section (2.4.3), the effect of having water instead of polyurethane is explored. In section (2.4.4), results from the direct application of the impulsive load to the steel plate is presented.

2.4.1 Comparison metric

To analyze the performance of steel plates under impulsive loading, we compare the plastic deformation that the steel plates undergo during the deformation process. More specifically, we measure the volume average of effective plastic strain corresponding to a circular region of diameter 10 cm at the center of steel plates. The effective plastic strain is defined as:

$$\gamma(t) = \int_0^t \sqrt{\frac{2}{3}\mathbf{D}^p : \mathbf{D}^p} \; dt \tag{2.20}$$

where, $\mathbf{D}^p$ is the plastic part of the deformation rate tensor. Based on their experimental results, Amini et al. [34, 36] have reported a correlation between this metric and the fracture of DH-36 steel plates and have used this metric as failure/fracture criteria. Figure (2.6) illustrates the cross-sectional view of a deformed steel plate and depicts the area for which effective plastic strain is measured and compared for different cases (circle A). The largest plastic deformations occur inside circle A and, therefore, the fracture/rupture is believed to initiate in this region.

2.4.2 Comparing BPU, FPU and NPU cases

In this section, the time-histories of the volume average of the effective plastic strain at the center of steel plates are plotted and discussed for the cases explained in section (2.3.4). The results are categorized based on the effective polyurea thickness, i.e. for each polyurea thickness (or no polyurea, with the same areal density), the average effective plastic strain is plotted for BPU, FPU and NPU cases.

Figure (2.7) depicts the time-histories of the volume average of the effective plastic strain in circle A for the cases with 1 cm polyurea. It is observed that placing polyurea in this case slightly affects the performance of the steel plate, with negligible difference between the cases.

In figures (2.8), (2.9) and (2.10) the time-histories of the volume average of the effective plastic strain in circle A for the cases with 2 cm, 3 cm and 4 cm polyurea are plotted, respectively. In all cases, 1 cm steel with polyurea performs better than the equivalent steel. Also, polyurea placed on the back face (BPU) demonstrates a better performance than the other two cases (FPU and NPU). The differences become more pronounced as polyurea thickness is increased.

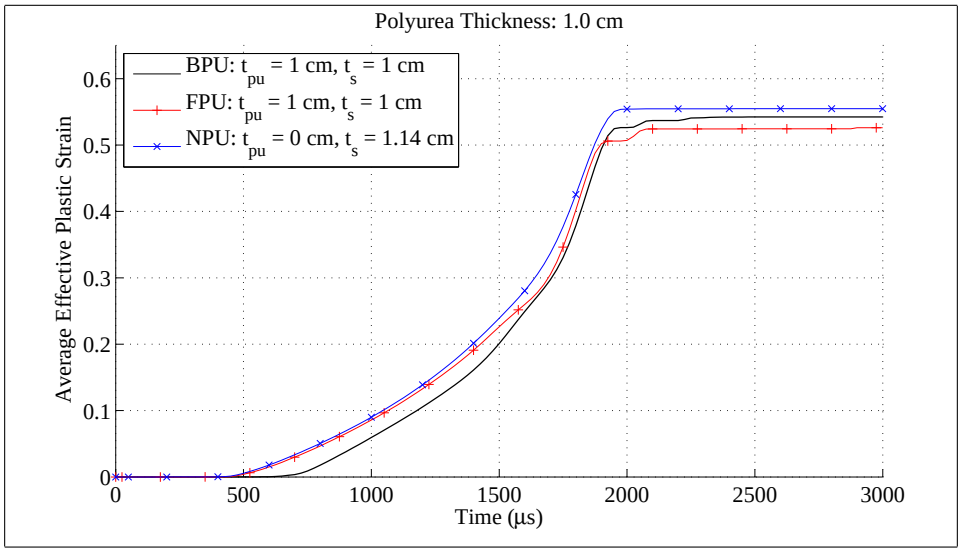

Figure 2.7: The time-history of the average effective plastic strain over a circle of diameter 10 cm at the center of the steel plate, with an effective polyurea thickness of 1 cm. With this polyurea thickness, the performance difference between the cases is nearly negligible.

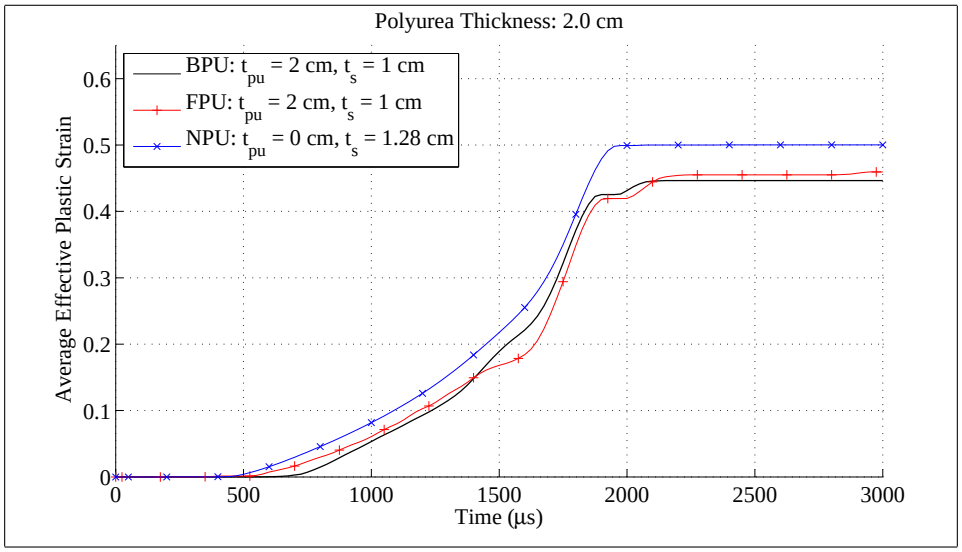

Figure 2.8: The time-history of the average effective plastic strain over a circle of diameter 10 cm at the center of the steel plate, with an effective polyurea thickness of 2 cm. The performance difference between the cases becomes apparent when the thickness of polyurea is equal to, or greater than, 2 cm.

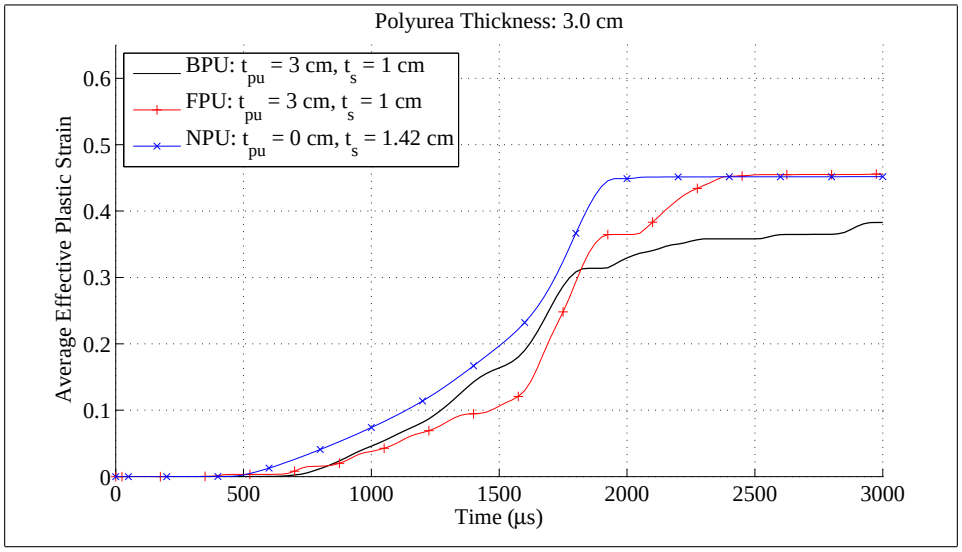

Figure 2.9: The time-history of the average effective plastic strain over a circle of diameter 10 cm at the center of the steel plate for an effective polyurea thickness of 3 cm. The performance difference between the cases becomes more pronounced when the polyurea thickness is increased.

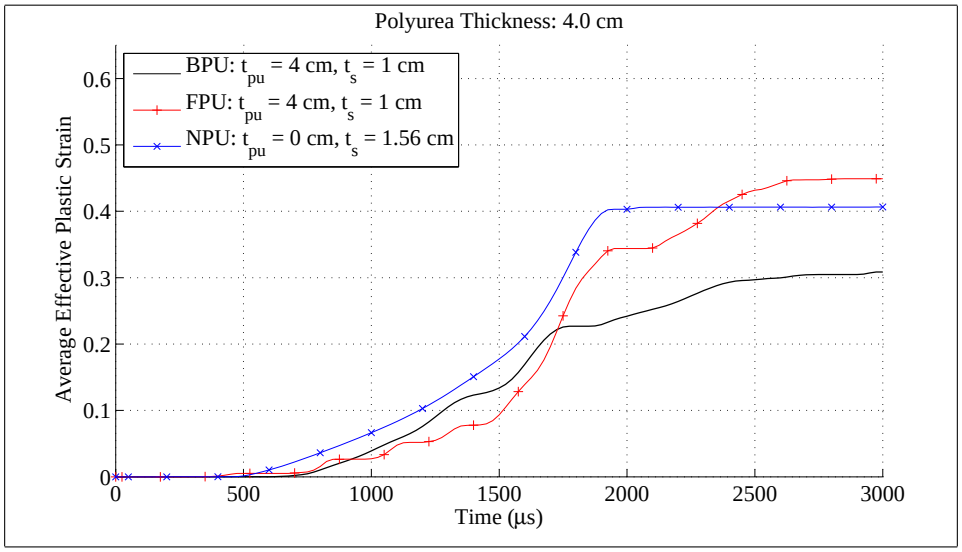

Figure 2.10: The time-history of the average effective plastic strain at a circle of diameter 10 cm at the center of the steel plate for an effective polyurea thickness of 4 cm.

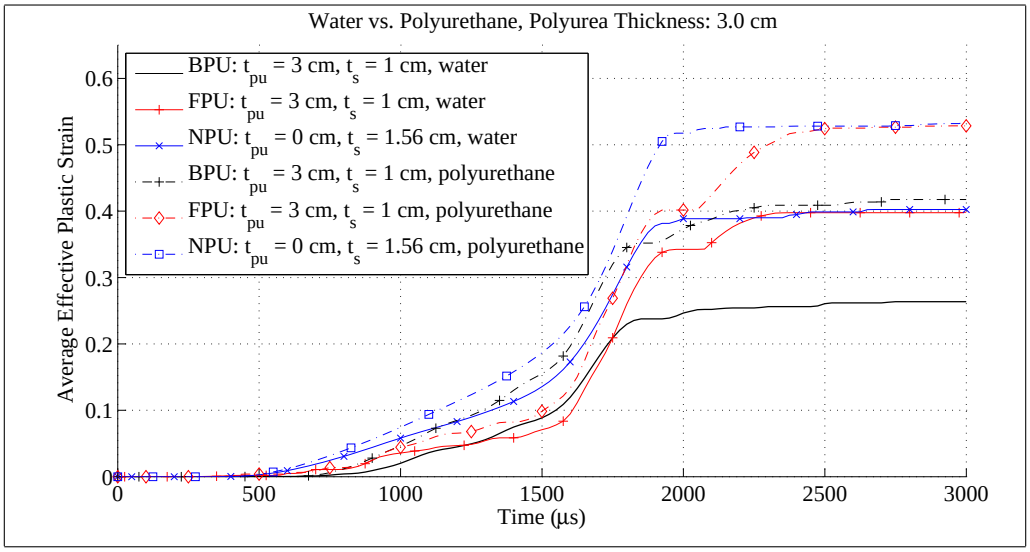

Figure 2.11: Comparing water and polyurethane as momentum transmitting media. The time-history of the average effective plastic strain over a circle of diameter 10 cm at the center of the steel plate for an effective polyurea thickness of 3 cm.

2.4.3 Water vs. polyurethane

In this section, we use water instead of polyurethane in our simulation as the pressure transmitting medium. We compare new results with previous results for cases with 3 cm polyurea. In figure (2.11), the volume average of the effective plastic strain in circle A is plotted for NPU, BPU and FPU cases with 3 cm polyurea. The same overall trend is observed when water is used instead of polyurethane; i.e. BPU performs better than FPU and NPU. However, in the case of water, the transmitted momentum is lower and a smaller plastic deformation occurs at the central regions.

2.4.4 Direct application of the impulsive loading

In this section, we eliminate the momentum transmitting medium (i.e. polyurethane or water) and directly apply the pressure to the bi-layer system.

Table 2.3: The geometrical and pressure specifications for the cases simulating the direct pressure scenarios. In these cases, no pressure transmitting medium is used and a pressure with a Gaussian spatial distribution is directly applied to the bi-layer system. Parameters, P_{max}, and, t_0, are defined in section (2.2.3).

Configuration	Steel Thickness	Polyurea Thickness	Pressure Type	P_{max} (MPa)	$t_0(\mu s)$
NPU (NO PU)	1.00 cm	0.0 cm	Gaussian, Direct	530	40
NPU (NO PU)	1.14 cm	0.0 cm	Gaussian, Direct	530	40
BPU (PU-Back)	1.0 cm	1.0 cm	Gaussian, Direct	530	40
FPU (PU-Front)	1.0 cm	1.0 cm	Gaussian, Direct	530	40
NPU (NO PU)	1.42 cm	0.0 cm	Gaussian, Direct	530	40
BPU (PU-Back)	1.0 cm	3.0 cm	Gaussian, Direct	530	40
FPU (PU-Front)	1.0 cm	3.0 cm	Gaussian, Direct	530	40

A Gaussian distribution with variance of 20 is assumed for the pressure; varying with time in the same manner as the former cases (see section 2.2.3). In other words, the following equation is used for the pressure:

$$\frac{P}{P_{max}} = e^{-\frac{x^2}{2 \cdot 20^2}} \cdot p_t(t) \tag{2.21}$$

where, $p_t(t)$ is the time-varying function given in section (2.2.3). In table (2.3), the geometrical specifications of the simulated cases are presented.

In figures (2.12) and (2.13), the volume average of the effective plastic strain over a circle of 10 cm at the center of the steel plate is plotted. Only the cases with 1 cm and 3 cm polyurea are considered here. The response of the steel plates to this type of loading is clearly different from the cases in section (2.3.4), where a uniform pressure is applied to the bi-layer system through a separate medium. These results suggest that with this type of loading, the effectiveness of polyurea layer is not observable. In other words, the bi-layer system of the BPU configuration has a negligible superiority over the NPU configuration, and the use of polyurea seems redundant. Also, note that in FPU cases, more energy is transmitted to the

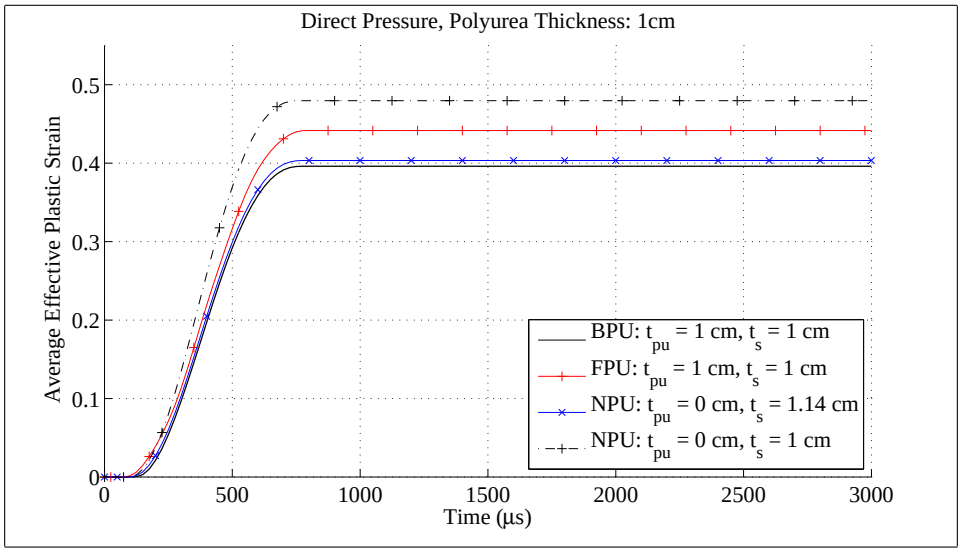

Figure 2.12: The time-history of the average effective plastic strain over a circle of diameter 10 cm at the center of the steel plate for an effective polyurea thickness of 1 cm. There is negligible performance difference between BPU and NPU cases.

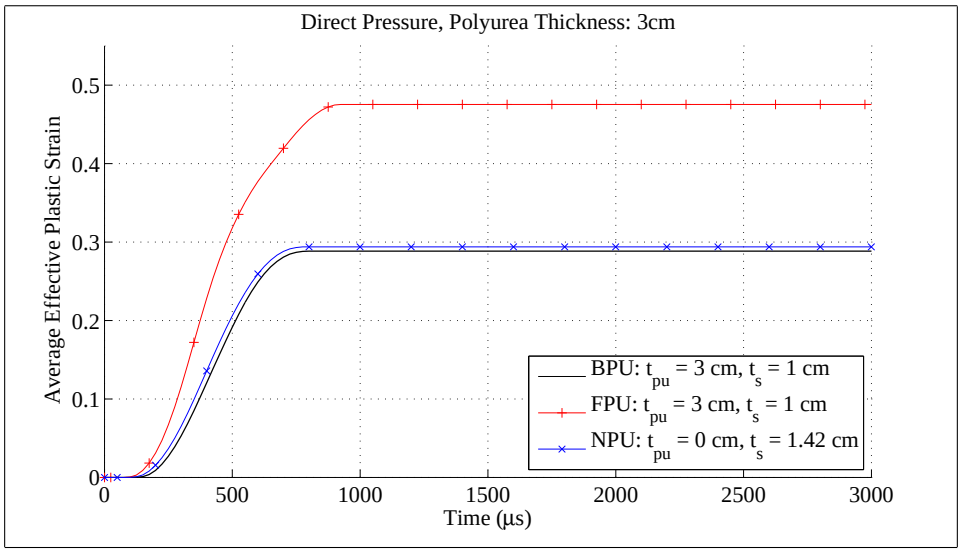

Figure 2.13: The time-history of the average effective plastic strain over a circle of diameter 10 cm at the center of the steel plate for an effective polyurea thickness of 3 cm. Unlike the former cases, there is negligible difference in the performance between BPU and NPU cases when the pressure is directly applied to the bi-layer system.

bi-layer system and higher plastic deformations are observed in the elements at the central parts of the steel plates.

2.5 Summary and Conclusion

In this chapter, the effect of polyurea on the performance of polyurea-steel bi-layers subjected to impulsive loadings was investigated. A numerical problem was designed and simulated using an explicit finite element model in LS-DYNA. The primary objective was to determine the effectiveness of polyurea; and subsequently, determine the manner in which the thickness of polyurea affects the problem. In order to achieve this, different cases were developed and simulated. To ensure obtaining accurate results, reliable material models and mesh-size independent finite element models were employed.

Numerical results suggest that when polyurea is placed on the back face (the side of the steel plate opposite to the impulsive loading), the average plastic strain is less than the cases where the polyurea is placed on the load-receiving side (front face). This result can be explained by considering the unique properties of polyurea. The stiffness of polyurea is highly pressure-dependent and increases by orders of magnitude under locally-confined compression [49]. For FPU cases, when the polyurea layer is confined and compressed by the incoming pressure pulse, its stiffness is considerably increased. As a result, because of a better impedance match with the steel plate, it transmits a greater amount of the impact energy to the steel plate. On the contrary, when polyurea is placed on the back face, it traps and dissipates a large amount of energy due to excessive tension.

It was shown that polyurea thickness is an essential factor in effectiveness of its application. In other words, when a thin layer of polyurea is placed on either

side of the steel plate, the change in performance is negligible. However, when the thickness is increased, the effect of polyurea is more apparent and appreciable.

The effect of loading type on this problem was also investigated. It was shown that there is a remarkable difference between direct and indirect application of pressure to the bi-layer system. When a pressure transmitting medium is used, the problem reflects the physics of the problem more realistically. When the pressure is directly applied to the bi-layer system, however, the wave interactions are undermined and the performance of the bi-layer changes drastically. However, for all cases, the most effective case is found to be BPU; i.e. polyurea placed on the back face.

2.6 Acknowledgments

This numerical work has been conducted at the Center of Excellence in Advanced Materials (CEAM), Mechanical and Aerospace Engineering Department, University of California, San Diego, and has been supported by the ONR grant number N00014-06-1-0340. This chapter is prepared for publication by A. Samiee, A. V. Amirkhizi and S. Nemat-Nasser. The dissertation author is the primary investigator of this work.

Chapter 3

Performance of Steel-Polymer-Steel Sandwich Structures Subjected to Impulsive Loadings

In this chapter, the results from our experiments and numerical modeling of steel-polymer-steel sandwich structures subjected to high-rate loadings are discussed. To study the dynamic response, failure and fracture of such structures under impulsive loadings, a set of impact experiments are performed on circular steel-polyurea-steel sandwich specimens using a 3" Hopkinson bar setup. The experimental results from these experiments are limited to final sample shape and the time-history of force transmitted through the sample. Hence, the entire experiment is numerically modeled in a finite element software package (LS-DYNA) to study the impact process in depth. Numerical results are found to be in good agreement with experimental data indicating the accuracy and validity of the material models

used for polyurea and steel under these loading conditions.

In addition to the aforementioned effort, an independent numerical study is performed on steel-polyurea-steel sandwich structures with larger dimensions. This study is solely numerical due to limitations on experimental capabilities when the sandwich structures are scaled up. The goal is to investigate whether the same trend could be observed when the scale of the problem is different. Accordingly, an axi-symmetric finite element model is designed and developed allowing for fine meshes at a reasonable computational cost.

From experimental and numerical results, it is observed that when a steel-polyurea-steel sandwich structure is exposed to impulsive loading, the steel plate facing the load is more likely to remain intact while the steel plate on the opposite side experiences fracture. In other words, the plate on the back side with respect to the impact, serves as a sacrificial layer, saving the steel plate on the load-receiving side.

3.1 Introduction

To investigate the performance of steel-polymer-steel sandwich structures subjected to impulsive loadings, an experimental and numerical study has been conducted on circular steel plates with a layer of polyurea cast between each pair. Polyurea is a well-known reaction and abrasion resistant polymer and has been extensively used in the coating industry in solid form (e.g. tunnels, bridges, roofs, truck beds). In addition to its coating applications, polyurea has shown exceptional mechanical, physical and chemical properties and has found its applications in the armor and automotive industries. For example, polyurea increases the resistance of military armor to ballistic loads [50]. Amini et al. [51] have shown that a steel

plate with a layer of polyurea coated on the back (with respect to impact loads) delays the necking and rupture of the steel plate, unlike front coated plates where the shock is magnified and failure is promoted.

Polyurea is the product of reaction between an isocyanate component and a synthetic resin blend component. Mechanical properties of polyurea are highly dependent on temperature, pressure and the rate of deformation. The glass transition temperature, T_g, of polyurea is around -50℃[52]. Roland et al. [53] have reported stress-strain measurements for an elastomer polyurea in uni-axial tension over a range of strain rates from 0.06 to 573 s^{-1}. Sarva et al. [54] have reported on the uni-axial compression stress-strain behavior of a representative polyurea over a wide range of strain rates, from 0.001 s^{-1} to 10,000 s^{-1}. They have compared their data to other researchers' results and observed that polyurea undergoes a transition from a rubbery-regime behavior at low rates to a leathery-regime behavior at higher rates. Above the glass transition temperature, polyurea has a nearly elastic volumetric response and a viscoelastic shear response at moderate pressures and strain rates. At room temperature, polyurea is highly elastic and can undergo up to 800% elongation prior to rupture.

While the response of monolithic plates has been studied extensively over the last few decades [55, 56], the applicability and effectiveness of the polymer-steel sandwich structures has become a topic of interest recently. Bahei-El-Din and others [57] have conducted a numerical study on a sandwich structure design and observed that adding an inter-layer of polyurea improves the performance of the structure under blast loads. Xue and Hutchinson [58] have explored the ability of the bi-layer plates to sustain intense impulses and compare the results to the estimated performance of monolithic steel plates of the same total mass.

In this study, polyurea is made by mixing Isonate 2143L [59] and Versalink

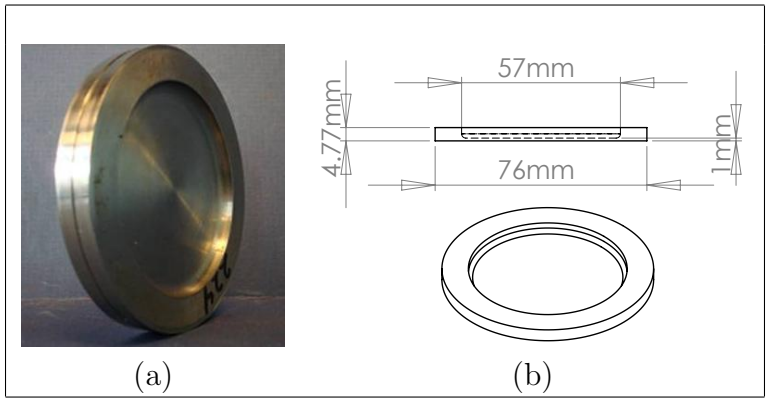

Figure 3.1: (a) A steel-polyurea-steel sample (b) The geometry and dimensions of the steel plates

P1000 [60] under proper conditions with a five percent excess of Isonate 2143L to produce a lightly cross-linked polymer [61]. Amirkhizi et al. [62] have systematically studied the viscoelastic properties of polyurea over a wide range of strain rates and temperatures. Based on this study, a pressure, temperature, and strain-rate sensitive material model has been developed to be utilized in explicit finite element solvers such as LS-DYNA. Using this model for polyurea, the entire process is numerically modeled in LS-DYNA, and the calculations are compared to the experimental results.

3.2 Materials and Experimental Setup

The steel plates used to fabricate the sandwich samples were machined from DH-36 naval structural steel. Polyurea prepared in the material processing lab at UCSD/CEAM was cast between pairs of steel plates. Fabricated samples were stored in an environmental chamber for at least two weeks prior to testing to assure that the polyurea was fully cured. Figure (3.1a) illustrates a typical

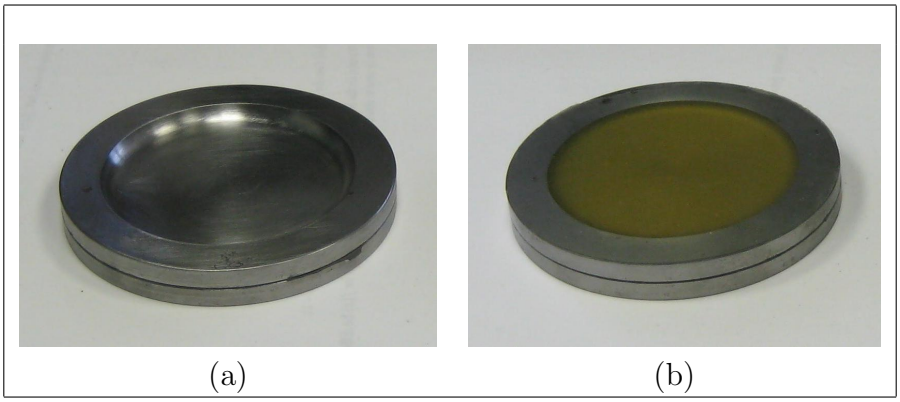

Figure 3.2: Two sandwich sample configurations: (a) SP-PU-SP (steel - polyurea - steel) (b) SP-PU-SP-PU (steel - polyurea - steel - polyurea)

sandwich sample and figure (3.1b) contains the geometry and dimensions of steel plates used to fabricate the samples. Each steel plate has a relatively thick rim on the outer edge that reinforces the structure against large pure rotations. The rim is designed to ensure that the failure occurs at the center of the steel plate. The rim plays an important role in the experiments and changing the design can alter the failure mode, which is discussed in following sections.

For these experiments, samples with three different configurations were fabricated and tested:

1. Regular sandwich sample of figure (3.2a) which has one layer of polyurea and is referred to as SP-PU-SP

2. The second configuration illustrated in figure (3.2b) has an extra layer of polyurea and is refereed to as SP-PU-SP-PU

3. And the third configuration consists of two steel plates with no polyurea layer and is referred to as SP-SP.

A Split Hopkinson Pressure Bar (SHPB) setup was used for conducting the experiments. Figure (3.3) illustrates the Hopkinson bar facility at UCSD, which

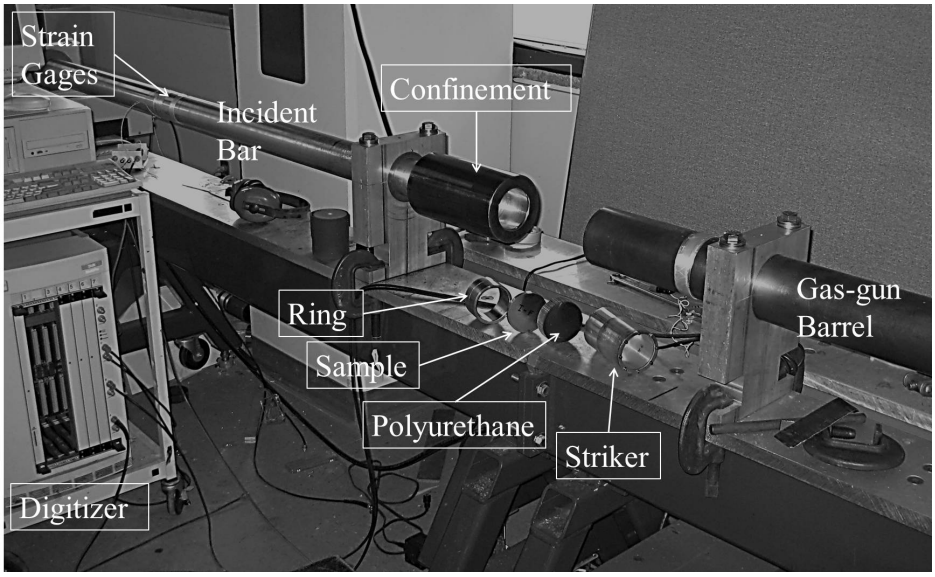

Figure 3.3: The experimental setup: 3-inch Split Hopkinson Pressure Bar (SHPB) and the sample confining components. Only the incident bar is shown in this figure.

consists of a gas gun, barrel, incident bar, transmission (output) bar and brakes. Incident and output bars are each 8-feet long with 3-inch diameters and are made of a high strength aluminum alloy. Two strain gages are precisely surface mounted in the middle of each bar, on opposite sides. These gages are elements of a Whetstone bridge, designed at CEAM, which minimizes possible errors due to bending in the bars. The output signal from the bridge, proportional to the strain at the location of strain gages, is recorded by a digitizer at the sampling rate of 1 MHz.

In these experiments[1], the sample is placed between the incident bar and the end of the barrel. Figure (3.4) illustrates the exploded schematic view of the experimental setup. The sandwich structure is placed between a piece of polyurethane and a hollow steel ring, all fitted in a thick-walled cylindrical confinement. The confinement is slid over the incident bar to the point where the hollow ring is in contact with the incident bar.

[1]The experimental procedure is explained in detail in appendix A.

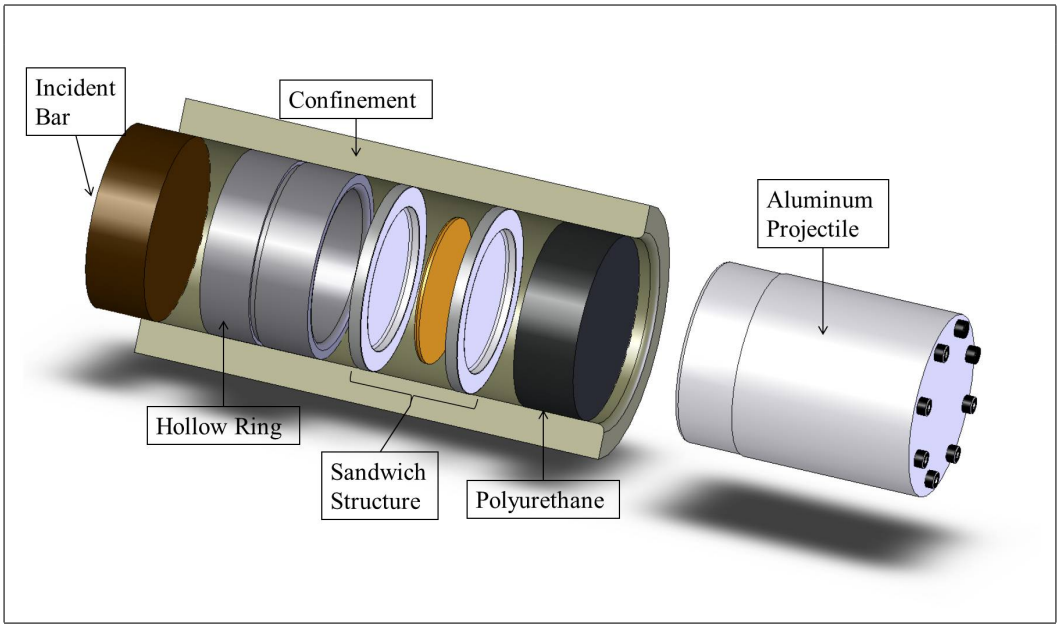

Figure 3.4: The sample-confining components and the projectile. This figure illustrates how the components are positioned with respect to one another in the confinement. Note that only a small part of the incident bar is plotted.

The gas gun is pressurized by a compressed nitrogen tank. When the gun is triggered, high pressure gas accelerates an aluminum projectile through the barrel towards the target. The projectile impacts the target with a high velocity. Two magnetic sensors placed 3 inches apart at the end of the barrel are used to measure the impact velocity. Polyurethane, which is nearly incompressible, is now confined between the projectile and the sample. This subjects the sample to an impulsive pressure pulse.

The stress history transmitted from the sample and hollow ring is measured by the two strain gages mounted on the incident bar. This is the only quantitative measurement from the experiments that can be compared to numerical results for verifying accuracy. This measurement is also a qualitative indication of the average impact load experienced by the sample. The incident bar is stopped by a clamp

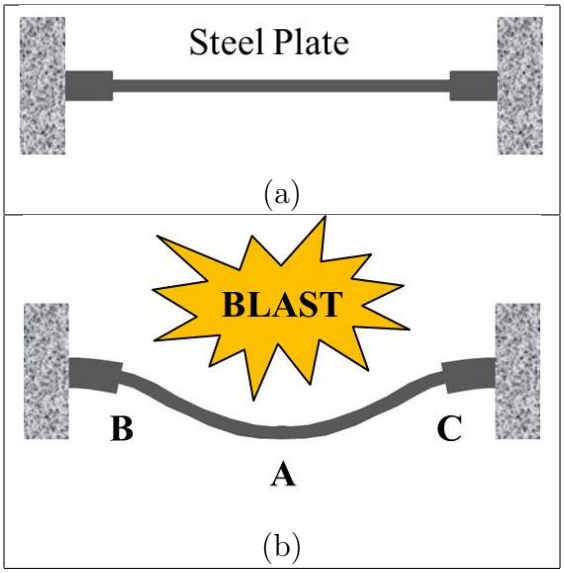

Figure 3.5: Schematic view of a typical thin steel plate blast experiment: The steel plate is shown (a) before the impact and (b) after the impact. Different modes of failure are observed at points A, B and C.

brake in a controlled and repetitive manner.

3.3 Experimental Results

Previous experimental studies on thin steel plates have revealed that three different failure modes can occur [63, 64]. Figure (3.5) illustrates the schematic view of a typical blast experiment for a monolithic circular steel plate. When the steel plate is exposed to impulsive loadings, it may experience a large inelastic deformation and fracture at point A due to excessive tension (Mode I). Also, tearing might happen at the edge (points B and C) due to shearing (Mode II) or tension (Mode III). Different modes of failure can be achieved by altering the edge design. In our experiments, we have designed the rim in order to avoid the second and third failure modes and have focused our attention on the first mode of failure.

Table (3.1) summarizes the experimental results. Four different configu-

rations have been tested with a variety of input energy levels. The impact and rebound velocities of the projectile are measured and used to calculate the input kinetic energy. Experimental results suggest a superior performance for sandwich structures with polyurea (SP-PU-SP and SP-PU-SP-PU) compared with the ones without polyurea (SP-SP). In other words, in a few experiments with the same input energy level, sandwich structures with no polyurea fractured severely, whereas the samples with polyurea did not experience mode I fracture. When the input energy level was increased, the steel plate facing the impact (front plate) did not experience mode I failure, whereas the steel plate on the opposite side (back plate) severely fractured.

Table 3.1: Experimental Results. SP: steel plate, PU: polyurea, KE: Kinetic Energy.

EXP. NO.	Configuration	Projectile Mass (g)	Projectile V (m/s)	Projectile Rebound V (m/s)	Gas Gun Pressure (psi)	Input Kinetic Energy (J)	Final State
D01	SP	832	60.71	-	78	1533.3	Severe Fracture
S01	SP-SP	832	69.4	8.7	100	2003.6	Moderate Fracture
P01	SP-PU-SP	832	69.8	16.2	100	2026.8	No Fracture
B01	SP-PU-SP-PU	832	69.8	14.3	100	2026.8	No Fracture
S02	SP-SP	832	75.1	7.3	122	2346.2	Severe Fracture
P02	SP-PU-SP	832	77.5	13	122	2498.6	No Fracture
B02	SP-PU-SP-PU	832	76.5	14.14	122	2434.5	No Fracture
P03	SP-PU-SP	832	82.1	13.6	150	2804.0	No Fracture / Moderate Shear
B03	SP-PU-SP-PU	832	83.4	13.7	150	2893.5	No Fracture / Moderate Shear
P04	SP-PU-SP	1655	65	-	-	3496.2	Severe Fracture

When the input energy reaches about 2800J, the sample experiences a moderate tearing at the edge (modes II and III). In figure (3.6), two samples that fractured at the inside rim edge are displayed. Therefore, mode I can not be obtained with this sample design without the presence of other failure modes. Increasing

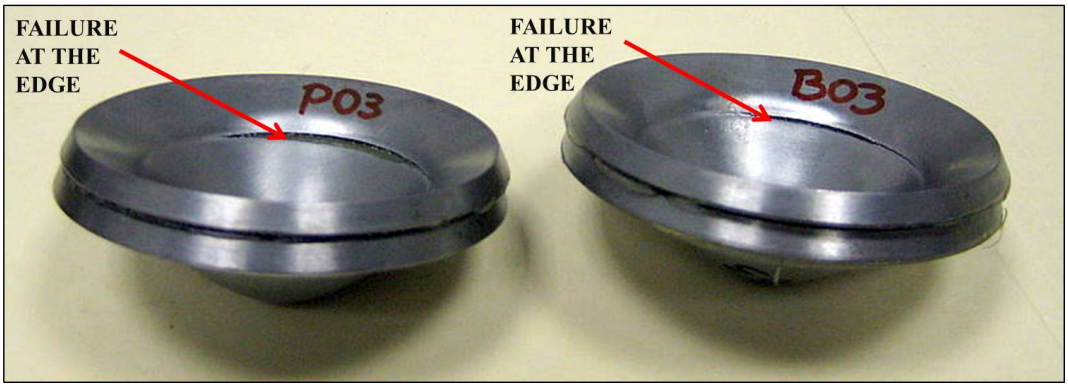

Figure 3.6: The edge effect - some samples undesirably experienced tearing at the edge of the rim; which means that for this rim design failure mode I can not occur without the presence of other failure modes.

the projectile velocity leads to severe fracture of the back plate and no fracture on the front plate.

In figure (3.7), two samples after impact are shown: one with polyurea between the plates (experiment P04) and one without polyurea (experiment S02). In all of the samples severe failure occurs. However, different failure trends are observed in different steel plates. In the sample without polyurea (figure 3.7-left), both of the plates experience failure mode I. In the sandwich sample with polyurea, the front face exposed to the impact tears at the edge (mode II), whereas the steel plate on the back experiences a severe mode I failure. It is remarkable that when polyurea is cast between the steel plates, the front face is protected and does not fracture, while more drastic deformation and fracture occur on the back face. We conclude that the back plate serves as a sacrificial layer, absorbing a great amount of energy when fracture occurs. As a result, the front plate facing the impact remains intact.

The only quantity measured in these experiments is the strain history on the incident bar. This measurement is a qualitative indication of the average pressure

Figure 3.7: Samples after severe fracture: Experiment S02 (left): two plates without polyurea in between, Experiment P04 (middle): Sandwich structure front side, which received the impulsive load and did not fracture at the center, Experiment P04 (right): sandwich structure back side, severely fractured.

applied to the sample. In other words, the pressure applied to the sample creates strain waves that travel through the ring and incident bar before they are measured by the strain gages. When the waves travel through the bar, the following issues should be considered:

- The pulse shape measured at the strain gages is not identical to the pulse transferred through the sample due to dispersion. Waves with different frequencies travel at different velocities and, after some distance, their phases shift relative to one another. As a result, the shape of the pulse measured at the strain gages is not exactly an indication of the time history of the force applied to the ring from the rim of the sample.

- The pressure pulse which is transmitted through the ring becomes more uniform in the cross-section as it travels along the bar. Therefore, the magnitude of this pressure is not equal to that applied to the ring.

Considering these points, the quantity measured at the strain gages is just a rough estimation of the pressure applied to the ring from the sample rim. However, this experimentally acquired quantity can be compared to the results from

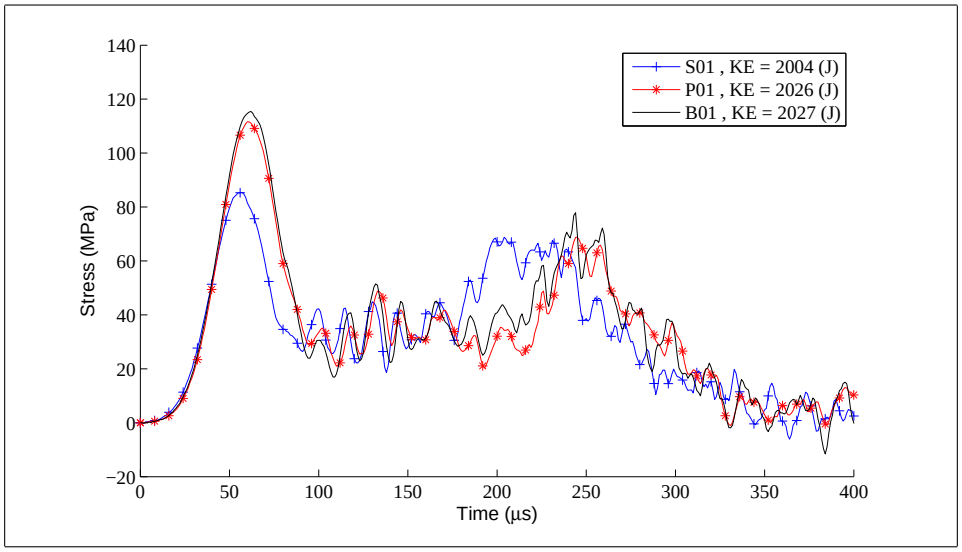

Figure 3.8: Transmitted force for 01 experiments. The input energy in all these cases is about the same (2000J). Note that the smallest peak belongs to the sample without polyurea (experiment S01), which also experiences moderate fracture. The extra layer of polyurea on the back does not seem to affect the deformation process by much (compare experiments P01 and B01).

the numerical simulations to measure the accuracy and verify the validity of the simulations.

Figures (3.8) and (3.9) show the measured stress on the incident bar for experiment sets 01 and 02. The input kinetic energies for experiments 01 and 02 are approximately 2000J and 2400J, respectively. However, in both cases the peak for the sample without polyurea that experiences fracture is noticeably smaller. The time-history of the transmitted force for P cases and B cases closely match. Therefore, the extra layer of polyurea on the back seems to not have much effect on the deformation process for these experiments.

Figure (3.10) compares the transmitted force for the SP-PU-SP sample configuration at different input energy levels. An increase in the peak force is observed from case P01 to case P02. However, from case P02 to P03, although

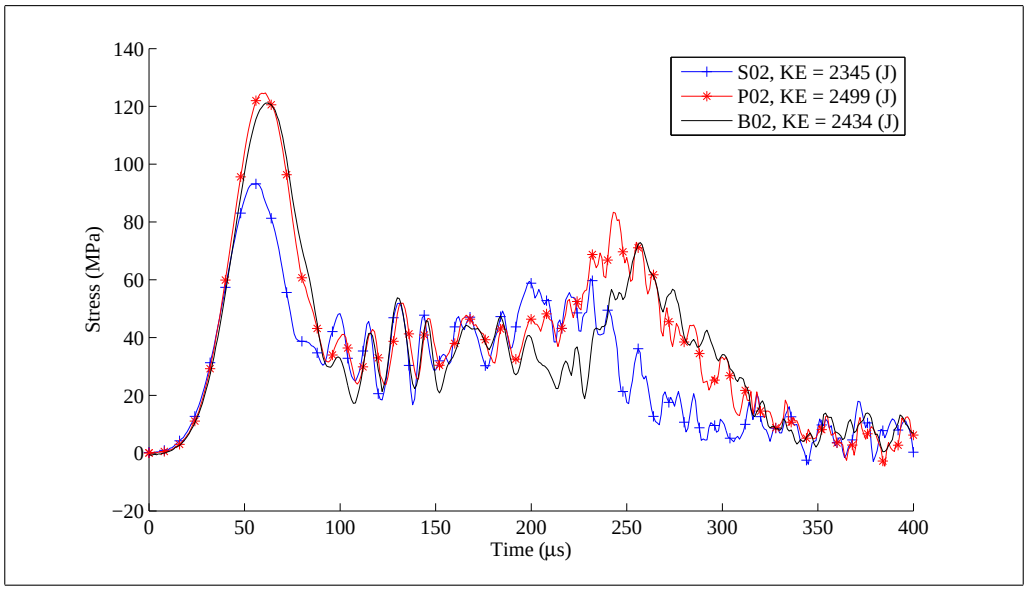

Figure 3.9: Transmitted force for 02 experiments. The input energy in all these cases is about the same (2400J). Note that the smaller peak belongs to the sample without polyurea (experiment S02), which also experiences severe fracture. The extra layer of polyurea on the back seems to not affect the deformation process by much (compare experiments P02 and B02).

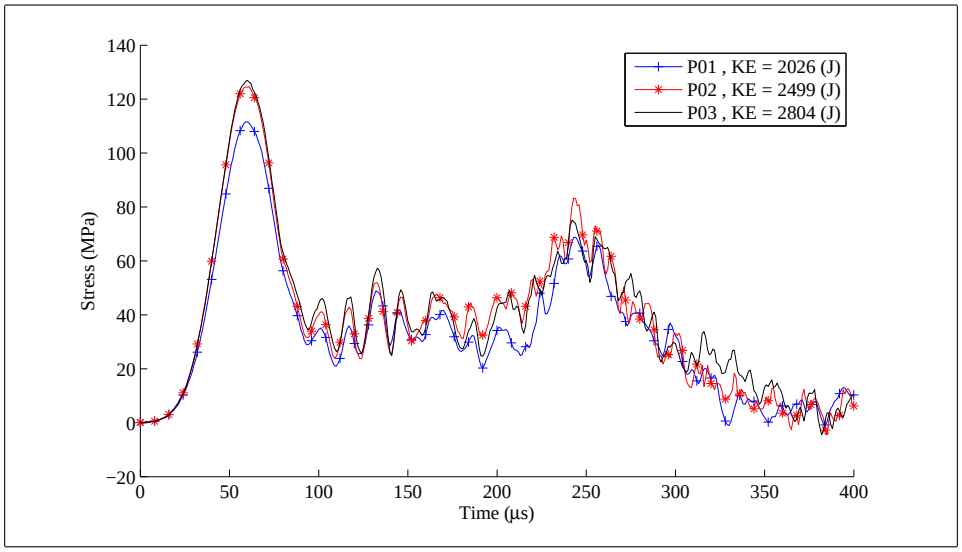

Figure 3.10: Transmitted force for SP-PU-SP samples for different input energy levels. Peak force is increased from the case P01 to the case P02. The same trend, however, is not observed when comparing cases P02 and P03. This can be due to occurrence of a moderate fracture in the case P03, which is a energy dissipative process.

the input energy increases by 15%, the peak transmitted force does not increase comparably. This could be due to the occurrence of a moderate fracture in the case P03, which is an energy dissipative process.

3.4 Finite Element Modeling

A better understanding of sandwich-structure impact experiments can be achieved using computational techniques. Our experimental measurements and observations are mostly qualitative and primarily based on the final shape of the samples. Consequently, a quantitative estimate of the entire process is highly desired. Therefore, a 3D finite element model has been developed that models the entire experimental process. An explicit finite element solver (LS-DYNA) has been employed for numerical calculations. A number of factors are involved in obtaining

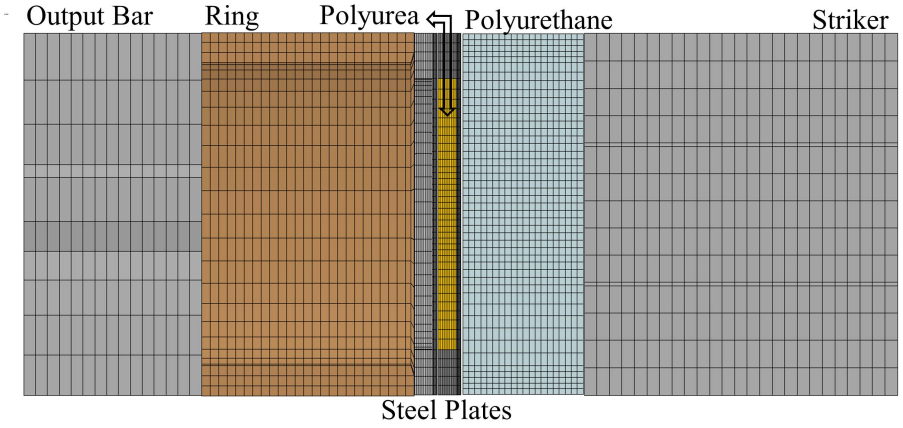

Figure 3.11: Finite element mesh - only a small part of the incident bar is shown

accurate and reliable results from the Finite Element Method (FEM):

- The mesh size should be fine enough to capture the variation of field variables in the model. It is important to reduce the mesh size until a mesh-size independent solution is achieved. However, since an explicit integration is involved, the time step is determined by the size of the smallest element in the model to guarantee stability. Therefore, unnecessary refinement of the mesh size leads to not only a larger numerical problem but also smaller time steps and subsequently, a more computationally expensive problem.

- The boundary conditions and contact surfaces should be realistic and local loadings (for example on one node) should be avoided.

- The most important factor is the use of reliable material models. The material models should cover the physics of the problem.

In this section the details of the finite element model are explained and discussed.

3.4.1 Elements and boundary conditions

Figure (3.11) contains the main part of the finite element mesh. 8-node solid elements with the Lagrangian formulation are used for all parts except polyurethane for which the Arbitrary Lagrangian Eulerian (ALE) formulation is used. Polyurethane experiences very high and unusual deformation and the Lagrangian formulation can not capture the process due to the occurrence of a negative Jacobian(self-interference) in some elements. When the Lagrangian formulation is used, before the model crashes due to a negative Jacobian, the stresses and strains are generally lower compared to the case where the ALE formulation is used.

The loading process is through the polyurethane and no external loads (surface tractions) are directly applied to the sample nodes. The only initial condition is the projectile's velocity which is applied directly to the projectile nodes. Polyurethane which is placed between the projectile and the sample is radially constrained. A non-reflecting boundary condition is applied after the strain gages on the bar, and the rest of the incident bar is not included in the model. In the experiments we are not interested in measuring the waves reflected from the end of the incident bar and we don't need to take them into account in our simulations.

3.4.2 Finite element solver

LS-DYNA, a finite element software package well-known in impact and blast applications, was employed to carry out the calculations. One of the main advantages of this software is its user-defined material model capability. For our simulations, material models for DH-36 steel and polyurea were compiled into the executive file. In section (3.4.3), each material model is explained in detail. Some of the essential LS-DYNA *keywords* used in this model are as follows:

- *CONSTRAINED_LAGRANGE_IN_SOLID; This keyword is used to distinguish the ALE elements from the Lagrangian elements. The interaction between ALE and Lagrangian elements is computed and handled when this keyword is used.

- *CONTACT_AUTOMATIC_SURFACE_TO_SURFACE_TITLE; This keyword is used to define the contact surfaces between different parts.

- *CONTACT_TIED_SURFACE_TO_SURFACE_TITLE; This keyword is used to define the contact surface between the polyurea and steel plates.

- *BOUNDARY_NON_REFLECTING; This keyword is used at the location of strain gages on the incident bar. LS-DYNA assumes that the geometry is extended to infinity wherever this keyword is used.

- *INITIAL_VELOCITY; This keyword is used to apply the initial velocity to the projectile's nodes.

All the calculations were carried out on a workstation with an Intel Pentium D 3.4GHz CPU and RedHat Enterprise 5.0 operating system. Total calculation time was about 12 hours.

3.4.3 Material models

In this section[2], the material models used in our finite element simulations are introduced. For polyurea, an experimentally-based material model is used which is pressure- and temperature-sensitive and has been developed and tested by

[2]This section is the duplicate of section (2.3.2) and is repeated here for the sake of chapter independence and readability.

Amirkhizi et al. [62]. This model is based upon incremental updates of stress components and assumes linear viscoelasticity at each time step. It evaluates bulk and shear moduli at each step based upon state variables (i.e. temperature, pressure and strain rate). In other words, it explicitly evaluates the following hereditary integral:

$$\boldsymbol{\sigma}(t) = \int_{-\infty}^{t} (3K(t-\tau)\mathbf{E}^1 + 2G(t-\tau)\mathbf{E}^2) : \mathbf{D}(\tau)d\tau \tag{3.1}$$

where, K and G are bulk and shear moduli, respectively; and $\mathbf{D}$ is the deformation-rate tensor. Fourth-order tensors, $\mathbf{E}^1$ and $\mathbf{E}^2$ are simple known tensors from isotropic elasticity which separate the deviatoric and dilatational parts of the elasticity tensor. For bulk deformation, the model assumes

$$tr(\boldsymbol{\sigma}) = 3\kappa\frac{lnJ}{J} \tag{3.2}$$

$$J = det(\mathbf{F}) = |\frac{\partial x}{\partial X}| \tag{3.3}$$

where, J is the Jacobian of the deformation tensor, and κ is a experimentally evaluated modified bulk modulus that depends linearly on temperature:

$$\kappa(T) = \kappa(T_{ref}) + m(T - T_{ref}) \tag{3.4}$$

where, T_{ref} is the reference temperature. The deviatoric part of equation (3.1) is written as:

$$\boldsymbol{\sigma}^{'}(t) = \int_{0}^{t} G(\tau, T, P)\mathbf{D}^{'}(\tau)d\tau \tag{3.5}$$

where, $\mathbf{D}^{'}$ is the deviatoric part of the deformation-rate tensor, and $G(\tau, T, P)$ is extracted from the time-temperature-pressure master curve for polyurea. A four-

term ($n = 4$) Prony series defines the relaxation function:

$$G(\tau, T, P) = \frac{T(\tau)}{T_{ref}} 2G_{ref} \left(\xi(t) - \xi(\tau)\right) \tag{3.6}$$

$$G_{ref}(t) = G_\infty \left(1 + \sum_{i=1}^{n} p_i e^{-t/q_i}\right) \tag{3.7}$$

where, p_i and q_i are Prony series coefficients, and ξ is a reduced time and is related to time as shown:

$$\xi(t) = \int_0^t \frac{d\tau}{a_T(\tau)} \tag{3.8}$$

$$a_T = 10^{\frac{A(T - C_{tp}P - T_{ref})}{B + T - C_{tp}P - T_{ref}}} \tag{3.9}$$

where, P is pressure, C_{tp} is a time-pressure coefficient and A, B and T_{ref} are parameters which are given by Knauss [52] for polyurea. The temperature, T, at each time step is evaluated assuming that the dissipated work is entirely transformed into heat which is trapped in the material and only accounts for temperature changes:

$$\frac{\partial T}{\partial t} = \frac{1}{C_v} \frac{\partial W_d}{\partial t} \tag{3.10}$$

where, C_v is the heat capacity at constant volume, and W_d is the dissipated work. The dissipated work is evaluated as below:

$$\frac{\partial W_d}{\partial t} = G_\infty \frac{T(t)}{T_{ref}} \sum_{i=1}^{n} \frac{p_i}{q_i} \boldsymbol{\epsilon}_d^i(t) : \boldsymbol{\epsilon}_d^i(t) \tag{3.11}$$

where,

$$\boldsymbol{\epsilon}_d^i(t) = \int_0^t e^{-(\xi(t) - \xi(\tau))/q_i} \mathbf{D}'(\tau) d\tau \tag{3.12}$$

Table (3.2) lists the numerical values used for the parameters in polyurea material model. This polyurea material model shows a reliable match to experimental results [62].

Table 3.2: Numerical values of parameters in polyurea material model used for our simulations.

$T_{ref}(K)$	A	B	$C_{tp}(K/GPa)$
273	-10	107.54	7.2
$C_v(J/mm^3/K)$	$m(GPa/K)$	κ_{ref}	G_∞
1.997×10^{-3}	-0.015	4.948	0.0224
p_1	p_2	p_3	p_4
0.8458	1.686	3.594	4.342
q_1	q_2	q_3	q_4
463.4	0.06407	1.163×10^{-4}	7.321×10^{-7}

A physics-based material model is available for DH-36 Naval structural steel. Nemat-Nasser and Guo [40] have conducted a series of experiments on this material and reported that the DH-36 steel is strongly temperature and strain rate dependent; with temperature sensitivity greater for temperatures below 400K and very low above that. Based on the dislocation theory, and with an insight from experimental data, a physically based model is developed by Nemat-Nasser and Isaacs [44], Nemat-Nasser et. al. [45] and Nemat-Nasser and Guo [46], applied to several polycrystalline metals. This model expresses the flow stress (effective stress), τ, as a function of temperature, T, effective plastic strain, γ, and effective plastic strain rate, $\dot{\gamma}$,

$$\tau = \tau_a^0 \gamma^{n_1} + \tau^0 \left\{ 1 - \left[\frac{-kT}{G_0} \left(\ln \frac{\dot{\gamma}}{\dot{\gamma}_0} + \ln \left(1 + a(T) \gamma^{\frac{1}{2}} \right) \right) \right]^{\frac{1}{p}} \right\}^{\frac{1}{p}} \left(1 + a(T) \gamma^{\frac{1}{2}} \right)$$

$$, for T \leq T_c \tag{3.13}$$

$$\tau = c_0 + c_1^{n_1} \qquad , for T \geq T_c \tag{3.14}$$

$$a(T) = a_0 \left[1 + \left(\frac{T}{T_m} \right)^2 \right] \tag{3.15}$$

where, G_0 is total energy of the shift-range barrier to the motion of dislocations, k is the Boltzmann constant. Remaining constants are material properties which can be derived by comparison to experimental data. These constants are derived by Nemat-Nasser and Guo [65] for DH-36 and are used in our simulations.

Polyurethane is modeled by LS-Dyna incompressible Moony-Rivlin rubber material model [66] which is based on a strain energy function:

$$W = A(I_1 - 3) + B(I_2 - 3) + C(\frac{1}{I_3^2} - 1) + D(I_3 - 1)^2 \tag{3.16}$$

where, A and B are user defined constants; whereas C and D are derived from A and B. $I_1 - I_3$ are derived from invariants of the right Cauchy-Green tensor. The stress update is then given by [67]

$$J\sigma_i = \lambda_i \frac{\partial W}{\partial \lambda_i} \tag{3.17}$$

where, λ_i's represent uniform dilatation. Our inputs to this model are shear modulus $G = 16MPa$, Poisson's ratio $\nu = 0.495$ and the density $\rho = 1.19g/cc$.

Since field variables (strain, temperature, etc) in the projectile, ring and output bar do not experience non-elastic effects, elastic models with proper values are used for those parts.

3.5 Numerical Results and Comparison

Experimental observations can be explained by the results from the finite element calculations. However, the accuracy and validity of numerical calculations should be verified. We compare the stress measured at the strain gages on the incident bar from the experiments to the stress at that location computed by numerical simulations. Figure (3.12) compares the experimental and numerical results for experiment P03, which has an input energy of 2800J. There is a very

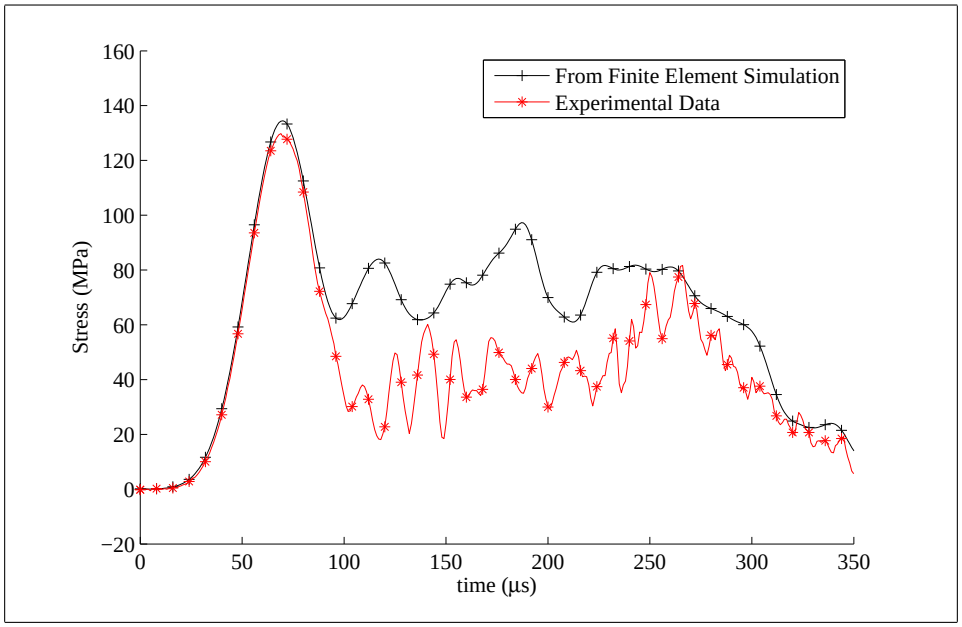

Figure 3.12: The time history of the transmitted force calculated from the finite element solution is compare to the experimental results.

close match in the beginning, the loading phase, and at the end, the release phase. The results during mid-phase are not promising and the problem needs to be investigated and the finite element model needs to be improved. The problem may be due to the fact that the failure was not modeled for these simulations. Therefore, more energy is transferred to the incident bar leading to a smaller decrease of transmitted force.

The deformation history of the sandwich sample is displayed in figure (3.13). The entire deformation process lasts about $140\mu s$. We first compare Von Mises stress contours of the steel plates on the front and the back. In figure (3.14), Von Mises stresses are plotted for all of the elements of the two steel plates. It is evident that the highest stresses occur at the center in the steel plate on the back, whereas for the front plate, the highest stresses occur at the edge of the rim. Therefore fracture at the center is expected for the back face (mode I) and for the front

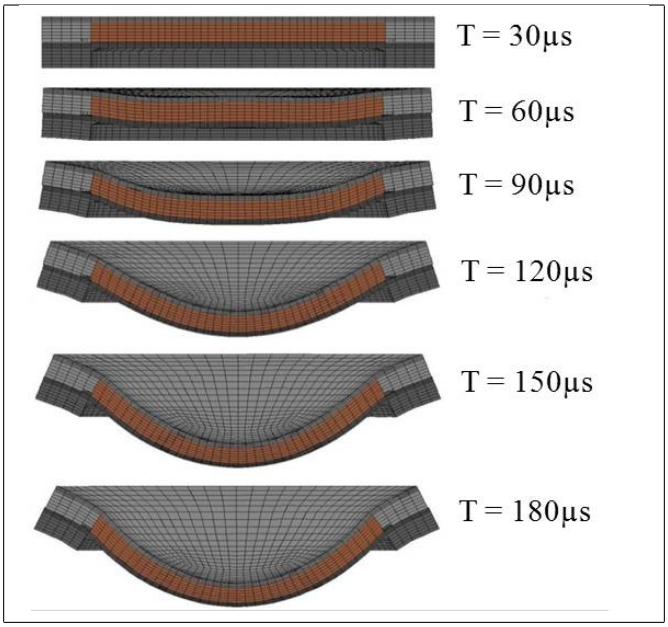

Figure 3.13: The deformation history of steel-polyurea sandwich structure. The model is split in half for illustration purposes.

plate, the second mode of failure is expected, which agrees with the experimental observations.

As another comparison metric, the amount of plastic deformation that the steel plates undergo during the course of deformation is considered at critical locations. The effective plastic strain is defined as:

$$\gamma(t) = \int_0^t \sqrt{\frac{2}{3}\mathbf{D}^p : \mathbf{D}^p}\ dt \tag{3.18}$$

where, $\mathbf{D}^p$ is the plastic part of the deformation rate tensor. Based on their experimental results, Amini et al. [68, 69] have noticed a correlation between this metric and the fracture of DH-36 steel plates and have used this metric as failure and fracture criteria in their numerical computations. The largest plastic deformation occurs at the central region of the steel plates. Therefore, the fracture/rupture is believed to initiate at this region. Consequently, we measure the volume average

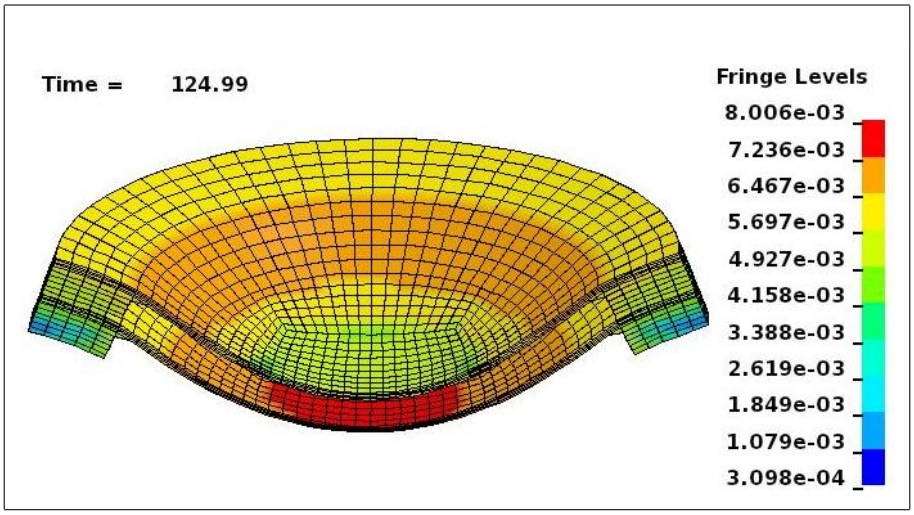

Figure 3.14: Von Mises stresses in the elements of the steel plates on the front and back. The highest stresses occur at the center of the back plate. The model is split in half for illustration purposes.

of the effective plastic strain corresponding to a circular region of diameter 10mm at the center of steel plates.

Figure (3.15) displays the volume average of effective plastic strain over the elements of the aforementioned circle for the steel plates on the front and the back. There is a substantial difference between the plastic deformation of the two plates. The plate that is confronting the impulsive load (front plate) experiences lower plastic deformation and remains intact. However, the back plate which experiences more plastic deformation fractures and, in that process, absorbs and dissipates energy serving as a sacrificial layer to save the front plate.

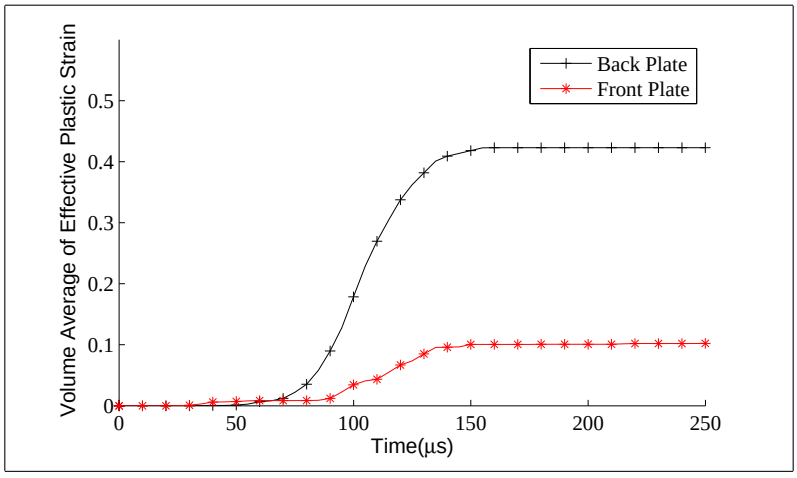

Figure 3.15: The volume average of effective plastic strain over a circle of 10mm diameter at the center of steel plates. The steel plate on the back undergoes higher plastic deformations and is more likely to fracture.

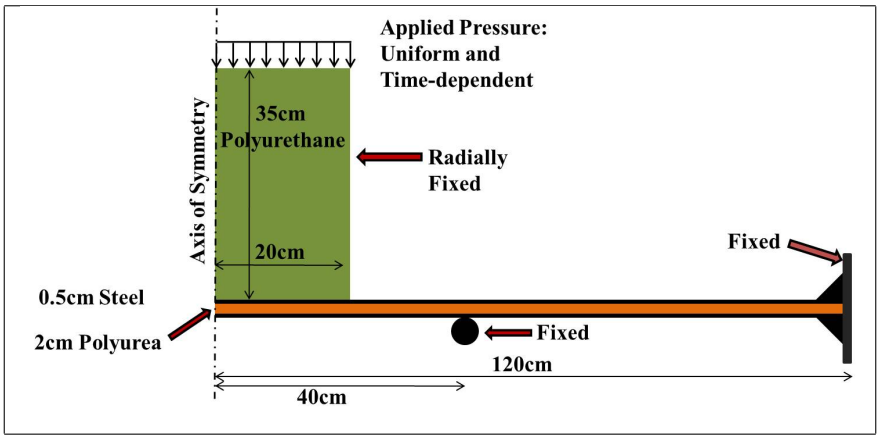

Figure 3.16: The geometry of the axi-symmetric model. A uniform time-varying impulsive load is applied to the top of the polyurethane cylindrical part, which is radially confined. The steel plates are extended far enough to avoid edge complications. The polyurea is sandwiched between the steel plates.

3.6 Axi-symmetric Finite Element Model (Large Scale)

To investigate the role of polyurea in sandwich structures with larger dimensions subjected to high-rate loadings, an axi-symmetric finite element model was developed. This numerical problem is designed and proposed to serve as a framework for our study on steel-polyurea-steel sandwich composites. Some remarkable features of this numerical model are:

- Element size: compared to a 3D model, an axi-symmetric model can include finer meshes with the same computational cost. This model is refined to obtain a mesh-size independent solution.
- Edge-effect: as shown in figure (3.16), the sandwich structure is extended far from the loading region to avoid possible edge complications.
- Fracture modeling: a failure/fracture criterion based on the value of effective plastic strain is included in this model.

To compare the performance of the sandwich structure subjected to impulsive loadings to that of bare steel, the model was modified to exclude polyurea and include a steel plate with the same thickness as the sandwich composite, while other conditions remained the same. The results from these models are displayed and compared in section (3.6.5).

3.6.1 Geometry and boundary assumptions

Figure (3.16) illustrates the geometry and details of the proposed numerical problem. A $2cm$ layer of polyurea is sandwiched between two steel plates of diame-

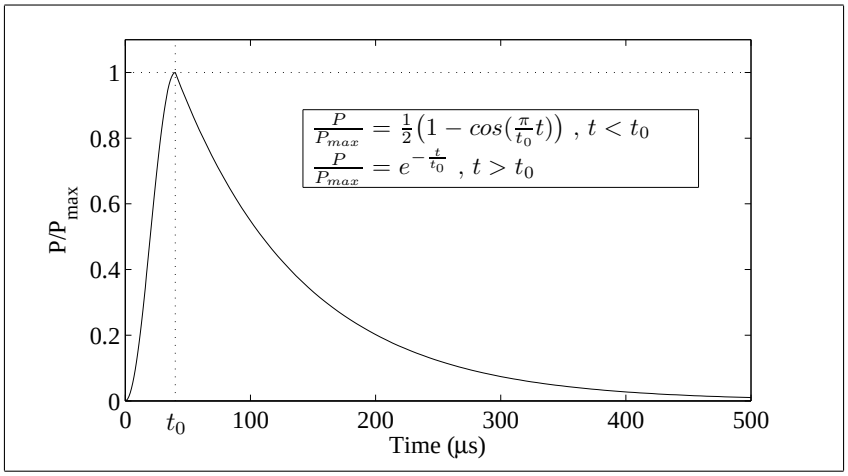

Figure 3.17: The time-history of the normalized pressure; the pressure rises within $40\mu s$ and exponentially declines, with a decay constant of $40\mu s$.

ter $1.2m$ and thickness $0.5cm$. As mentioned before, we refer to the side of the steel plate that receives the pressure pulse as the *front face*, and to the opposite side as the *back face*. A uniform time-varying pressure pulse is applied to the system through a medium with a relatively low impedance (*polyurethane* in figure 3.16). The shape and time-history of this impulsive pressure pulse is plotted in figure (3.17).

Direct application of the pressure pulse to the structure is avoided to attain a more physical and realistic scenario. In other words, employing polyurethane as a pressure-transmitting medium assures the capturing of the physics behind the impact phenomenon and wave interactions. The pressure pulse propagates through the polyurethane and, when it impacts the structure, a wave is generated at the interface which reflects back to the polyurethane. The height of the polyurethane is designed so that when the reflection of this wave from the top arrives back to the interface, the structure is completely detached from the polyurethane.

The polyurethane is radially fixed. As a result, the pressure pulse travels

through the polyurethane without losing its uniformity in shape. The circular steel plates are designed such that they experience the highest stresses and deformations at the central regions, leading to the first mode of failure explained in section (3.3). More specifically, steel plates are extended far from the polyurethane part to avoid edge complications. A fixed cylindrical wall is included to confine the deformation to a circle of $80cm$. Steel plates are fixed at $120cm$ from the center, which eliminates of the possibility of obtaining the highest stresses at the fixed edge.

3.6.2 Time-varying pressure pulse

The impulsive loading applied to the sandwich structure as a pressure pulse is assumed to vary in time as depicted below:

$$\frac{P}{P_{max}} = \frac{1}{2}\big(1 - cos(\pi\frac{t}{t_0})\big) \qquad for\ t < t_0 \tag{3.19}$$

$$\frac{P}{P_{max}} = e^{-\frac{t}{t_0}} \qquad for\ t > t_0 \tag{3.20}$$

where, t_0 is the rise-time, and P_{max} is the maximum pressure. In figure (3.17), the magnitude of pressure pulse versus time is plotted. The values of P_{max} and t_0 used in the simulations were $270MPa$ and $40\mu s$, respectively.

3.6.3 Failure criterion

To capture the fracture of steel plates, a criterion based on the nodal values of the effective plastic strain is introduced in this model. This criterion is only added to the section of steel underneath the polyurethane (a circle of radius $20cm$) within which the highest stresses and strains are observed. All the elements under consideration are created separately; i.e. adjacent elements do not share nodes. In other words, adjacent elements are not connected even though they share an

edge. Coincident nodes are then tied with one another using the LS-DYNA keyword *CONSTRAINED_TIED_NODES_FAILURE. When the nodal value of the effective plastic strain reaches a critical value, the tying condition is removed and nodes separate. The critical value for effective plastic strain in our simulations was 0.4.

3.6.4 Finite element solver

LS-DYNA was employed to carry out the calculations. Material models used for these simulations were the same as the 3-dimensional model explained in section (3.4.3). We highlight some of the essential LS-DYNA keywords employed in this model:

- *CONTACT_2D_AUTOMATIC_SURFACE_TO_SURFACE_TITLE:
  This keyword is used to define polyurethane-steel and steel-wall contact surfaces.

- *CONTACT_2D_AUTOMATIC_TIED_TITLE: This keyword was used to tie the nodes from the section of the steel that was under fracture criterion to the nodes from the rest of the steel at their interface (see section 3.6.3). Note that even though the nodes at the interface are coincident, they are not connected.

- *CONSTRAINED_TIED_NODES_FAILURE: Refer to section (3.6.3) for details.

All the calculations were carried out on a workstation with an Intel Pentium D 3.4GHz CPU and RedHat Enterprise 5.0 operating system. Total calculation time was about 2 hours.

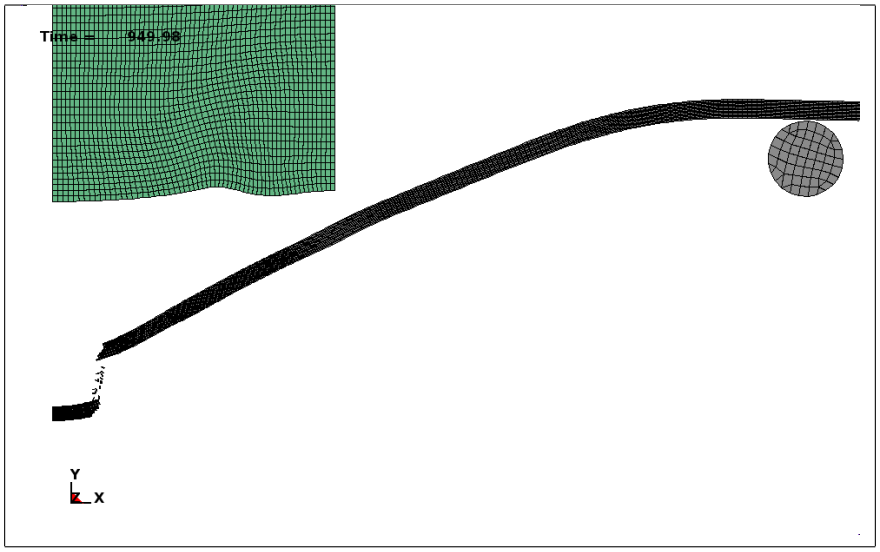

Figure 3.18: The shape of the steel plate at $t = 950\mu s$; the fracture does not occur at the center under the assumed fracture criterion.

3.6.5 Results and discussion

In this section, the performance and fracture mechanism of the two structures, steel-polyurea-steel and steel-only, subjected to the defined impulsive loading are compared. In figure (3.18), the shape of the steel-only structure at $t = 950\mu s$ is depicted. The fracture starts at $t \approx 700\mu s$, when the deflection of the center of the steel plate is about $11.69cm$. Numerical results reveal that, in this case, the fracture is not initiated from the center.

Figure (3.19) illustrates the shape of the steel-polyurea-steel sandwich structure at time $t = 950\mu s$. The fracture starts at $t \approx 800\mu s$ when the deflection of the center of the steel plate is about $11.70cm$. The results suggest that under this type of loading, the steel plate on the back fractures, whereas no fracturing occurs on the front plate. It is also clear that the fracture on the back face does not start from the center. This agrees with experimental observations from some of our tested samples. Figure (3.20) demonstrates the final shape and fracture of the back

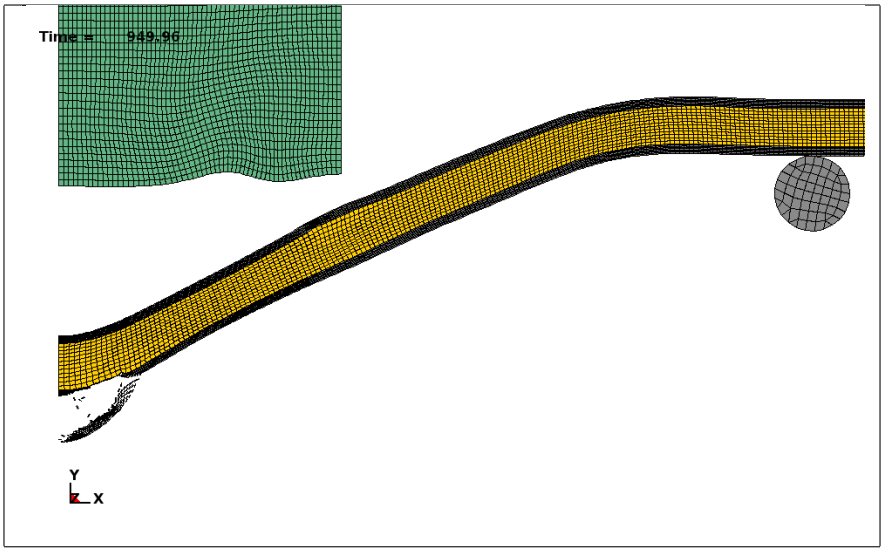

Figure 3.19: The shape of the sandwich structure at $t = 950\mu s$; the steel plate on the back is fractured while the steel plate on the front, which receives the impulsive loading, remains intact. In this case, the fracture does not start from the center.

plate of a sandwich structure after the experiment. Although in the experiment the geometry and loading condition were different from the simulations, the same trend can be observed. In other words, the fracture did not start from the center in both cases.

In comparison, the steel-polyurea-steel sandwich structure demonstrates a different behavior compared to the steel-only structure subjected to impulsive loading. The remarkable fact that the front plate is saved from fracturing can be viewed as a potential for applications where the leakage of a substance into the system is of great danger, for example after a blast or an accident. However, it is necessary to regard that these results can not be generalized to all types of loading and conditions without further exploration.

Figure 3.20: The back plate from the experiment *HH4* after the impact test. The fracture does not occur at the center. This trend, which is predicted by the numerical model, is observed in a few, but not all, of the tested samples.

3.7 Summary and Conclusion

The results from experiments and numerical modeling of steel-polymer-steel sandwich structures subjected to high-rate loadings have been presented. To study the dynamic response, failure and fracture of such structures under impulsive loadings, a set of impact experiments was performed on circular steel-polyurea-steel sandwich specimens using a 3" Hopkinson bar setup. The experimental results from these experiments are limited to the final sample shape and the time-history of force transmitted through the sample. The entire experiment was numerically modeled in a finite element software package (LS-DYNA) to study the impact process in depth. Numerical results were found to be in good agreement with experimental data indicating the accuracy and validity of the material models used for polyurea and steel under these loading conditions.

In addition to the aforementioned effort, an independent numerical study was performed on steel-polyurea-steel sandwich structures with larger dimensions.

The goal was to investigate whether the same trend could be observed when the scale of the problem is different. Accordingly, an axi-symmetric finite element model was designed and developed allowing for fine meshes and yet a reasonable computational cost.

From experimental and numerical results, it is observed that when a steel-polyurea-steel sandwich structure is exposed to impulsive loading, the steel plate facing the load is more likely to survive whereas the steel plate on the opposite side experiences fracture. In other words, the plate on the back side with respect to the impact, serves as a sacrificial layer and fractures, thereby saving the steel plate on the load-receiving side.

3.8 Acknowledgments

The experimental work has been conducted at the Center of Excellence in Advanced Materials (CEAM), Mechanical and Aerospace Engineering Department, University of California, San Diego, by the author and Mr. Jon Isaacs, and has been supported by the ONR grant N00014-06-1-0340. This work is prepared for publication by A. Samiee, J. Isaacs and S. Nemat-Nasser. The author of this dissertation is the primary investigator of this work.

Chapter 4

Ballistic Performance of Polyurea-Coated Armor Grade Ceramic Tiles and Steel Plates

Experiments have been conducted to study the ballistic performance of polyurea-ceramic and polyurea-steel layered composites. The application of ceramics as blast resistant materials has been studied by many researchers. Recent studies suggest a 25% improvement in the ballistic performance of ceramics, when they are restrained by thin layers of certain materials, such as E-glass/epoxy and carbon-fiber/epoxy [70]. Any modification to the ceramic or steel structure that enhances the energy absorbing properties of the system is significant. In this study, the effect of *polyurea* - an excellent energy dissipating agent - on the blast resisting properties of the resulting ceramic- and steel-based composites is investigated.

Polyurea is cast on top or in between layers of ceramic tiles or steel plates to fabricate layered structures. Sets of penetration tests have been carried out on these composites. In the experiments, a high velocity projectile is propelled to impact

and perforate the layered composite. The velocity and the mass of the projectile are measured before and after the penetration. The change in the kinetic energy of the projectile is considered as a metric for comparing the ballistic performance of the different composites. Experimental results suggest that polyurea is not as effective as other restraining materials, such as E-glass/epoxy and carbon-fiber/epoxy, in the case of ceramic-based composites. For steel-based composites, the superior performance is observed when polyurea is cast on the side facing the blast.

4.1 Introduction

The application and variety of ceramics have been continuously increasing over the past few decades. The dynamic mechanical properties of ceramics has become a subject of interest over the last two decades. The problem of the ballistic performance of ceramic targets has been tackled by many researchers and a few repeatable facts have been established. Most of the experiments have involved a high strength alloy projectile penetrating a ceramic target at a velocity range of 0.5-5.0 km/s. Using highspeed photography and flash radiography, it has been observed that the ceramic ahead of the projectile pulverizes and is ejected from the front and back faces of the ceramic. The process of fragmentation and the size of fragments have been studied. Experimental results from different researchers suggest that the process of pulverization and the fragmentation of the ceramic is directly related to the ballistic performance of the ceramic tiles.

Bless et. al. [71] have reported that the penetration resistance of alumina decreases with velocity for armor-piercing bullets and is relatively independent of velocity for rods and fragment-simulating projectiles. Rosenberg et. al. [72] have conducted a series of terminal ballistic experiments with small scale tungsten alloy

penetrators with impact velocities ranging between 1.25 to 3.0 km/s in order to quantify the ballistic efficiency of confined ceramic tiles and found that the differential ballistic efficiency of alumina tiles is practically independent on impact velocity and the tile thickness.

Lundberg et. al. [73] have investigated the penetration of long tungsten projectiles into the steel-backed alumina targets and concluded that the laws of replica-scaling hold with sufficient degree of accuracy to justify scaled-down experiments. Orphal and Franzen [74] measured the penetration of simple confined boron carbide targets by long tungsten rods with impact velocities ranged from 1.5 to about 5.0 km/s and observed an initial steady state penetration. Shockey et. al. [75] have suggested that non-conventional material properties such as the dynamic compressive failure energy and the friction, flow and abrasive properties of the finely fragmented material govern the penetration resistance of confined ceramics.

Woodward et. al. [76] have conducted experiments in which both confined and unconfined ceramic targets are perforated by pointed and blunt projectiles and established a correlation between increased degree of fragmentation and reduced ceramic toughness. They attributed the fine fragments to crushing ahead of the impacting projectile, and coarse fragmentation to the interaction of stress relief waves to explain the effects of confinement in terms of a simple model for loading and stress relief during perforation. Curren et. al. [77] present a micro-mechanical model to describe the non-elastically deformation of ceramics which is caused by sliding and ride-up of fragments and suggest that friction, flow and abrasive properties of the fine fragments govern the penetration resistance of ceramics.

Sarva et. al. [70] have reported a 25% improvement in ballistic efficiency of armor grade Al_2O_3 and SiC tiles by restraining the impact face of ceramics by materials such as E-glass/epoxy, carbon-fiber/epoxy and Ti-3%Al-2.5%V alloy.

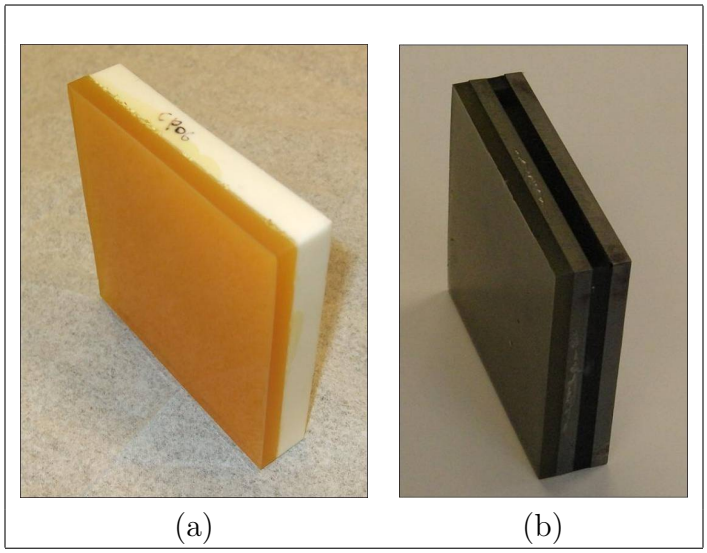

Figure 4.1: $\frac{1}{4}$-inch polyurea layer cast on a $\frac{1}{2}$-inch armor grade ceramic tile (Alumina based)

They have shown that the thin membrane restraint restricts the flow of pulverized ceramic debris and causes more resistance to penetration. By comparing the grain size of ceramics and the pulverized fragments, they have observed that the pulverization is the result of a sub-grain level failure mechanism.

In this study, we have investigated the effect of adding a polyurea layer on the ballistic efficiency of ceramic tiles and steel plates by performing perforation tests on polyurea-ceramic and polyurea-steel composites. A high speed projectile impacts the composite and the velocity and weight of the projectile are measured before and after the impact. The change in the kinetic energy of the projectile has been evaluated and compared for different polyurea-ceramic and steel-polyurea configurations (e.g. polyurea on the front, polyurea on the back, etc.).

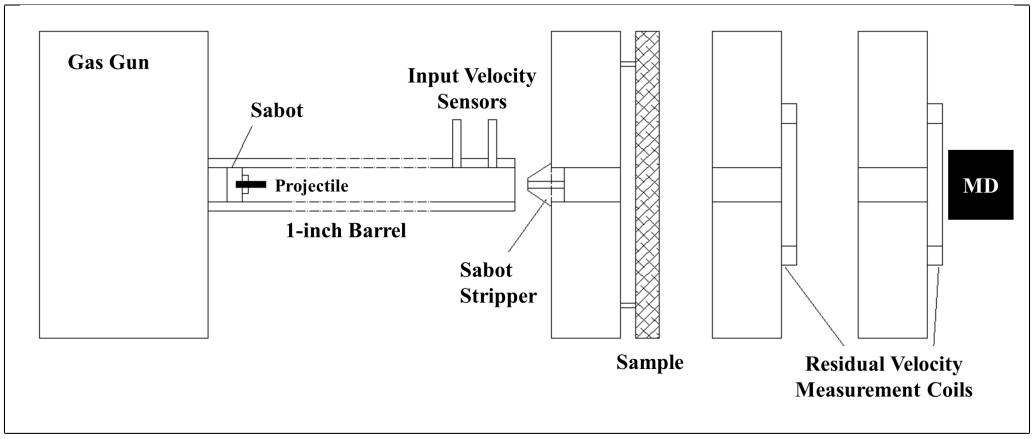

Figure 4.2: Schematic view of the components of the experimental setup. Note that the components are not drawn to scale. MD: Momentum Dump

4.2 Materials and Experimental Setup

Layered composites were fabricated at UCSD/CEAM's material processing labs. Polyurea was made by mixing Isonate 2143L [78] and Versalink P1000 [79] with a five percent excess of Isonate 2143L to produce a lightly cross-linked polymer [80]. $\frac{1}{2}$-inch and $\frac{1}{4}$-inch armor grade Al_2O_3 ceramic tiles and DH-36 naval structural steel with variety of thicknesses were used to fabricate ceramic-polyurea and steel-polyurea layered composites, respectively. In figure (4.1a), a $\frac{1}{2}$-inch ceramic tile coated with a $\frac{1}{4}$-inch layer of polyurea is depicted. Figure (4.1b) displays a layered composite with 2 steel layers and 2 polyurea layers, where all layers have the same thickness of $\frac{1}{4}$-inch.

Figure (4.2) illustrates the schematic view of the experimental setup. The components are not drawn to scale. Penetration tests were conducted at UCSD/CEAM's gas gun facilities laboratory. A $\sim$10.6g flat-ended cylindrical projectile (diameter 6mm, length 20mm), machined from tungsten heavy alloy (WHA) was employed as the penetrator. The projectile is carried by an aluminum part, referred to as

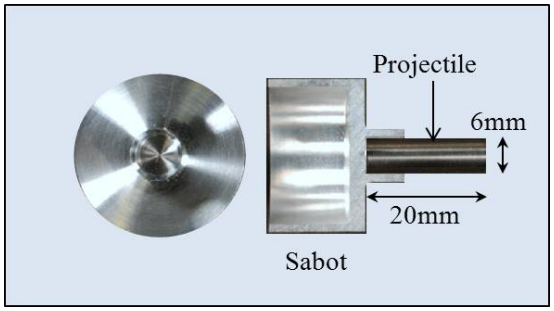

Figure 4.3: Projectile and its aluminum carrier (sabot)

a *sabot*. In figure (4.3), the projectile and its ∼7g aluminum carrier (sabot) are depicted.

The experimental procedure is as follows: The sabot-projectile assembly is placed in the gas gun barrel, which has a 1-inch (2.54cm) diameter and 16-feet (5m) length. The gun is pressurized to ∼ 2400 psi by helium; and when manually triggered, the gas is released behind the sabot, propelling it towards the target. The projectile reaches a velocity of ∼900m/s before penetrating the sample. The sabot is removed from the projectile by a component made of high strength steel, and labeled as *sabot stripper*.

The impact velocity is measured by two velocity sensors placed at the end of the barrel before the sabot-stripper. The velocity of the projectile after the impact is measured by two magnetic coil residual velocity sensors. The projectile after the impact is slightly magnetic due to the iron content in its composition. After the impact, the magnetized projectile passes through the coils inducing an electromagnetic pulse, which is measured by a digital oscilloscope. The time difference between the peaks of these pulses and the distance between the two coils are used to calculate the residual velocity of the projectile.

The eroded projectile has a large amount of momentum even after the

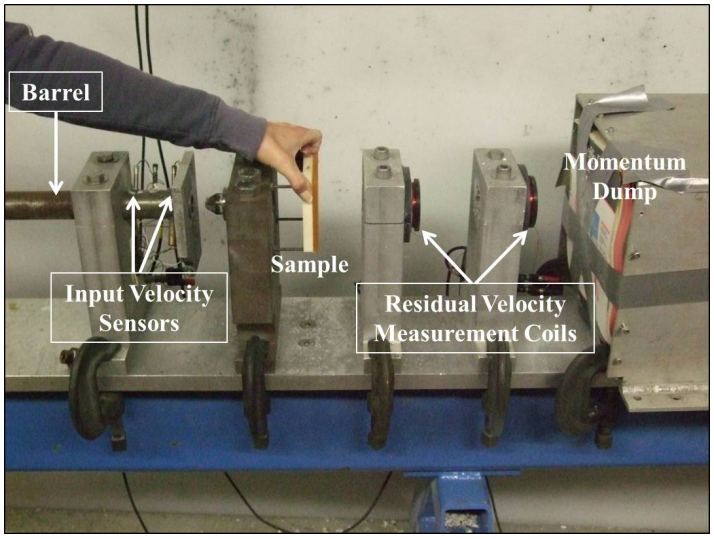

Figure 4.4: : The projectile-sabot assembly arrives at the end of the barrel with a velocity of approximately 900m/s. Sabot is removed by the sabot-stripper before the projectile penetrates the sample. After the impact, the projectile passes through the residual velocity measurement coils and is stopped by the bulk paper stack (momentum dump).

impact. A bulk paper stack, labeled as *momentum dump*, is placed after the coils to stop and recover the remainder of the projectile. In figure (4.4), the experimental setup - from the end of the barrel to the momentum dump - is displayed. In figure (4.5), the projectile before and after the impact is displayed. Eroded projectiles are from the experiments on bare ceramic samples.

Figure 4.5: The projectile before and after the penetration. Eroded projectiles are from the experiments on bare ceramic samples.

4.3 Results I: Ceramic-Polyurea Composites

Two sets of experiments were conducted on ceramic-polyurea samples. The first set contains 3 bare ceramic samples, 2 ceramic-polyurea samples and 3 carbon fiber-ceramic-polyurea samples. The results are presented in table (4.1). The position of polyurea with respect to the penetration side and the increase to the areal density of the ceramic tiles are specified for each sample in separate columns. PU-Front refers to cases that the projectile first penetrates the polyurea side of the sample. PU-Back refers to cases that the penetration occurs from the steel side of the sample.

Table 4.1: Results of the first set of the experiments on polyurea-ceramic composites. EE: e-glass/epoxy, F(x): x layers of carbon fiber; polyurea is cast on the back in all EE cases.

Exp. No.	Polyurea Position	Projectile Velocity Drop (%)	Projectile Mass Drop (%)	Areal Density Increase (%)	Kinetic Energy Drop (%)
1	No PU	28	44	-	71
2	No PU	26	42	-	68
3	No PU	28	48	-	73
4	PU-Front	33	50	14	77
5	PU-Back	33	55	12	80
6	EE-F(16)/PU	36	62	27	84
7	EE-F(3)/PU	45	58	8	87
8	EE-F(3)/PU	43	53	9	85

The kinetic energy reduction is a function of the velocity decrease and weight loss of the projectile. After the impact, The remainder of the projectile is recovered to measure the weight loss due to erosion. In some cases, the projectile completely fragmented upon impact, and it was not possible to recover all of the pieces to obtain complete results. Figures (4.6) and (4.7) show the ceramic tiles after impact for different cases.

The polyurea layer has a thickness of approximately $\frac{1}{4}$-inch and weighs

$\sim$60g; this equates to a $\sim$13 percent areal density increase for the 510g ceramic tile. Experimental results reveal that the ballistic performance of ceramic tiles is improved (at most) by 10% when polyurea is cast on them.

A second set of experiments were conducted to verify the results from the first set. Samples include 3 bare ceramic tiles, 3 polyurea($\frac{1}{4}$")-ceramic($\frac{1}{2}$") composites, 2 ceramic($\frac{1}{4}$")-polyurea($\frac{1}{4}$")-ceramic($\frac{1}{4}$") sandwich composites. The major differences between the two sets are as follows:

- Ceramic-polyurea samples for the second set were fabricated more systematically; they all exhibit 13% areal density increase.
- A different design of sabot-stripper was used.
- A new digitizer with a higher sampling rate was employed.

Table (4.2) presents the results of the second set of experiments. Up to 12% improvement in ballistic performance is observed in ceramic-polyurea cases as evident when comparing experiments cp41 and cp43 to experiments cp31 and cp 32. Ceramic-polyurea-ceramic sandwich composites (experiments cp21 and cp22) exhibit a slightly inferior performance than ceramic-polyurea samples.

Table 4.2: Results of the second set of the experiments on polyurea-ceramic composites

Exp. No.	Polyurea Position	Projectile Velocity Drop (%)	Projectile Mass Drop (%)	Areal Density Increase (%)	Kinetic Energy Drop (%)
cp41	PU-Front	24	54	13	73
cp42	PU-Back	?	34	13	?
cp43	PU-Front	28	44	13	71
cp31	NO PU	24	35	0	62
cp32	NO PU	21	33	0	58
cp21	Sandwiched	33	33	13	70
cp22	Sandwiched	33	33	13	70
cp23	NO PU	23	33	0	61

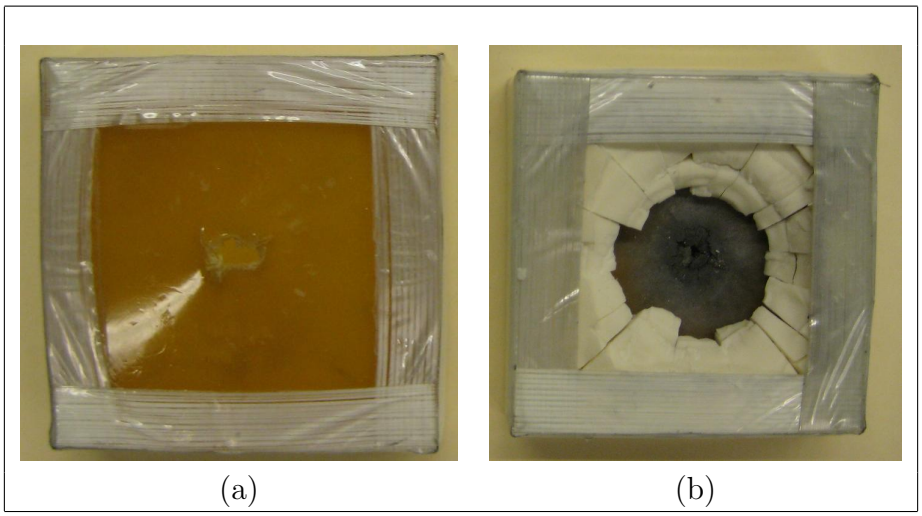

Figure 4.6: Ceramic tiles with polyurea coating after the impact: (a) polyurea cast on the back - back view, (b) polyurea cast on the back - front view.

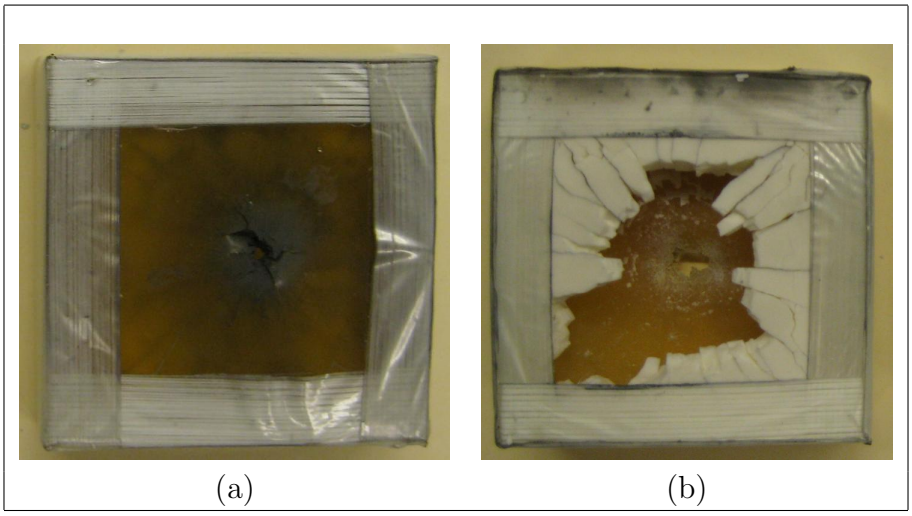

Figure 4.7: Ceramic tiles with polyurea coating after the impact: (a) polyurea cast on the front - back view, (b) polyurea cast on the front - front view.

Experimental results reveal that a slight improvement in ballistic performance of ceramic tiles can be achieved by coating them with polyurea; however, polyurea does not seem to be as effective as other restraining materials, such as E-glass/epoxy and carbon-fiber/epoxy, when added to ceramic structures to improve the ballistic efficiency. In other words, it exhibits lower ballistic performance while adding more areal density to the system.

4.4 Results II: Steel-Polyurea Composites

Penetration tests have been conducted on steel-polyurea layered composites to investigate the effect or polyurea on ballistic performance of steel plates. The experimental setup described in section (4.2) was employed to carry out the penetration tests. Various samples with different thicknesses and configurations were fabricated at UCSD/CEAM's material processing laboratory (some depicted in figure 4.8):

1. bare: no polyurea is cast on steel (experiments b1 and b2).

2. 1/2"(s-pu): consists of one layer of steel and one layer of polyurea, both having $\frac{1}{2}$" thickness (experiments s3-s6).

3. 1/4"(s-pu-s-pu): consists of two layers of steel and two layers of polyurea, all having $\frac{1}{4}$" thickness (experiments s7 and s8).

4. 1/4"s-1/2"pu-1/4"s: one $\frac{1}{4}$"-thick layer of polyurea is sandwiched between two steel plates with $\frac{1}{4}$" thickness (experiments s9-s11).

5. 1/6"(s-pu-s-pu-s-pu): consists of 3 layers of steel and 3 layers of polyurea, all having $\frac{1}{6}$" thickness (experiments s12 and s13).

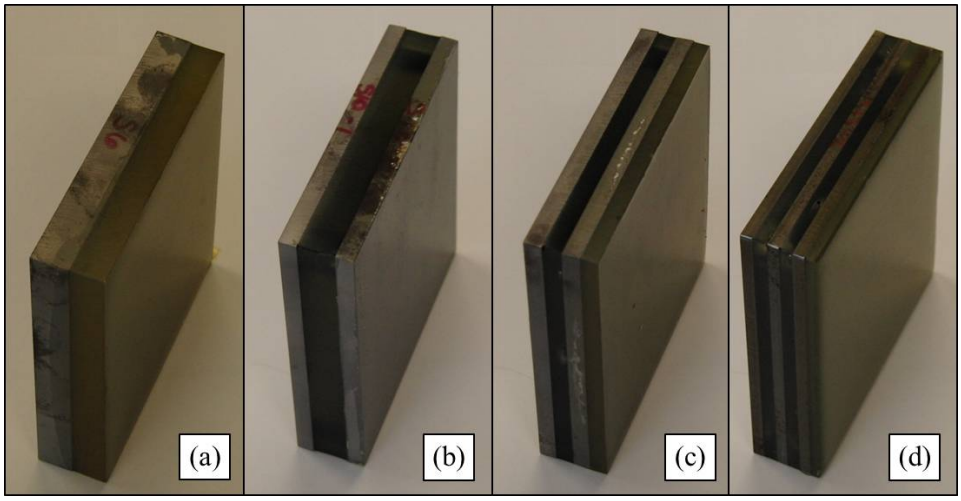

Figure 4.8: Different steel-polyurea layered composites: (a) 1/2"(s-pu) (b) 1/4"s-1/2"pu-1/4"s (c) 1/4"(s-pu-s-pu) (d) 1/6"(s-pu-s-pu-s-pu)

Experimental results are presented in tables (4.3) and (4.4). Consistent results are obtained within samples with the same configuration. Note that the total thickness of all polyurea-steel samples is 1.0". Among all configurations, 1/2"(s-pu) shows a noticeably superior ballistic performance.

4.5 Summary and Conclusion

Experiments have been conducted to study the ballistic performance of ceramic- and steel-based layered composites. In this study, the effect of polyurea - an excellent energy dissipating agent - on the blast resisting properties of the ceramic-polyurea and steel-polyurea layered composites are investigated.

Polyurea is cast on top or in between layers of ceramic tiles or steel plates to fabricate layered structures. A set of penetration tests have been carried out on these composites. In the experiments, a high velocity projectile is propelled to impact and perforate the layered composite. The velocity and the mass of the

Table 4.3: Details and results of experiments on polyurea-steel composites: m_1 and m_2 are the mass of projectile before and after the impact, respectively; Δt_1 and Δt_2 are the time difference between the peak of the signals measured from the input sensors and output sensors, respectively. The starred number is an estimate due to the lack of reliable experimental data.

Exp.	Configuration	Polyurea Position	m_1 (gr)	m_2 (gr)	Δt_1 (μs)	Δt_2 (μs)
b1	bare	-	10.6300	8.1927	56.8	303.5
b2	bare	-	10.5669	7.874	57.2	331.2
s3	1/2"(pu-s)	Front	10.4707	8.8061	56.7	429.1
s4	1/2"(pu-s)	Front	10.5843	9.0879	56.7*	430.5
s5	1/2"(s-pu)	Back	10.5807	7.7752	56.7	342
s6	1/2"(s-pu)	Back	10.6276	8.0257	56.4	342.9
s7	1/4"(s-pu-s-pu)	Sandwich	10.5272	9.167	56	348
s8	1/4"(s-pu-s-pu)	Sandwich	10.6469	9.0845	55.1	332.1
s9	1/4"s-1/2"pu-1/4"s	Middle	10.5383	9.2911	56.4	326.2
s10	1/4"s-1/2"pu-1/4"s	Middle	10.633	9.4387	56.2	323
s11	1/4"s-1/2"pu-1/4"s	Middle	10.6324	9.4879	56.2	324.4
s12	1/6"(s-pu-s-pu-s-pu)	Sandwich	10.6351	9.3988	56.5	368.4
s13	1/6"(s-pu-s-pu-s-pu)	Sandwich	10.6335	8.5783	56.4	372.9

Table 4.4: Results of experiments on polyurea-steel composites.

Exp.	Configuration	Mass Drop (%)	Velocity Drop (%)	Energy Drop (%)
b1	bare	22.93	43.76	75.62
b2	bare	25.48	48.10	79.93
s3	1/2"(pu-s)	15.90	60.29	86.74
s4	1/2"(pu-s)	14.14	60.42	86.55
s5	1/2"(s-pu)	26.52	50.18	81.76
s6	1/2"(s-pu)	24.48	50.57	81.55
s7	1/4"(s-pu-s-pu)	12.92	51.64	79.64
s8	1/4"(s-pu-s-pu)	14.67	50.14	78.79
s9	1/4"s-1/2"pu-1/4"s	11.83	48.04	76.20
s10	1/4"s-1/2"pu-1/4"s	11.23	47.71	75.73
s11	1/4"s-1/2"pu-1/4"s	10.76	47.94	75.82
s12	1/6"(s-pu-s-pu-s-pu)	11.62	53.91	81.23
s13	1/6"(s-pu-s-pu-s-pu)	19.33	54.55	83.34

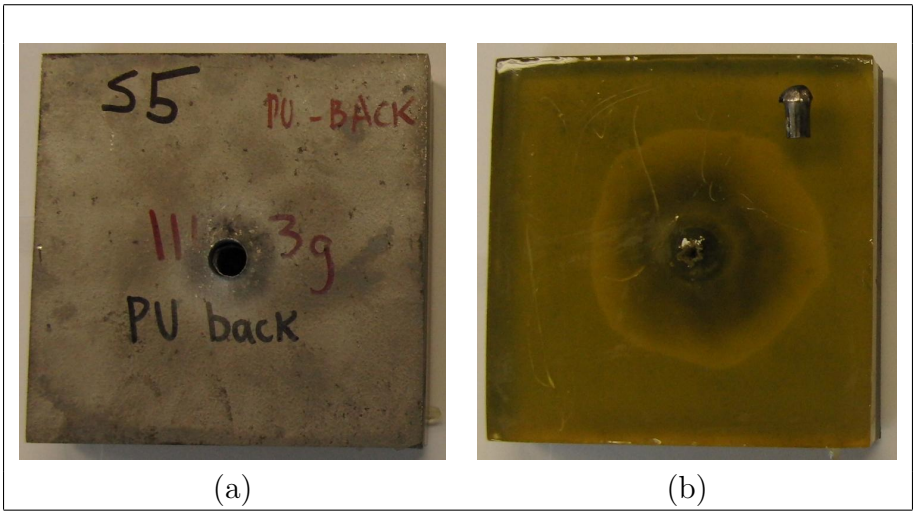

(a) (b)

Figure 4.9: Steel-polyurea composites after the penetration test for the experiment s5: (a) polyurea cast on the back - front view, (b) polyurea cast on the back - back view; the deformed projectile is also displayed on the top-right corner.

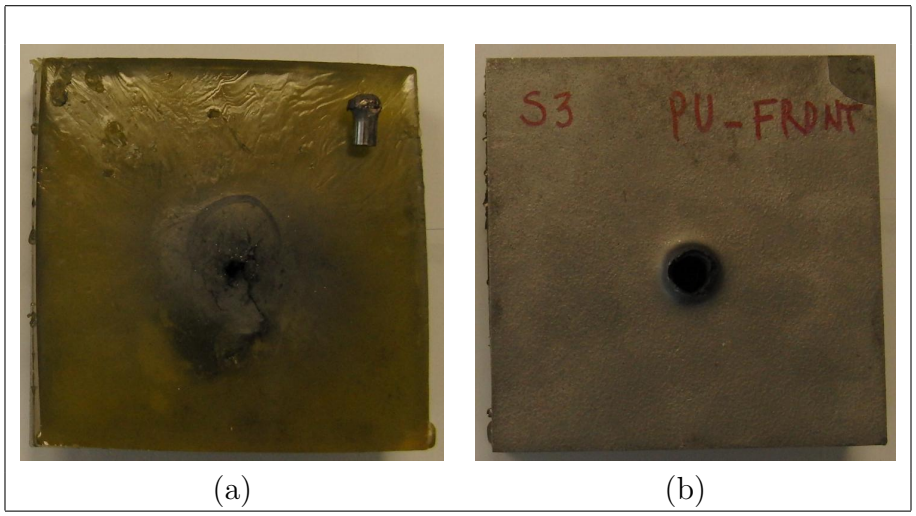

(a) (b)

Figure 4.10: Steel-polyurea composites after the penetration test for the experiment s3: (a) polyurea cast on the front - front view; the deformed projectile is also displayed on the top-right corner, (b) polyurea cast on the front - back view

projectile are measured before and after the penetration. The change in the kinetic energy of the projectile is considered as a metric for comparing the ballistic performance of different composites.

Experimental results suggest that polyurea is not as effective as other restraining materials such as E-glass/epoxy and carbon-fiber/epoxy in the case of ceramic-based composites. For steel-based composites, the superior performance is observed when polyurea is cast on the side facing the blast.

4.6 Acknowledgments

This experimental work has been conducted at the Center of Excellence for Advanced Materials (CEAM), Mechanical and Aerospace Department, University of California San Diego, and has been supported by the Office of Naval Research (ONR) grant N00014-06-1-0340. This work was a collaborative effort by Mr. J. Isaacs, Dr. Kirstin Schaaf, Mr. R. Griswold and the dissertation author.

Chapter 5

Wave Propagation in Layered Cylindrical Bars

In this chapter, a semi-analytical method to approximate the solution of the wave propagation problem in periodic layered cylindrical bars is presented. This method develops upon Rythov's classical solution of plane harmonic waves in periodic layered composites and employs the Pochhammer-Chree solutions to account for Poisson's effect in a finite cross-section. This method is then employed to calculate the dispersion curve for a periodic steel-aluminum cylinder. A dispersion correction routine is developed to obtain the shape of a given pulse at any given location on the periodic bar. Finite Element Method (FEM) is employed to verify the accuracy of this method. The dispersion solutions calculated from this method for periodic cylinders, therefore, are in closer agreement to FEM simulations than the Rythov dispersion solution.

5.1 Introduction

The most comprehensive solution to the propagation of longitudinal waves in elastic infinite layered media was first published by Rytov [81]. Many others developed continuum theories to address the wave propagation problem in laminated and fiber reinforced composites [82, 83]. Harmonic waves in periodic structures and elastic composites was the subject of interest in many other attempts [84, 85, 86]. The solutions revealed the dispersive nature of laminated/periodic composites, and many researchers have attempted to obtain dispersion curves for layered materials. For instance, Minagawa *et. al.* presented dispersion curves for two-dimensional layered, fiber-reinforced, and other elastic composites [87]. Verification of the analytical results has remained a tough challenge.

The exact solution to the wave propagation problem in elastic cylinders exists (Pochhammer (1876) and Chree (1889)). It has also been shown that elastic cylindrical bars are dispersive media, and the dispersion relation for these media has been obtained [1]. This information has been employed to develop methods to estimate the shape changes of traveling pulses in cylinders for applications such as Split Hopkinson Pressure Bar [88]. This method, known as *dispersion correction*, exhibits a near perfect match to experimental results; and therefore, can be used as a robust tool for verifying the dispersion relation, which is obtained analytically. Inspired by this, I have attempted to obtain the dispersion relation for layered cylindrical bars. The solution has been verified by using the dispersion correction method.

In this chapter, I have employed Finite Element Method (FEM) to solve examples of propagation of pressure pulses in a steel-aluminum layered cylinder. I have proposed an approximate semi-analytical method to obtain the dispersion

relation for layered cylinders. Then, I have developed a special dispersion correction routine for layered media capable of estimating the shape changes of traveling pulses. The finite element results are compared to the results for the dispersion correction method to verify the accuracy of the proposed solution.

5.2 Solution of Wave Equations

In this section, the solution of wave equations for cylindrical elastic bars is reviewed. This classic problem was first solved by Pochhammer (1876) and independently by Chree (1889). For a more detailed discussion on this subject refer to Redwood [89], from which most of the equations in this section are adopted.

It is more convenient to treat this problem in cylindrical coordinates (r θ and z), and in terms of potential functions. The governing equations for the propagation of elastic waves in a cylindrical bar in terms of potential functions ϕ and ψ are as follows:

$$\frac{\partial^2\phi}{\partial t^2} + \frac{1}{r}\frac{\partial\phi}{\partial r} + \frac{\partial^2\phi}{\partial z^2} = \frac{1}{c_d^2}\frac{\partial^2\phi}{\partial t^2} \tag{5.1}$$

$$\frac{\partial^2\psi}{\partial t^2} + \frac{1}{r}\frac{\partial\psi}{\partial r} + \frac{\partial^2\psi}{\partial z^2} = \frac{1}{c_t^2}\frac{\partial^2\psi}{\partial t^2} \tag{5.2}$$

where c_d and c_t are the speeds of *dilatational* and *shear* waves, respectively:

$$c_d^2 = (\lambda + 2\mu)/\rho \quad , \quad c_t^2 = \mu/\rho \tag{5.3}$$

where, λ and μ are Lamé constants and ρ is the density of the elastic bar. In this problem, the angular deformation (torsion) is not considered, and all the equations are independent of θ.

We consider the propagation of a harmonic wave with angular velocity ω along the axis of the bar. In an elastic media with no loss, all quantities are

harmonic with frequency ω,

$$\phi = \phi_0(r)e^{i(\omega t - k_0 z)} \quad , \quad \psi = \psi_0(r)e^{i(\omega t - k_0 z)} \tag{5.4}$$

where, k_0 is the wave number, which is related to the wavelength, Λ, by $\Lambda = 2\pi/k_0$. Substituting equations (5.4) into the wave equations (5.1) results in two Partial Differential equations (PDE):

$$\frac{\partial^2 \phi_0}{\partial r^2} + \frac{1}{r}\frac{\partial \phi_0}{\partial r} + \Big[\big(\frac{\omega}{c_d}\big)^2 - k_0^2\Big]\phi_0 = 0 \tag{5.5}$$

$$\frac{\partial^2 \psi_0}{\partial r^2} + \frac{1}{r}\frac{\partial \psi_0}{\partial r} + \Big[\big(\frac{\omega}{c_t}\big)^2 - k_0^2\Big]\psi_0 = 0 \tag{5.6}$$

The most general solution to these PDE's contains Bessel and Neumann functions; however, to have a finite solution at $r = 0$, the solution can only exist in terms of Bessel functions:

$$\phi = AJ_0(k_d r)e^{i(\omega t - k_0 z)} \tag{5.7}$$

$$\psi = CJ_0(k_t r)e^{i(\omega t - k_0 z)} \tag{5.8}$$

where,

$$k_d^2 = (\omega/c_d)^2 - k_0^2 \quad , \quad k_t^2 = (\omega/c_t)^2 - k_0^2 \tag{5.9}$$

The potential functions, ϕ and ψ, are related to u_r and u_z as follows:

$$u_r = \frac{\partial \phi}{\partial r} + \frac{\partial^2 \psi}{\partial r \partial z} \tag{5.10}$$

$$u_z = \frac{\partial \phi}{\partial z} - \frac{\partial^2 \psi}{\partial r^2} - \frac{1}{r}\frac{\partial \psi}{\partial r} \tag{5.11}$$

Substitute the solution of potential functions into equations (5.10) and (5.11) to obtain u_r and u_z:

$$u_r = \{-k_d A J_1(k_d r) + ik_0 k_t C J_1(k_t r)\}e^{i(\omega t - k_0 z)} \tag{5.12}$$

$$u_z = \{-ik_0 A J_0(k_d r) + k_t^2 C J_0(k_t r)\}e^{i(\omega t - k_0 z)} \tag{5.13}$$

The only non-zero stresses in this problem are:

$$\sigma_{rr} = \lambda \left\{ \frac{u_r}{r} + \frac{\partial u_r}{\partial r} + \frac{\partial u_z}{\partial z} \right\} + 2\mu \frac{\partial u_r}{\partial r} \tag{5.14}$$

$$\sigma_{zr} = \mu \left\{ \frac{\partial u_r}{\partial z} + \frac{\partial u_z}{\partial r} \right\} \tag{5.15}$$

At the radial boundary ($r = a$), these stresses must vanish. This leads to the following system of homogeneous equations:

$$\begin{aligned} A\Big\{ \frac{1}{2}(k_t^2 - k_0^2) J_0(k_d a) + \frac{k_d}{a} J_1(k_d a) \Big\} + \\ + C\Big\{ i k_0 k_t^2 J_0(k_t a) - \frac{i k_0 k_t}{a} J_1(k_t a) \Big\} = 0 \end{aligned} \tag{5.16}$$

$$A\big\{ 2 i k_0 k_d J_1(k_d a) \big\} - C\big\{ k_t^3 - k_0^2 k_t \big\} J_1(k_t a) = 0 \tag{5.17}$$

Non-trivial solutions to this system of equations exist, only when the determinant of the corresponding matrix vanishes. This yields *the characteristic equation*:

$$k_0^2 \frac{k_t J_0(k_t a)}{J_1(k_t a)} - \frac{1}{2}\left(\frac{\omega}{c_t}\right)^2 \frac{1}{a} + \left\{ \frac{1}{2}\left(\frac{\omega}{c_t}\right)^2 - k_0^2 \right\}^2 \frac{J_0(k_d a)}{k_d J_1(k_d a)} = 0 \tag{5.18}$$

The characteristic equation, or *the dispersion relation*, relates the frequency, ω, to the phase velocity, k_0, for given bar radius and material properties. This indicates that the velocity of a propagating wave in a cylindrical bar is a function of frequency. Therefore, the shape of a given pressure pulse composed of a range of frequencies, is subject to modification while traveling in the bar. This phenomenon is referred to as *dispersion*.

The most comprehensive solution of the characteristic equation was first published by Bancfort [1]. The solution contains multiple roots, corresponding to the various modes of vibration of the bar. Bancroft has plotted the solution for the first mode of vibration for different Poisson ratios. This plot is reproduced here for steel and aluminum, and is presented in figure (5.1). In this figure, the normalized

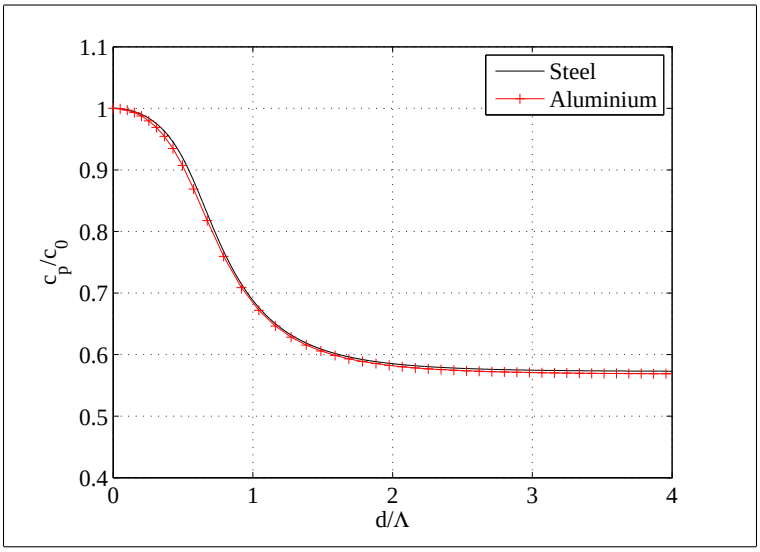

Figure 5.1: Normalized phase velocity as a function of d/Λ for steel ($\nu = 0.3$) and aluminum ($\nu = 0.34$); $M_{1,1}$ (After Bancroft [1])

phase velocity is plotted with respect to a/Λ, where a and Λ are the radius of the bar and the wavelength of the wave, respectively.

Davies [88] has presented the solution of the first three modes. He argues that the higher modes correspond to waves of extremely high frequencies and to forces applied over very small portions of the cross section of the bar. In this study, none of these conditions exists, and we only focus on the first mode of vibration, which is most likely the most dominant mode in our examples.

5.3 Wave Propagation in Layered Cylinders

For a cylinder with alternating layers of two materials, the dispersion relation of equation (5.18) must hold for each individual layer, so that the free-surface boundary conditions can be satisfied; therefore, each layer has its own dispersion relationship. Here, we take a similar approach that Rytov [81] employed to treat the problem of wave propagation in infinite layered media.

At the interface between every two layer, wave reflections occur due to impedance miss-match between the two different materials. As a result, we assume that in each layer, for a given frequency, waves propagate in both directions; thus, u_r and u_z in each layer can be written as:

$$u_r = \{-k_d A J_1(k_d r) + ik_0 k_t C J_1(k_t r)\} e^{i(\omega t - k_0 z)} \tag{5.19}$$
$$+\{-k_d B J_1(k_d r) + ik_0 k_t D J_1(k_t r)\} e^{i(\omega t + k_0 z)}$$
$$u_z = \{-ik_0 A J_0(k_d r) + k_t^2 C J_0(k_t r)\} e^{i(\omega t - k_0 z)} \tag{5.20}$$
$$+\{-ik_0 B J_0(k_d r) + k_t^2 D J_0(k_t r)\} e^{i(\omega t + k_0 z)}$$

Floquet's (or Block's) theory requires the harmonic quantities to have the same periodicity as the layered medium. In other words, the phase difference between two points, which are one unit cell apart, must be kL_u; where L_u is the unit cell length, and k is the layered medium wave number. We can hereby rewrite the equations (5.19) and (5.20) as:

$$u_r = \Big(\big\{ - k_d A J_1(k_d r) + ik_0 k_t C J_1(k_t r)\big\} e^{-i(k_0 + k)z} \tag{5.21}$$
$$+\big\{ - k_d B J_1(k_d r) + ik_0 k_t D J_1(k_t r)\big\} e^{-i(k - k_0)z}\Big) e^{i(\omega t + kz)}$$
$$u_z = \Big(\big\{ - ik_0 A J_0(k_d r) + k_t^2 C J_0(k_t r)\big\} e^{-i(k_0 + k)z} \tag{5.22}$$
$$+\big\{ - ik_0 B J_0(k_d r) + k_t^2 D J_0(k_t r)\big\} e^{-i(k - k_0)z}\Big) e^{i(\omega t + kz)}$$

where, k is the overall wave number associated with the Bloch wave.

The schematic view of a cylindrical bar consisting of two alternating materials is depicted in figure (5.2). Non-zero stresses and displacements in this problem must fulfill the Bloch periodicity conditions; *i.e.* the following equations must be

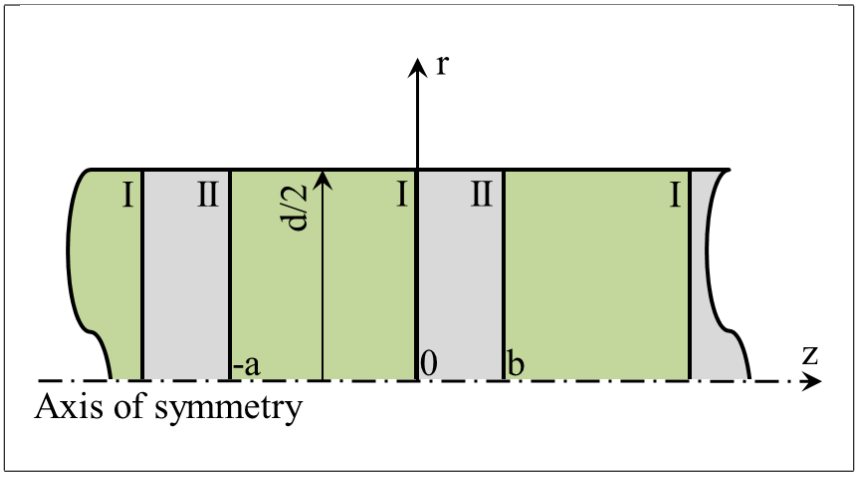

Figure 5.2: The schematic view of the layered cylindrical bar

satisfied:

$$u_r(r,0) = \bar{u}_r(r,0) \quad , \quad u_z(r,0) = \bar{u}_z(r,0) \tag{5.23}$$

$$\sigma_{zz}(r,0) = \bar{\sigma}_{zz}(r,0) \quad , \quad \sigma_{rz}(r,0) = \bar{\sigma}_{rz}(r,0) \tag{5.24}$$

$$u_r(r,-a) = \bar{u}_r(r,b)e^{ik(a+b)} \quad , \quad u_z(r,-a) = \bar{u}_z(r,b)e^{ik(a+b)} \tag{5.25}$$

$$\sigma_{zz}(r,-a) = \bar{\sigma}_{zz}(r,b)e^{ik(a+b)} \quad , \quad \sigma_{rz}(r,-a) = \bar{\sigma}_{rz}(r,b)e^{ik(a+b)} \tag{5.26}$$

where, a and b are the lengths of two adjacent layers constituting a unit cell, and all the unbarred and barred quantities correspond to materials I and II, respectively. Substituting equations (5.21) and (5.22) into the periodicity equations, yields a system of 8 equations and 8 unknowns. These equations are extremely difficult to solve; since r can not be simply eliminated from both sides. To arrive at the exact solution solution, a summation of infinite mode-shapes, each being a root of the Bessel functions, must be considered. Then, orthogonality condition between these modes should be used to calculate the unknowns. We, instead, use a first-order approximation of the Bessel functions which enables us to eliminate r from both sides, and simplify the problem.

In the solution for u_r and u_z, J_0 and J_1 are zeroth and first order Bessel functions of the first kind, and can be approximated by their Taylor series:

$$J_0(x) = 1 - \frac{1}{4}x^2 + \frac{1}{64}x^4 - ... \tag{5.27}$$

$$J_1(x) = \frac{1}{2}x - \frac{1}{16}x^3 + ... \tag{5.28}$$

Using the first-order approximation of Bessel functions and their derivatives to simplify u_r and u_z yields:

$$u_r = \left\{ (-A\frac{k_d^2}{2} + iC\frac{k_0 k_t^2}{2}) r e^{-i(k+k_0)z} + (-B\frac{k_d^2}{2} + iD\frac{k_0 k_t^2}{2}) r e^{-i(k-k_0)z} \right\} e^{i(\omega t + kz)} \tag{5.29}$$

$$u_z = \left\{ (-iAk_0 + Ck_t^2) e^{-i(k+k_0)z} + (-iBk_0 + Dk_t^2) e^{-i(k-k_0)z} \right\} e^{i(\omega t + kz)} \tag{5.30}$$

The non-zero stresses at the interface between each two layer are:

$$\sigma_{zz} = \lambda \left\{ \frac{u_r}{r} + \frac{\partial u_r}{\partial r} + \frac{\partial u_z}{\partial z} \right\} + 2\mu \frac{\partial u_z}{\partial z} \tag{5.31}$$

$$\sigma_{zr} = \mu \left\{ \frac{\partial u_r}{\partial z} + \frac{\partial u_z}{\partial r} \right\} \tag{5.32}$$

Finally, we substitute u_r and u_z into equations (5.31) and (5.32) to arrive at:

$$\begin{aligned} \sigma_{zr} &= \big(\mu\{iA(k_0 k_d^2/2) r e^{-ik_0 z} + iB(-k_0 k_d^2/2) r e^{ik_0 z} + \\ &\quad + C(k_0^2 k_t^2/2) r e^{-ik_0 z} + D(-k_0^2 k_t^2/2) r e^{ik_0 z}\}\big) e^{i\omega t} \end{aligned} \tag{5.33}$$

$$\begin{aligned} \sigma_{zz} &= \big(A(-(\lambda+2\mu)k_0^2 - \lambda k_d^2) e^{-ik_0 z} + B((\lambda+2\mu)k_0^2 - \lambda k_d^2) e^{ik_0 z} + \\ &\quad + iC(2\mu k_0 k_t^2) e^{-ik_0 z} + iD(2(\lambda+\mu) k_0 k_t^2) r e^{ik_0 z}\big) e^{i\omega t} \end{aligned} \tag{5.34}$$

Substituting equations (5.29) - (5.34) into the periodicity equations results in a homogeneous system of 8 equations and 8 unknowns, all independent of r. Non-trivial solutions to this system can only exist when the determinant of the

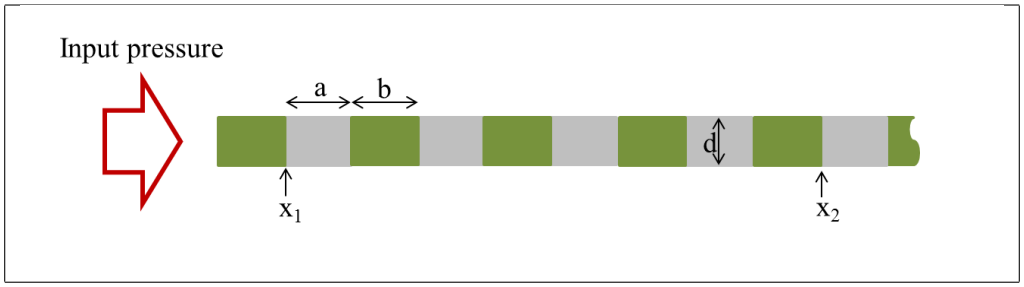

Figure 5.3: The schematic view of the geometry of the FEM model

corresponding matrix is equal to zero. The numerical solution to this problem is presented and discussed in section (5.5).

5.4 Steel-Aluminum Example (FEM vs. Analytical)

In this section, we consider the propagation of elastic waves in a long and relatively thin cylindrical bar consisting of alternating layers of steel and aluminum. Finite Element Method (FEM) is employed to investigate the accuracy and validity of the approximate method of solving the wave propagation problem in layered cylindrical bars, as presented in section (5.3). To this end, we applied our approximate method to a specific example and compared the results to those calculated from the Finite Element method. The procedure is summarized below:

- A finite element model was generated consisting of a number of alternating steel and aluminum cylinders.
- A pressure pulse was defined to be the input to the FEM model.
- The input pulse was applied as pressure to one end of the FEM model, and

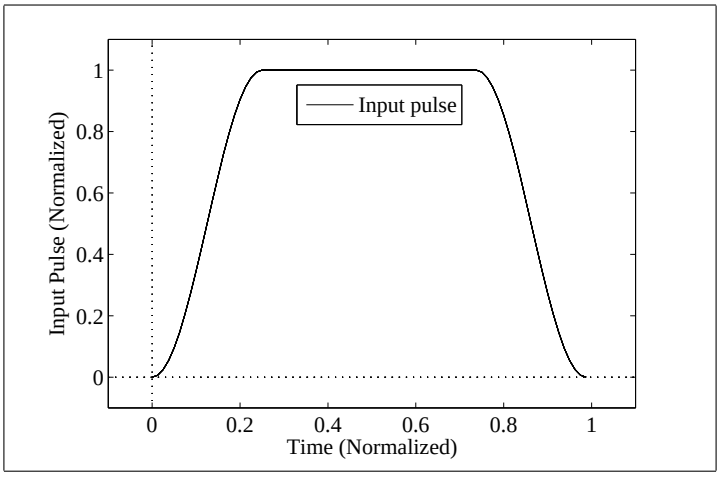

Figure 5.4: Input pressure pulse to the FEM model.

the propagation of this pulse through the layered material was solved using an explicit FEM software package.

- The system of equations from the periodicity conditions was solved to calculate the corresponding dispersion relationship for this layered medium.

- A dispersion correction routine was written in Matlab. The input to this routine is the shape of a pulse in time at any given point on the bar. Given the pulse and the dispersion curve of the medium, this routine is capable of obtaining the shape of the pulse at any given point on the bar.

- The results from the FEM model and the dispersion correction routine were compared and discussed.

5.4.1 Finite element model

An axi-symmetric finite element model was developed to solve the wave propagation problem in a layered cylindrical bar with known material properties.

A Matlab routine was written to generate the FEM model suitable for explicit calculations in LS-DYNA, a commercially available FEM solver. Input parameters to this routine were material properties of each layer, geometry and the size of the elements. Elastic material constants used for these simulations are:

$$E_{steel} = 210GPa \quad , \quad E_{Al} = 70GPa \tag{5.35}$$

$$\rho_{steel} = 7800Kg/m^3 \quad , \quad \rho_{Al} = 2700Kg/m^3 \tag{5.36}$$

$$\nu_{steel} = 0.3 \quad , \quad \nu_{Al} = 0.34 \tag{5.37}$$

Figure (5.3) illustrates the geometry of the finite element model. The following list contains the geometrical details of this model:

- Total length of the bar = 300cm
- Diameter of the bar = 3cm ($d/2 = 1.5$)
- Steel layer thickness = 8cm ($a = 8$)
- Aluminum layer thickness = 8cm ($b = 8$)

No external boundary conditions were applied to this model. A pre-defined pressure pulse was exerted to the left side of this model to generate a pressure wave. The propagation of this pressure pulse in the z-direction was solved and analyzed. Figure (5.4) presents the pressure pulse applied to the finite element model. The total time duration of this pulse is $100\mu s$.

Figure (5.5) presents the results from finite element analysis. In this figure, the pressure pulse at locations $x_1 = 40cm$ and $x_2 = 200cm$ is plotted as a function of time. Note that only one pulse is traveling in the bar; but, for illustration purposes, it is plotted in the same figure. For the sake of comparison, the same pressure pulse is applied to a steel-only cylindrical bar, and similarly, the pressure

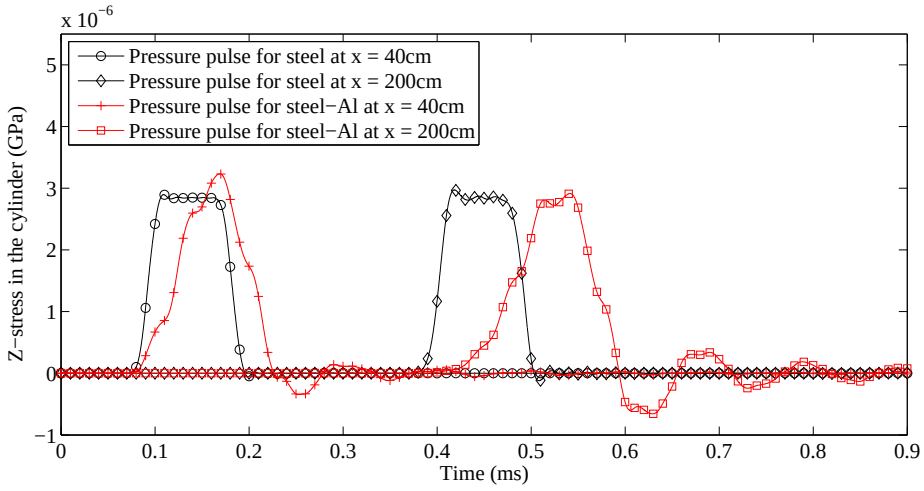

Figure 5.5: Time-history of the pressure pulse at different points in the elastic bar. Note how the shape of the pulse changes as the wave travels further down the bar. Also, the pulse shape-changes for the steel-only and the layered steel-Al bars are noticeably different.

pulse is plotted at the same locations: x_1 and x_2. There is a substantial difference between the propagation of the same wave in the two cases. It can be seen that the shape of the pulse changes due to dispersion as it travels from x_1 to x_2. The next section deals with the calculation of this dispersive effect and the prediction of the shape of a pulse as it travels in the composite.

5.4.2 Dispersion correction

Figure (5.5) illustrates how the shape of a pulse deforms while propagating in a dispersive medium. Dispersion in a medium occurs due to the fact that waves with different frequencies travel at different velocities. The knowledge of the dispersive properties of the medium can assist in estimating the changes in the shape of a propagating pulse.

Any given pulse can be represented as an infinite sum of harmonic waves of

different frequencies. In an elastic cylindrical bar, the propagation velocity of these waves are different. Consequently, starting from the same point, they arrive at any given location down the bar at different times. This means that in the summation, each frequency has a different phase shift. These shifts can be computed from the dispersion curve for any given frequency. As a result, by having the shape of a wave at one point in a solid bar, the shape of the wave can be obtained by this shifting process at any given point. This process is known as *dispersion correction.*

A dispersion correction routine is developed as a Matlab function. The procedure is straightforward; for a given pulse, $\mathbf{v}$, and a distance x_0:

- The Fast Fourier Transform (FFT) of the pulse is calculated: $\mathbf{v}_f = \text{fft}(\mathbf{v})$.
- For each frequency, the phase is corrected: For the j^{th} element of the vector in Fourier space,

$$\mathbf{v_f}^j = a_j + ib_j \Longrightarrow \phi_j = tan^{-1}(b_j/a_j) \tag{5.38}$$

the frequency associated with the j^{th} element of $\mathbf{v}_f$ is

$$p = \frac{2\pi}{T_{span}}(j-1)$$

where, T_{span} is the duration of the pulse. The characteristic equation of (5.18) can be solved to obtain the wave number (k) corresponding to this frequency. In figure (5.6), the wave number as a function of frequency is plotted for steel and aluminum for a cylinder of diameter $3cm$. The phase (angle) of the j^{th} element of $\mathbf{v}_f$ at a distance x_0 is evaluated,

$$\phi_j^{new} = \phi_j + kx_0$$

and finally, the real and imaginary parts of $\mathbf{v}_f$ are updated such that the magnitude remains intact:

$$\mathbf{v}_f^j = \sqrt{a^2+b^2}\ e^{i\phi_j^{new}} \tag{5.39}$$

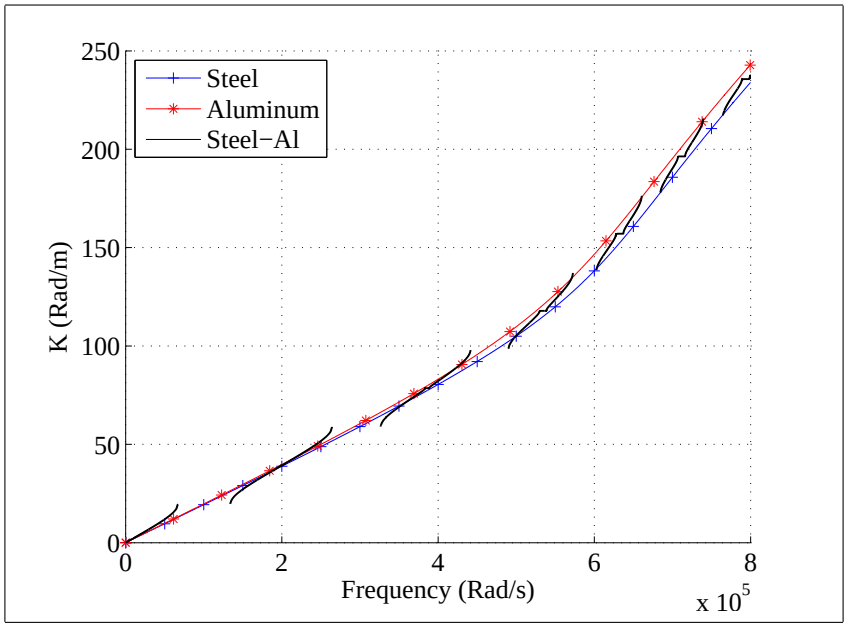

Figure 5.6: $k-\omega$ relationship for: (1) a steel-only bar, (2) an aluminum-only bar, (3) a layered steel-aluminum cylindrical bar. The numerical method to obtain the black solid line related to case (3) is explained in section (5.5).

- An Inverse Fast Fourier Transform (IFFT) is performed on the updated $\mathbf{v}_f$ to arrive at the pulse shape at the desired distance (x_0) from the original location.

To verify the accuracy of this routine, the propagation of the pressure pulse of figure (5.4) in a steel cylinder is considered. First, this problem is solved by the FEM model and the shape of the pulse at locations $x_1 = 40cm$ and $x_2 = 200cm$ are obtained. Then, the pressure pulse at x_1 is used as input to the dispersion correction routine and the deformed pulse at x_2 is calculated. Figure (5.7) illustrates the results, which indicates a near perfect match between the finite element method and the dispersion correction results.

The analytical solution to the wave propagation problem for elastic cylinders is remarkably accurate over a broad range of frequencies and loading condi-

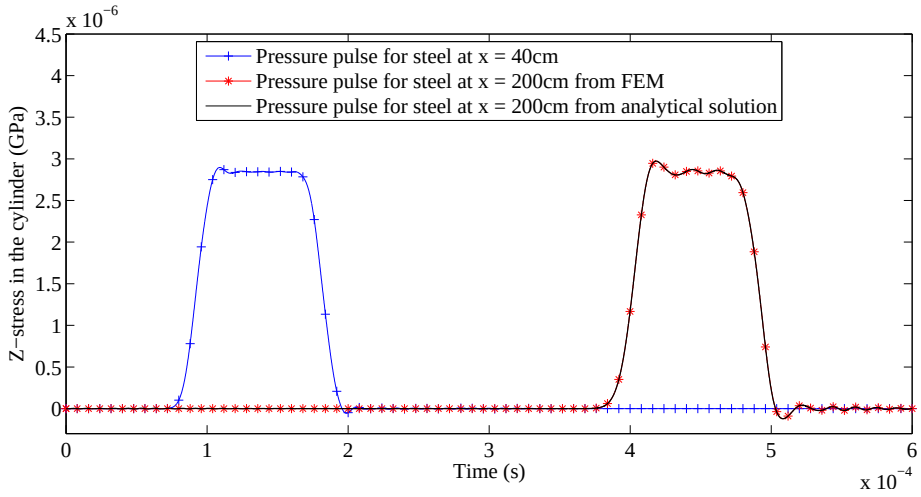

Figure 5.7: The pressure pulse for the steel-only bar is plotted at two different points in time: (1) from FEM results, (2) from the analytical solution: Using the dispersion relationship, the pressure pulse at $x = 200cm$ is numerically obtained from the time-history of the pulse at location $x = 40cm$.

tions. This has been observed and experimentally approved by many researchers (*reference needed*). In fact, the dispersion correction routine has been used over years in many applications, such as in Split Hopkinson Pressure Bar (SHPB) experiments. Inspired by this method of verifying the analytical solution, we seek to correct the dispersion occurring in a periodic layered cylinder using our numerical calculation of the corresponding dispersion curve. Next section presents the numerical method employed to obtain the dispersion curve for a layered cylindrical medium.

5.5 Dispersion Curve for Layered Cylinders

In this section, a method to numerically obtain the dispersion curve for layered cylinders is given: for given material properties and geometry, the dispersion curve for each layer was calculated; *i.e.* the value of wave number was numerically

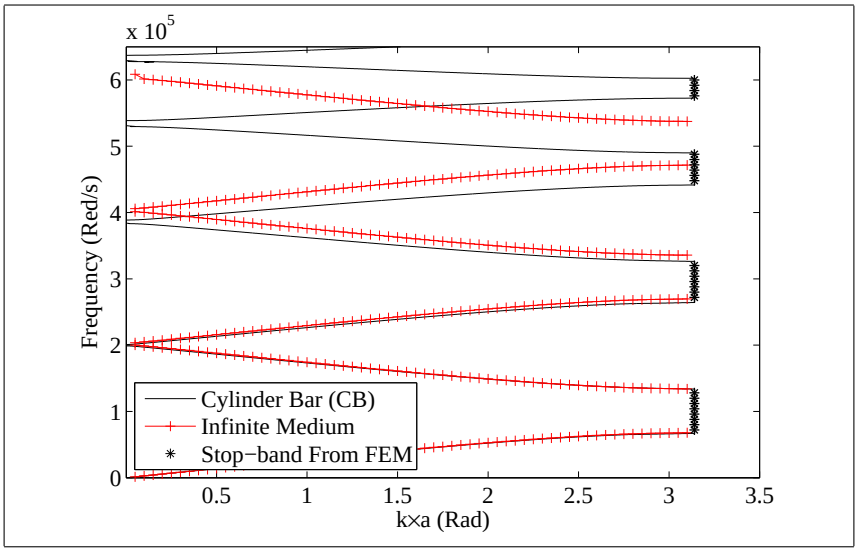

Figure 5.8: Dispersion curve for the layered steel-aluminum medium: (1) for a cylindrical bar, (2) for an infinite medium. Also, the stop-band frequencies for a specific problem is obtained from FEM results (section 5.5.1), and is compared to case (1).

calculated as a function of frequency for each material (Bancroft's approach - Figure 5.6). The system of 8-equations 8-unknowns, obtained in section (5.3), was formulated in matrix form. The elements of this matrix are functions of k_1, k_2 and material properties of steel and aluminum. A non-trivial solution can only exist when the determinant of this matrix becomes zero. For a given frequency, the determinant of this matrix is a function of $k \times a$, where a is the length of the unit cell. An optimization routine was designed, and a Matlab script was written to find the root of this function for any given frequency. The dispersion curve can then be obtained by running this script over a range of frequencies.

The black solid line in figure (5.8) corresponds to the dispersion curve for the steel-aluminum layered cylinder of the proposed example. The dispersion curve for an infinite layered medium for the same material properties is also plotted (red solid line with plus markers). The frequencies for which $k \times a = \pi$, correspond

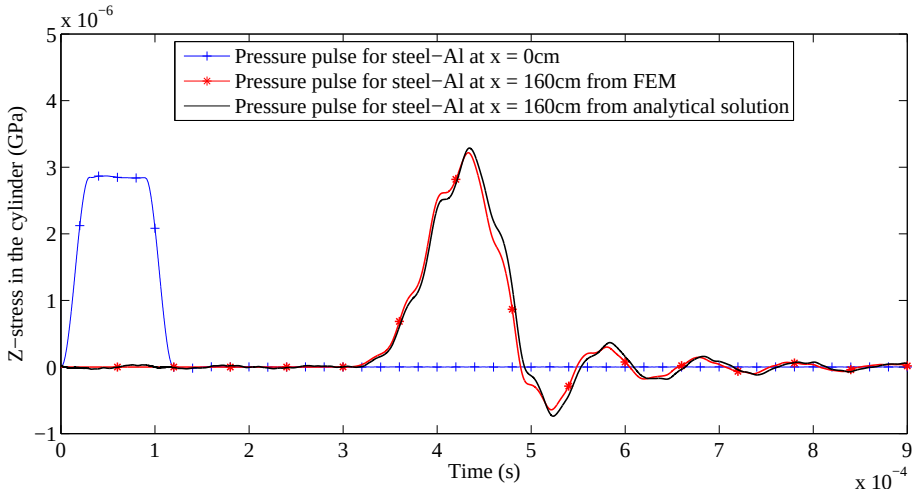

Figure 5.9: The pressure pulse for the layered steel-Al bar is plotted at two different points in time: (1) from FEM results, (2) from the approximate analytical-numerical solution: Using the dispersion relationship for the layered cylinder, the pressure pulse at $x = 160cm$ is obtained from the time-history of the pulse at location $x = 0cm$.

to stop-bands. At those frequencies, the traveling wave experiences a phase shift of $(2n-1)\pi$ through one unit cell, where n is the number of stop-band (starting from 1 for the first stop-band and increasing to ∞). At the interface between the unit cells, part of the wave is reflected with an additional π phase shift. When the reflected pulse reaches the other side of the unit cell, it is out of phase with coming waves of that frequency. As a result, the refracted and reflected waves at this frequency cancel each other out, and the wave is trapped inside the first few layers.

To apply the dispersion correction method explained in section (6.4) to the layered cylinder problem, a function is needed to relate each frequency to a wave number. The dispersion curve of figure (5.8) can be used to extract that function. Note that the value of k is needed to find the phase shift of the pulse at a given distance. Dividing the values in figure (5.8) by a would not result in proper values

of k. The correct wave number can be obtained by,

$$k_c = \frac{(-1)^{m+1}\{k \times a(\text{from figure } 5.8)\} + m\pi}{a}$$

where, m and a are the branch number and the unit cell length, respectively. The black solid line in figure (5.6) shows k versus frequency for the steel-aluminum layered cylinder, which remarkably lies between k_1 and k_2 corresponding to the steel and aluminum bars, respectively.

In figure (5.9), the result of dispersion correction for the steel-aluminum layered cylinder is presented and compared to the finite element results. The pressure pulse at $x_1 = 0$ was the input to the Matlab code (blue line with plus markers) and the shape of the pulse at $x_2 = 160cm$ was calculated (black solid line). The red line with star markers corresponds to the solution of the finite element model for this problem at $x_2 = 160cm$. The figure exhibits a good match between the pulses calculated from FEM method and the proposed analytical/numerical method. This plot clearly ascertains the validity of the presented approach to approximate the propagation of the elastic waves in elastic cylinders. It is expected that for higher frequencies when the first order Taylor Series approximation of the Bessel functions is not adequate to represent the mode shapes of the cylinders, the results of the proposed method may diverge from actual results. At those frequencies, evaluating the accuracy of this method requires further investigation.

5.5.1 Solution for a pulse containing high-frequency content

A simple Fourier analysis of the input pulse of the example presented in the previous section reveals that the high frequency content (above the first stop-band) is relatively insignificant. In this section, we investigate the accuracy and validity

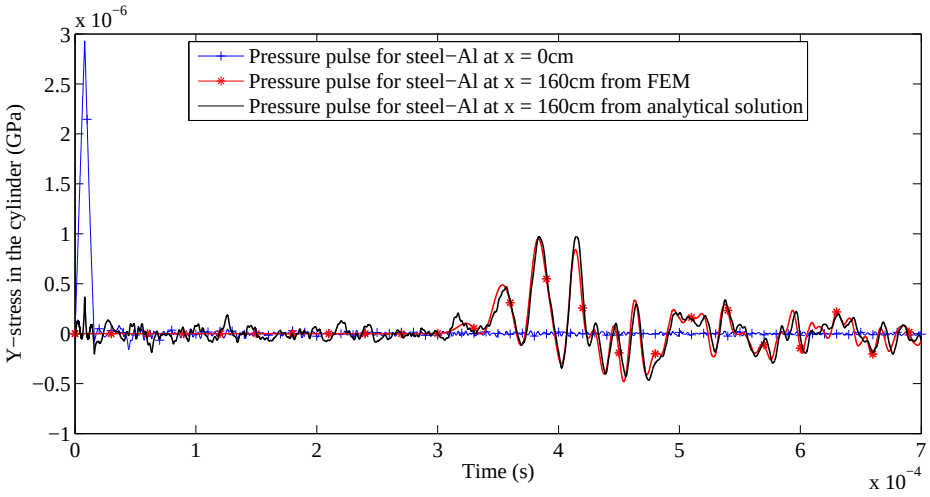

Figure 5.10: The pressure pulse of section (5.5.1) is plotted for the layered steel-Al bar at two different points in time: (1) from FEM results, (2) from the approximate analytical-numerical solution: Using the dispersion relationship for the layered cylinder, the pressure pulse at $x = 160cm$ is obtained from the time-history of the pulse at location $x = 0cm$.

of our proposed solution for layered cylinders at higher frequencies. Subsequently, a very short pulse containing high frequencies was applied to the same problem; followed by the same comparison approach used in previous section: First, the propagation of this pulse was solved by FEM and the shape of the pulse at $x_2 = 160cm$ was recorded. Then, the dispersion correction procedure was employed to obtain the shape of the pulse at the same location (x_2). Figure (5.10) illustrates the results. Again, a very good match between the the proposed dispersion correction method and finite element results is achieved.

FEM results are employed to verify the accuracy of the proposed approximate method in finding the stop-bands. Figure (5.11) depicts the Fourier Transform's of: (1) the sharp input pulse at $x_1 = 0cm$, blue line with plus markers; (2) the pulse that traveled along the bar to reach the location $x_2 = 160cm$ from the FEM results, red line with star markers. It is clear from the figure that some of the

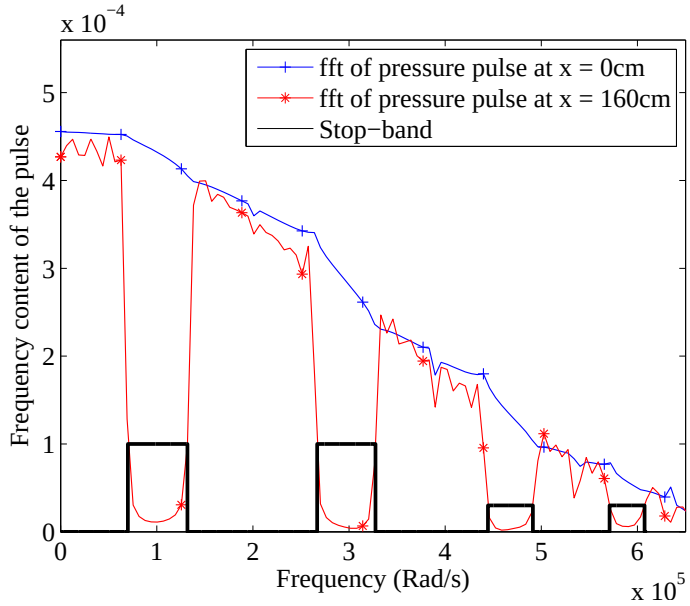

Figure 5.11: The frequency content of the pressure pulse of section (5.5.1) from FEM results: (1) at location $x = 0cm$ (2) down the bar at location $x = 160cm$. It is clear that some frequencies are filtered when the wave travels along the cylindrical bar. The solid black line is our estimate of the stop-bands for this example.

frequencies are filtered. The first four stop-bands are approximated by the solid black line. These frequencies are plotted as black stars in figure (5.8). Remarkably, the approximate solution of the wave propagation problem for layered cylinders yields very accurate results in finding the stop-bands.

5.6 Summary and Conclusion

An analytical-numerical method to approximate the solution of wave propagation problem in periodic layered cylindrical bars was presented. This method was then employed to obtain the dispersion curve for a periodic steel-aluminum cylinder. A dispersion correction routine was developed to obtain the shape of a given pulse at any given location on the periodic bar.

To verify the accuracy and validity of this approach, a numerical example was designed with a pre-defined pressure pulse as the input. A finite element model of the example was developed, suitable for explicit calculations in LS-DYNA. The propagation of the applied pressure pulse was first solved by FEM. Then, the problem was solved by the proposed dispersion correction routine and the results were compared to FEM calculations.

The results exhibit a good match between the two methods of solving the wave propagation problem in layered cylinders. It was also shown that the proposed analytical-numerical method was capable of measuring the pass-bands accurately.

5.7 Acknowledgments

The author would like to acknowledge Dr. Ankit Srivastava for his precious comments, and also for providing the dispersion curve for the infinite layered media

in figure (5.8). This work is prepared for publication by A. Samiee, A. Srivastava and S. Nemat-Nasser. The author of this dissertation is the main investigator of this work.

Chapter 6

High Strain Rate Behavior of Concrete Under Compression and Tension

Unconfined compression and tension tests have been performed on cylindrical samples prepared from a newly developed concrete. A 3-inch Split Hopkinson Pressure Bar (SHPB) setup has been employed to experimentally obtain the stress-strain relation of the concrete at different strain rates. A novel procedure is introduced to conduct tension tests. Initiation and propagation of cracks in concrete samples are captured by high-speed photography. The experimental data will be used to improve the existing concrete material models.

Extracting stress-strain relations from the experimentally obtained SHPB data requires assumptions about the sample size and the friction between the sample and the bars. The effect of violating these assumptions on the validity of experimentally acquired stress-strain results is explored by performing a full-scale finite element simulation of the entire process. Numerical results reveal that in

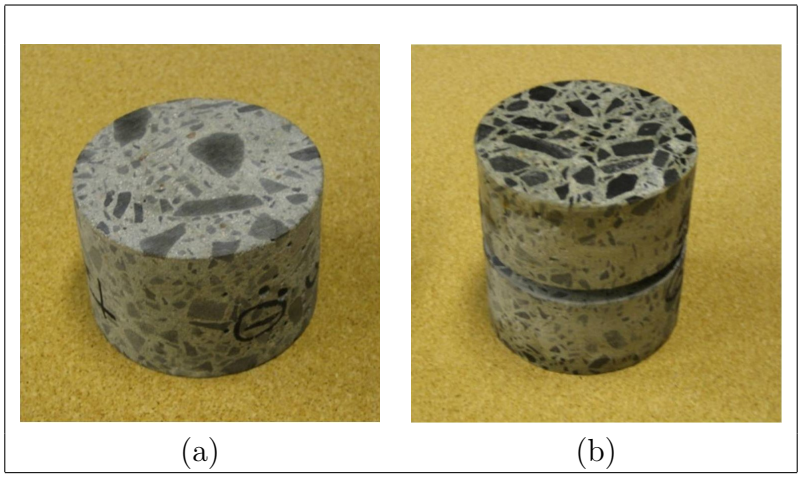

Figure 6.1: (a) Compression test specimen: 75 mm in diameter, 50 mm in length (b) Tension test specimen: 75 mm in diameter, 89 mm in length - A 6.35 mm wide notch with diameter 57.2 mm is designed to force the fracture to occur in the middle.

the presence of friction, the strain and stress history are not uniform within the sample. The usual method of analyzing the Hopkinson bar experimental results that generally overlooks this fact can be corrected by minor calibration on the data.

6.1 Compression Tests

In this section, we report the experimental results of our unconfined tests on concrete in compression subjected to high strain rate loadings. A Split Hopkinson Pressure Bar (SHPB) setup has been employed for the experiments. A compression sample is illustrated in figure (6.1a), which is nominally 75mm in diameter and 50mm in length. In Hopkinson bar experiments, the samples are usually small and thin. In our experiments, however, the size of aggregate was the leading factor in designing the samples, and the dimensions had to be chosen large enough to reduce

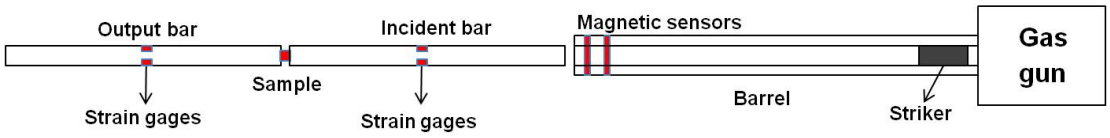

Figure 6.2: Split Hopkinson Pressure Bar (SHPB) setup for compression tests

the local effects. In other words, a small sample would result in material properties corresponding to aggregate or cement only. The effect of large sample size on the accuracy and validity of the experimental results is investigated numerically in section (6.3).

The primary objective of these experiments was to obtain a relationship between the strain rate and the stiffness of the samples. For that, the stress-strain results are presented in section (6.1.3).

6.1.1 Compression experimental setup

A Split Hopkinson Pressure Bar (SHPB) is employed to conduct experiments on concrete in compression. Pioneered by Hopkinson (1872) and fundamentally modified to its current form by Kolskey (1949), SHPB has been extensively used to study the high strain rate properties of materials.

In figure (6.2), a SHPB setup is schematically illustrated. A sample is sandwiched between two relatively long cylindrical bars known as incident and transmission bars. A gas gun is used to accelerate a striker towards the incident bar. The striker is usually impedance-matched with the bars. The impact of the striker with the incident bar generates a longitudinal pressure wave, which travels along the bars. When this wave reaches the sample, part of it is reflected, and the remaining part is transmitted. This is the result of the impedance mis-match between the

Figure 6.3: Experimental setup - 3" Split Hopkinson Pressure Bar in the high strain rate lab at UCSD's CEAM

bars and the sample. The time-histories of the initial, reflected and transmitted waves are measured by strain gages surface-mounted at the mid-length of each bar. Typical raw data from the gages on the incident and transmission bars is plotted in figure (6.4). This data can be used to calculate the true stress and strain experienced by the sample. The corresponding equations, which are derived from one dimensional wave propagation solution, are written as (see Nemat-Nasser *et. al.* (1991) and Gray (1999)):

$$\frac{d\varepsilon_s(t)}{dt} = -\frac{2c_0}{L_s}\varepsilon_R(t) \tag{6.1}$$

$$\varepsilon_s(t) = \int_0^t \dot{\varepsilon}_s(t)dt \tag{6.2}$$

$$\sigma_s(t) = E_0\frac{A_0}{A_s}\varepsilon_T(t) \tag{6.3}$$

where, ε_s and σ_s are the true strain and stress in the sample, respectively; ε_R and ε_T are the strains on the bars corresponding to the reflected and transmitted waves,

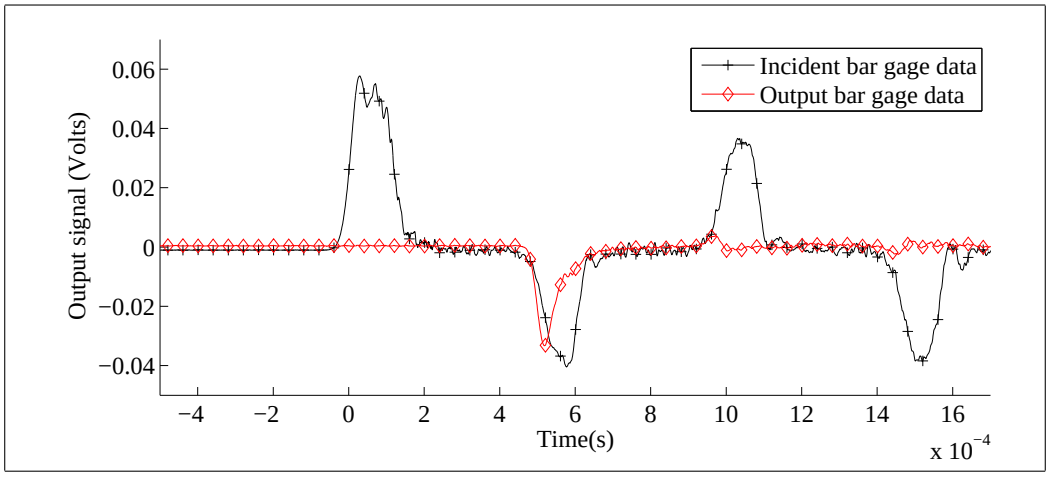

Figure 6.4: Typical raw data from the gages on the incident and transmission bars

respectively; L_s, A_s, A_0, E_0 and c_0 are the length of the sample, cross-sectional area of the sample, cross-sectional area of the bars, modulus of elasticity of the bars and the longitudinal wave velocity in the bars, respectively. We refer to equations (6.1-6.3) as the *Hopkinson bar equations*.

A few remarks on the accuracy and validity of the Hopkinson bar equations, which are derived under certain assumptions:

- The striker, incident and transmission bars must remain elastic. In these experiments, the bars are made of a high strength aluminum alloy. The highest stresses occurring in the concrete samples are far from exceeding the elastic limit of this aluminum.

- These equations are derived assuming that the sample deforms uniformly; *i.e.* the forces acting on the two sides of the sample are assumed to be equal at all times.

- The strain-histories measured at the gages are not identical to strains at the interfaces of the sample and the bars, due to the *dispersion* of waves in

elastic cylindrical bars.

- The friction at the interfaces of the sample and the bars is neglected.

A popular approximation for the time needed to reach the state of equilibrium is the time required for π-reverberations of the wave within the sample [90]. Therefore, thin samples are usually more appropriate for a SHPB experiment. For brittle materials, a common approach is to employ a ramp-shape pulse, which can be obtained by placing a thin circular piece of a ductile material, for instance copper, between the striker and the incident bar. Consequently, the brittle sample would have enough time to reach the equilibrium state before fracture. The brittle material most likely fails (fractures) during the rise time of the pulse. The strain rate also increases during the course of deformation, and does not remain constant. Therefore, unlike ductile materials, it is very unlikely to achieve a constant strain rate during the deformation for brittle materials. In other words, assigning a strain rate to the results from a Hopkinson bar experiment on a brittle material is not acceptable. Further explanation on the strain rate issue is presented in section (6.1.2).

The exact analytical solution of the propagation of longitudinal waves in cylindrical elastic bars (Pochhammer (1876), Chree (1889), and Bancroft [91]) indicates that waves with different frequencies travel with different velocities. More specifically, waves with higher frequencies tend to propagate slower in the bar. This gives rise to a pulse shape-change which we refer to as *dispersion*. When a pulse containing waves with different frequencies travels along a bar, it preserves all the waves; however, the waves are phase-shifted relative to one another. These phase shifts can be calculated for different frequencies, and a dispersion correction routine can be developed to evaluate the shape of the pulse at any given location on the

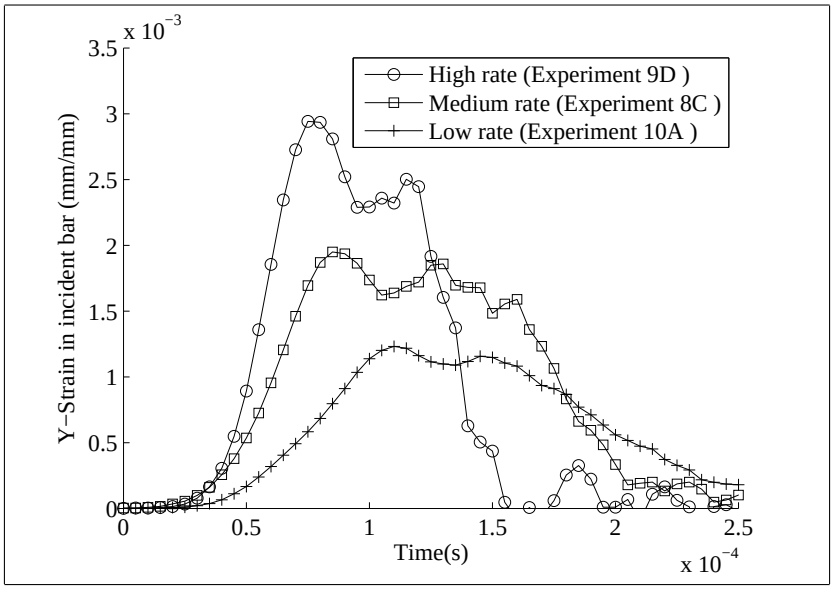

Figure 6.5: Compression waves generated by strikers with various sizes and impact velocities to produce different strain-rates; recorded from the gages on the incident bar.

bar. For out experiments, all the measured waves at the gages were dispersion corrected to obtain the exact strain history as arrived at the interfaces. A detailed explanation of this process in presented in section (6.4).

6.1.2 Input pulses and strain rates

The strain-history at the mid-length of the incident and transmission bars are measured by the gages. As discussed before, achieving constant deformation rates in brittle samples seems unlikely. Therefore, instead of assigning a value of strain rate to each experiment, we differentiate them as *high, medium and low rates*. To obtain different deformation rates, the length and the impact velocity of the striker were varied. Figure (6.5) displays the three input pressure pulses generated for our compression tests.

The reflected pulses from the sample, and measured at the gages on the

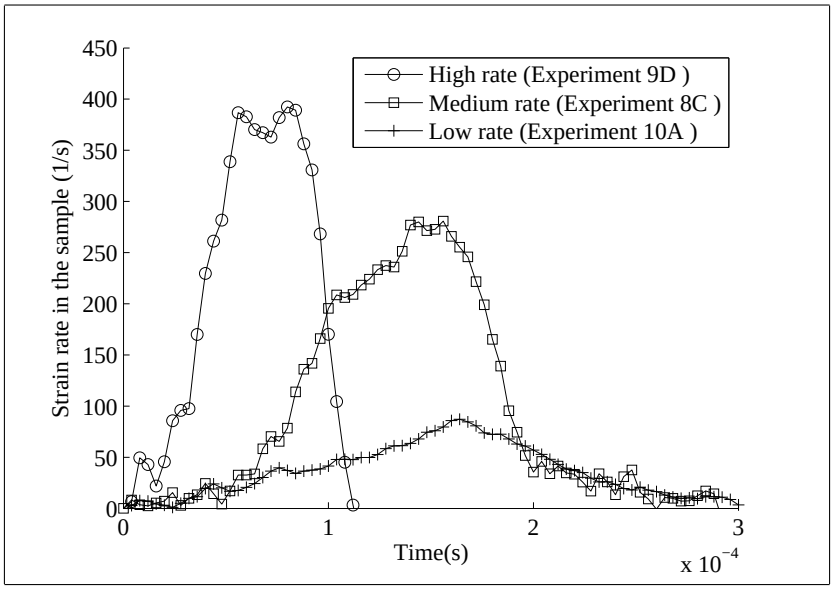

Figure 6.6: Time-histories of strain rate for three experiments in compression tests. Note that the strain rate is not constant during the course of deformation.

incident pulse, are dispersion corrected, and equation (6.1) is employed to calculate the strain rate history of the sample. In figure (6.6), the time-histories of the strain rate for three experiments are illustrated. Note that the strain rate is not constant during the course of deformation; however, to be able to quantitatively analyze the response of concrete to high rate loadings, we define a metric as an indication of deformation rate for each experiment. This metric is defined as the strain rate at the time of failure. Figure (6.7) demonstrates how the metric is assigned to the experiments: first, the time at which the maximum stress (from equation (6.3)) occurs in the sample is determined. Then, the strain rate at that time is measured from equation (6.1), and is assigned to the corresponding experiment.

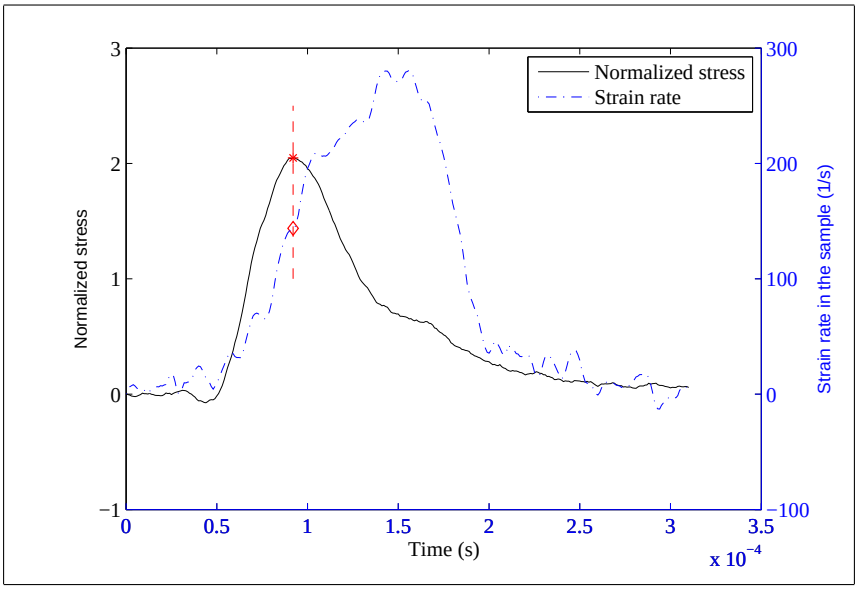

Figure 6.7: The strain rate at the time of failure is assigned to each experiment as a metric of deformation rate in the sample.

6.1.3 Experimental results

The compression samples were fragmented into pieces after the experiments (figure 6.8a). High-speed photography reveals that the initial cracks propagate along the planes parallel to the wave propagation in compression samples.

Equations (6.1)-(6.3) are employed to calculate the strain- and stress-histories for all the samples. In figure (6.9), the stress-strain relationships for all the compression samples are plotted. The highest stresses are designated by red circles. The stress is normalized by the quasi-static failure stress of the same concrete. Note that three separate groups of data, each corresponding to a rate level, can be identified.

In figure (6.10), the normalized failure stresses of the tested samples are plotted versus the strain rates at the times of fracture. These results suggest that a correlation exists between the rate of loading and the maximum stress in the

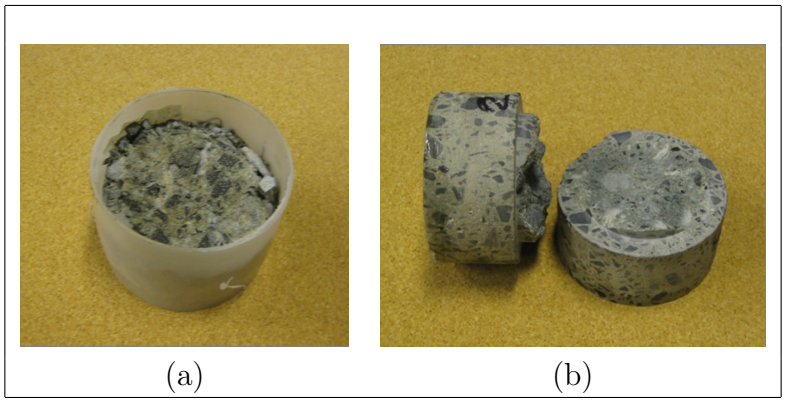

Figure 6.8: (a) A compression sample after the experiment (b) A tension sample after the experiment

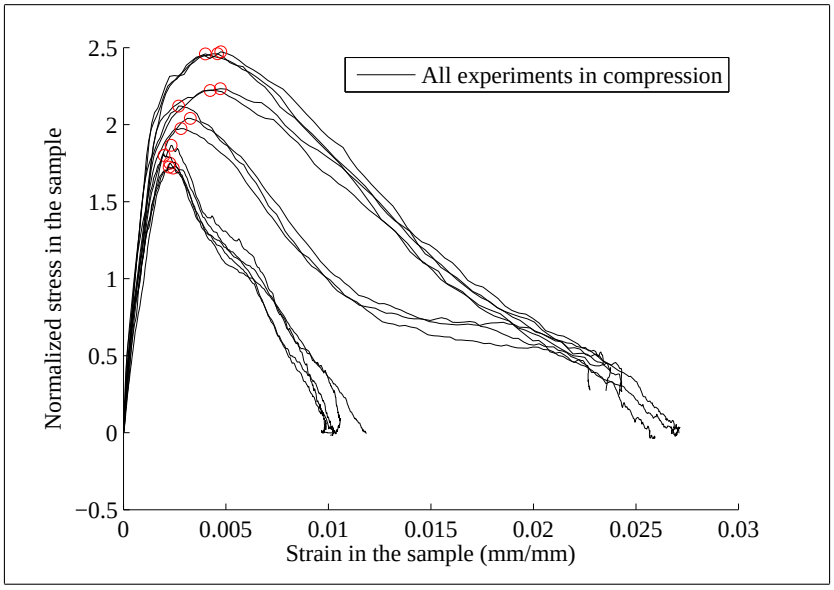

Figure 6.9: Compression test results: normalized stress vs. strain

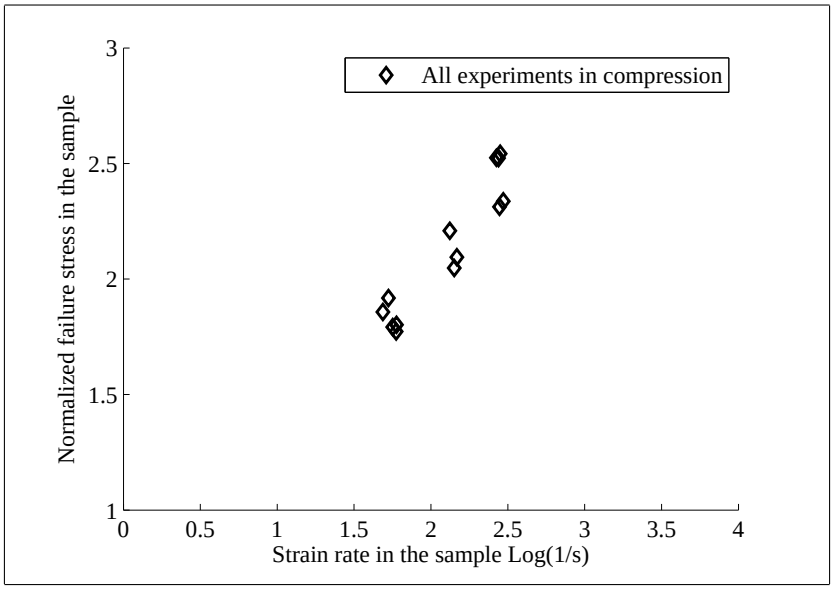

Figure 6.10: Concrete strengthening with rate in compression: Normalized stress vs. strain rate

sample before the fracture.

The slopes of the stress-strain curves in figure (6.9) are calculated to investigate the effect of the rate of loading on the elastic modulus of this concrete. In figure (6.11), the elastic moduli for all the compression tests are plotted versus the strain rates at the times of failure; no definitive correlation can be observed.

6.2 Tension Tests

In this section, the results of the tension experiments on concrete subjected to high strain rate loadings are presented. A modified Split Hopkinson Pressure Bar (SHPB) setup has been employed for the experiments. A tension sample is illustrated in figure (6.1b), which is 75 mm in diameter and 89 mm in length. The sample is glued between two bars, and pulled to fracture. A 6.35 mm wide notch with diameter 57.2 mm is designed to force the fracture to occur in the middle,

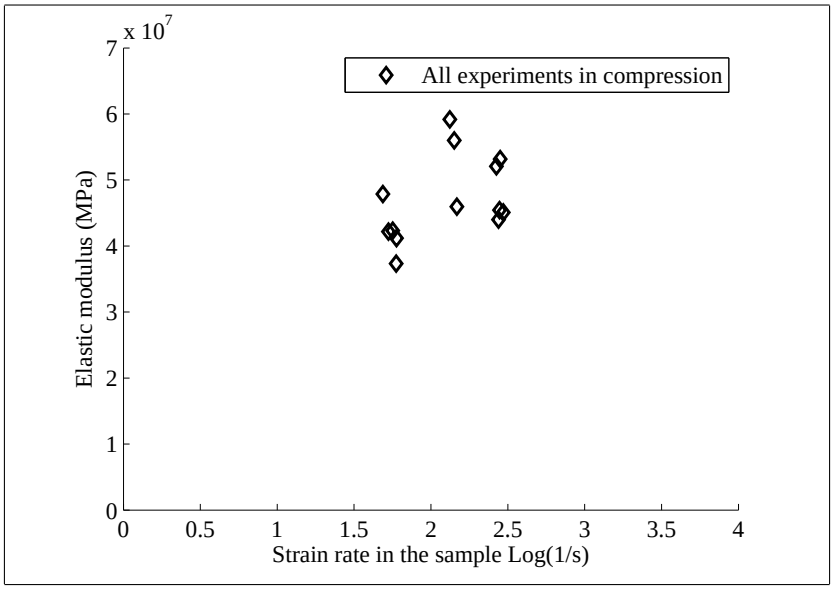

Figure 6.11: Elastic modulus in compression

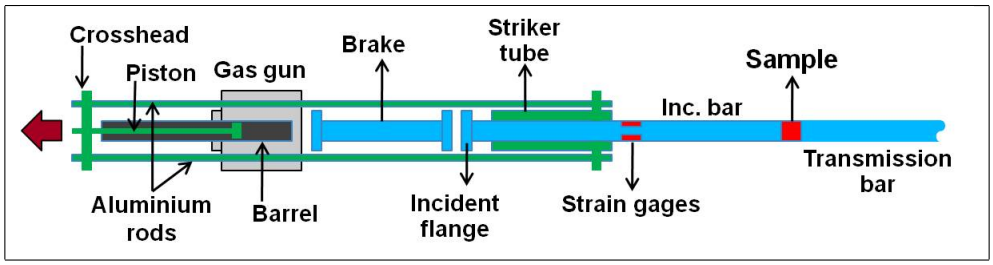

Figure 6.12: Split Hopkinson Pressure Bar (SHPB) setup for tension tests

i.e. at the cross-section of the notch rather than the glue line. The presence of the notch precludes application of equation (6.1) in accurately measuring the rate of strain in the samples. Nevertheless, this equation can be used to approximate the rate of deformation of the sample. On the other hand, equation (6.3) remains applicable for measuring the stress in the samples.

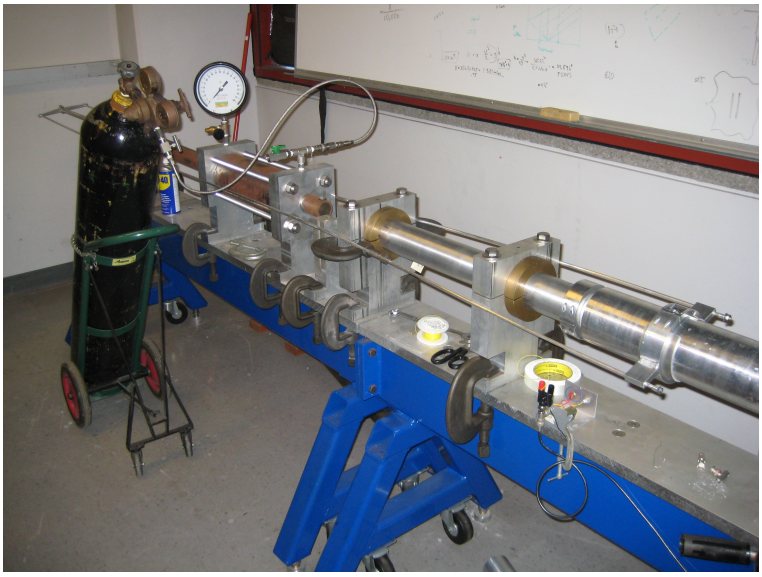

Figure 6.13: The tension Hopkinson bar setup at the high strain rate lab at UCSD's CEAM

6.2.1 Tension experimental setup

A novel method was proposed and developed by Mr. Jon Isaacs to carry out the tension experiments on concrete. Figure (6.12) illustrates the schematic view of the tension experimental setup. A tension sample (figure 6.1b) is glued between the incident and transmission bars using a special epoxy glue. The sample is slightly compressed for one-and-a-half hour, until the glue is fully cured. A striker tube is mounted on the incident bar. The tube is bolted to two aluminum bars, which are attached to a cross-head on their other end. The cross-head is placed in front of the barrel of a gas gun. A piston is employed to push the cross-head away from the barrel, causing the aluminum bars to accelerate the striker tube towards a flange, which is bolted to the incident bar. The impact of the striker tube with the flange generates a tension pulse in the incident bar. A braking system is installed to stop the incident bar after the impact. The tension experimental setup is displayed in

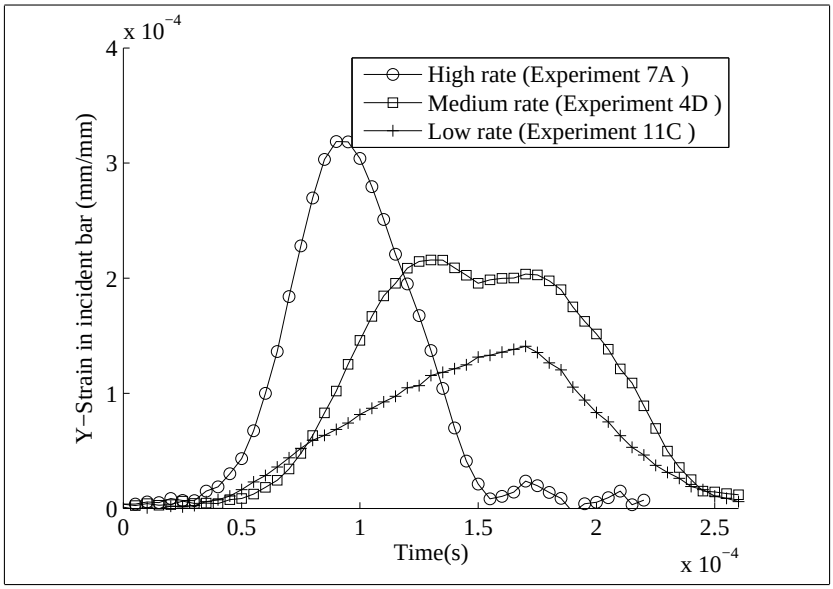

Figure 6.14: Tension waves generated by strikers having various sizes and impact velocities to produce different strain-rates; Recorded from the gages on the incident bar.

figure (6.13).

Upon the arrival of the tension pulse to the sample, part of the pulse is reflected, and the remaining is transmitted through the sample to the output bar. Note that in these tests, unlike the compression cases, two stages of impedance mismatch occur; one, between the sample and the bars (because of the change in the speed of sound and the density), and, at the notch (because of the change in the cross-sectional area). This gives rise to complications in using the Hopkinson bar equations, which were discussed before.

6.2.2 Strain rate and stress rate

As discussed before, the use of the Hopkinson bar equations to calculate the rate of strain in the sample does not yield accurate results; however, they can be used to approximate the strain rate for comparative purposes. In this section,

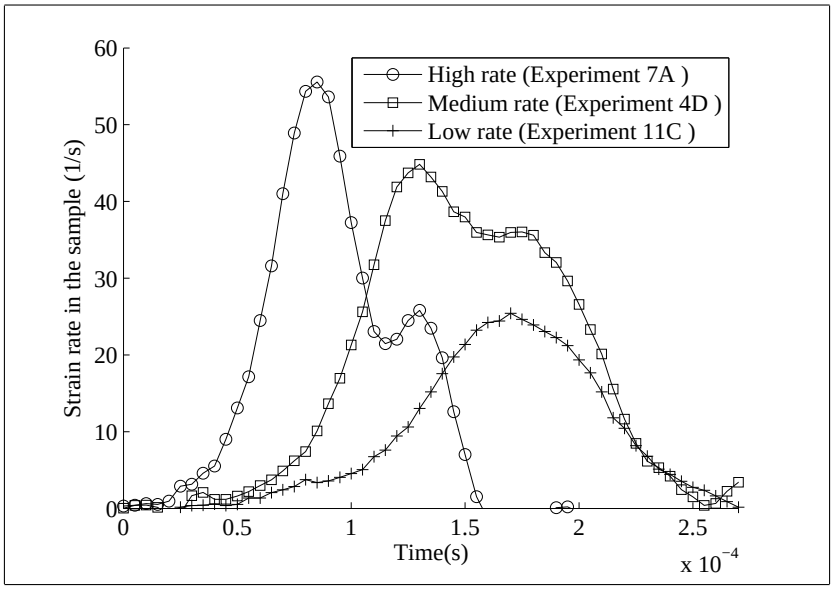

Figure 6.15: Strain-rates under which the samples were loaded in tension tests.

for the sake of comprehensiveness, we present some results containing strain rates.

Figure (6.14) contains the three tension pulses generated in the incident bar. The length and impact velocity of the striker tube were varied to create three different deformation rate levels in the samples. In figure (6.15), the time histories of the approximate strain rates are plotted.

The stress measurement in tension tests is more accurate; therefore, stress rate can be calculated from the linear part of the stress time history as a more reliable metric for comparing different cases.

6.2.3 Experimental results

In this section, the experimental results of the tension tests are presented. In figure (6.16), the stress-strain curves for all the tension tests are plotted. Unlike the compression case, the curves can not be distinguished into three separate groups. Little correlation can be observed between the maximum stresses and the

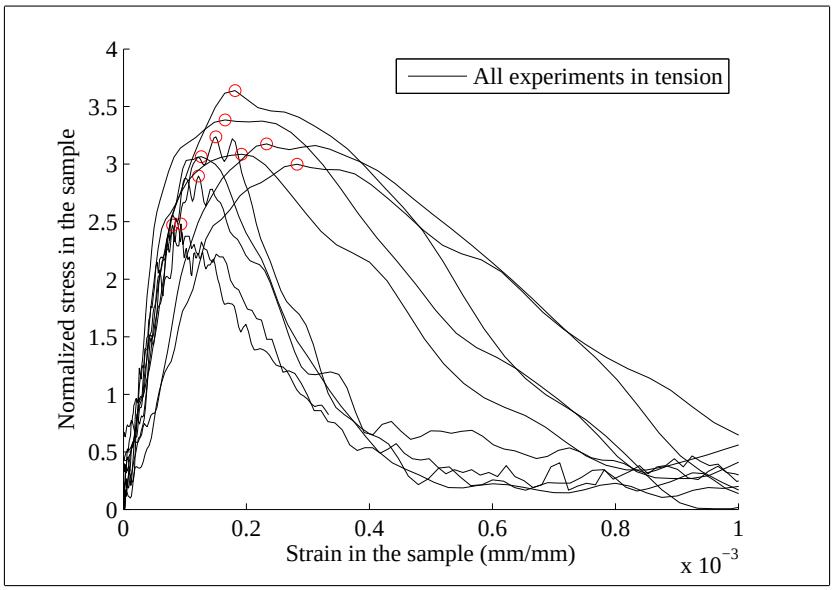

Figure 6.16: Tension test results

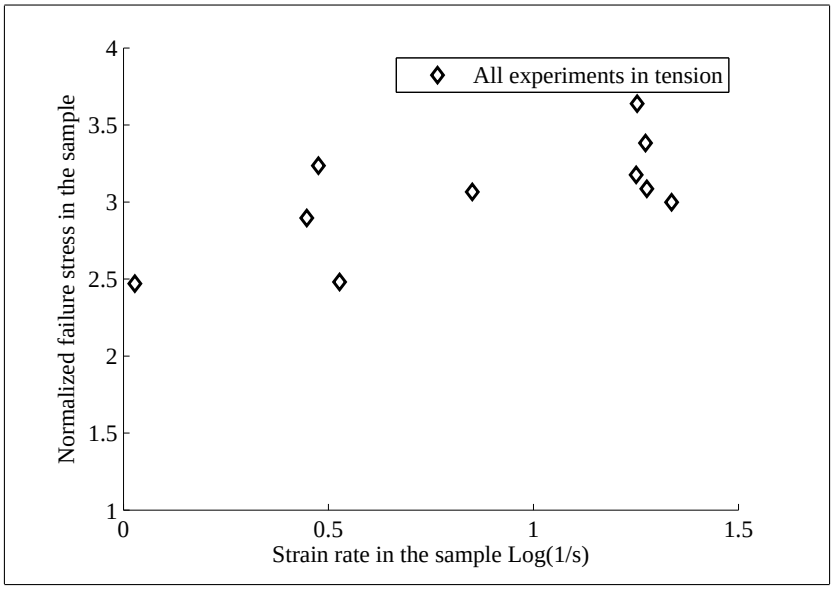

Figure 6.17: Concrete strengthening with rate in tension

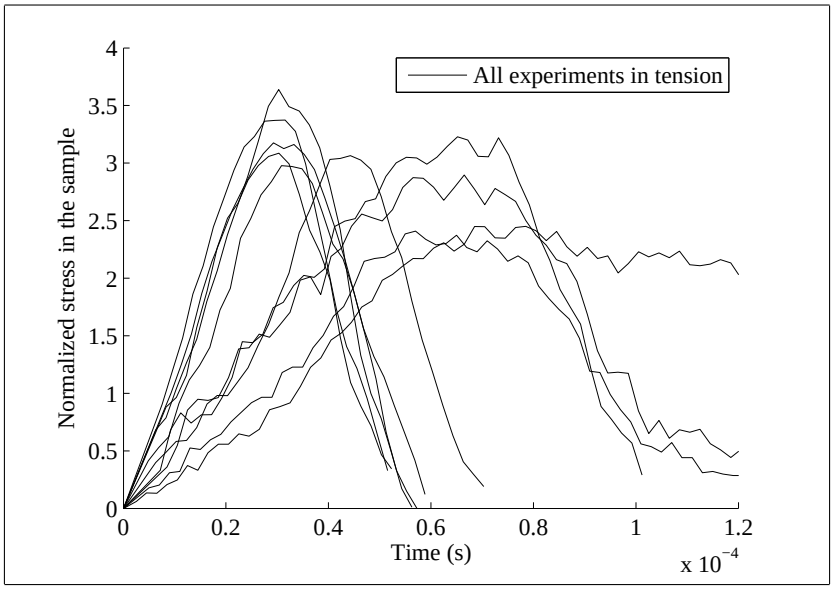

Figure 6.18: Stress versus time in tension

approximate strain rates at the times of failure (figure 6.17).

In figure (6.18), the time histories of stress experienced by tension samples are presented. The linear part of each curve is used to measure the stress rate for each case. Subsequently, the stress at the time of failure is plotted versus the stress rate. Figure (6.19) demonstrates that the strength of the concrete is increased under higher stress rates.

6.3 Finite Element Model

A 3-dimensional finite element model is developed to numerically simulate the experiments in both compression and tension. The objectives of this numerical study is summarized as below:

- Exploring the effect of sample size on the validity and accuracy of the the Hopkinson bar equations, which are employed to obtain the stress-strain

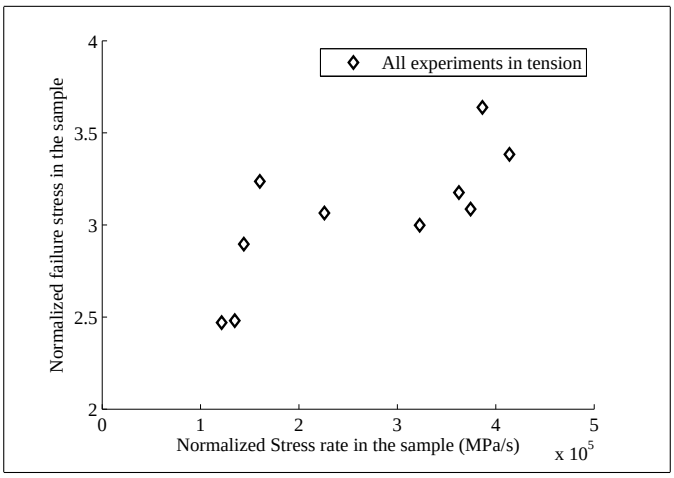

Figure 6.19: Concrete strengthening with stress rate in tension

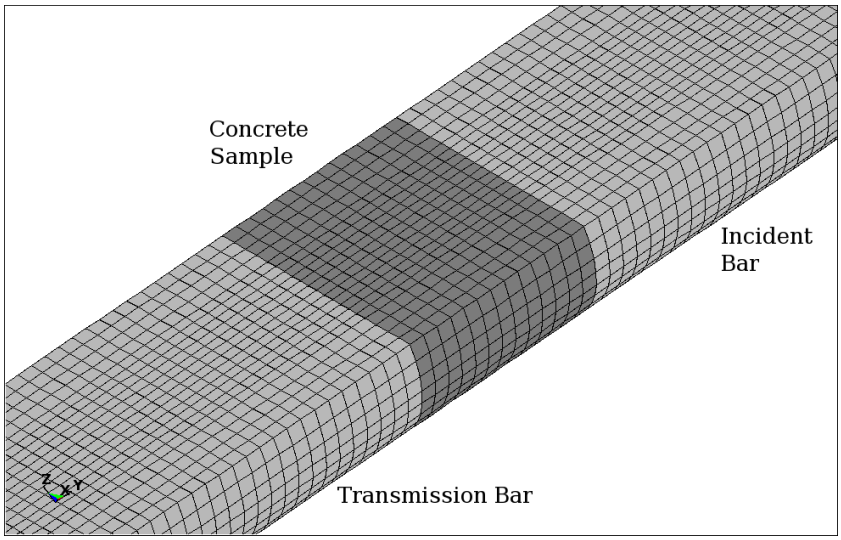

Figure 6.20: Finite element mesh for compression; for illustration purposes, the model is split in half. The model only contains 8-node brick elements.

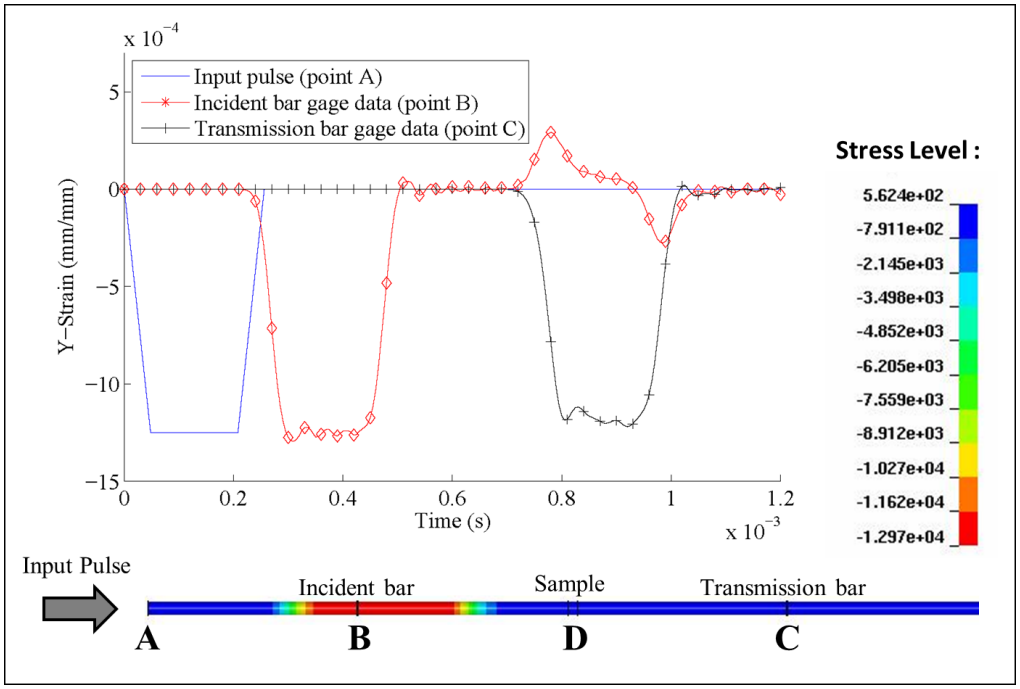

Figure 6.21: The numerical results from the finite element simulations: The trapezoidal pressure pulse (blue solid line) is applied to point **A**. Red line with diamond markers corresponds to stress history at point **B**, where the strain gage on the incident bar is located. Black line with plus markers corresponds to stress history of point **C**, where the strain gage on the transmission bar is located. The colored bar at the bottom, illustrates a snap shot of the y-strain in the bar at $t = 399.7\mu s$. The location of the pulse on the bar at that instant can be identified as the red region. Note that the sample is located at point **D**.

curves from the experimental data.

- Investigating the effect of friction at the sample-bar interfaces on the compression tests and the role of lubricating the interfaces.

- Comparing the experimental and numerical results to improve the current concrete material model.

The model consists of three parts: incident bar, sample and transmission bar. All the elements are 8-node brick elements (figure (6.20)). The finite element

meshes are refined to achieve a mesh-size independent solution. Contact surfaces are defined between the bars and the sample. Instead of using a striker bar, the input pulse is manually applied as a pressure pulse on the incident pulse. Elastic material models are used for Aluminum bars. For concrete, the material model developed by Karagozian and Case (K&C) is employed. This material model incorporates failure and strain rate effects into the finite element calculations [47].

6.3.1 Sample size effect

Here, the experimental process is duplicated by the finite element model. Material properties of a generic concrete is inputted to the (K&C) concrete material model. A trapezoidal pressure pulse is applied to the incident bar. The strain histories of the elements located at the position of the gages are numerically calculated. This data is used to calculate the stress and strain histories by employing the Hopkinson bar equations, mimicking the post-processing of the experimental data. This result is then compared with the actual stress and stain histories inside the sample, which is available from the finite element simulations. In these simulations, the friction between the sample and the bars is neglected.

In figure (6.21), the results from the finite element simulations are presented. The trapezoidal pressure pulse (blue solid line) is applied to point **A**. The stress history is measured at points **B** and **C**, where the strain gages are located. Red line with diamond markers corresponds to the strain gage on the incident pulse. Note that the shape of the pulse changes traveling from point **A** to **B**. The reflected and transmitted pulses, which are used to find the stress and strain histories in the sample from the Hopkinson bar equations, are also shown.

In figure (6.22), two stress-strain curves are plotted, which are derived in two different ways: (1) red line with '$\times$' markers, from an element at the center

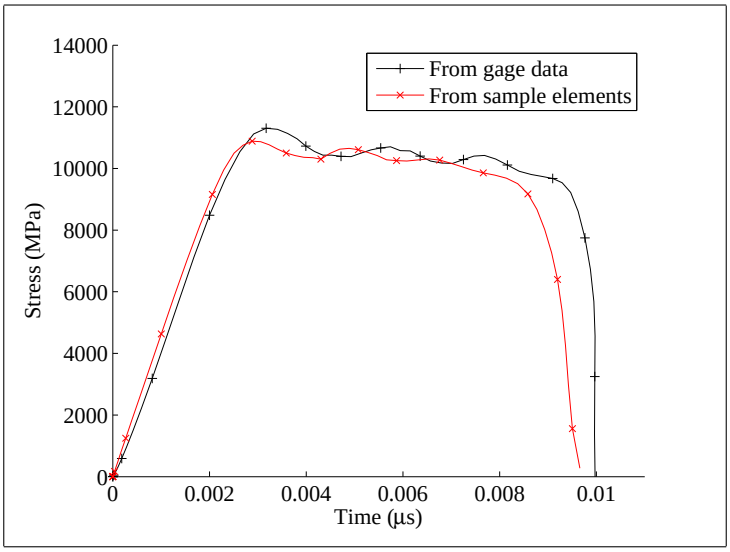

Figure 6.22: The strain-strain curves obtained from the experimental data

of the sample; (2) black line with '+' markers, from the Hopkinson bar equations, using the strain histories of the elements at the locations of the strain gages. The numerical results suggest that the sample size effect is not a major issue if the friction is minimal.

6.3.2 Friction effect

From finite element results, it is observed that in the absence of friction, the strain history is fairly equal in the elements of a given cross-section, both in the sample and in the bars. However, when a high friction exists at the interfaces between the sample and the bars, the elements of a given cross-section in the sample experience different stress and strain histories.

In figure (6.23), a section of the sample is shown, and 9 elements are chosen form different locations in the sample. In figure (6.24), the solid lines present the stress-strain curves for the elements shown in figure (6.23). The dotted line is the

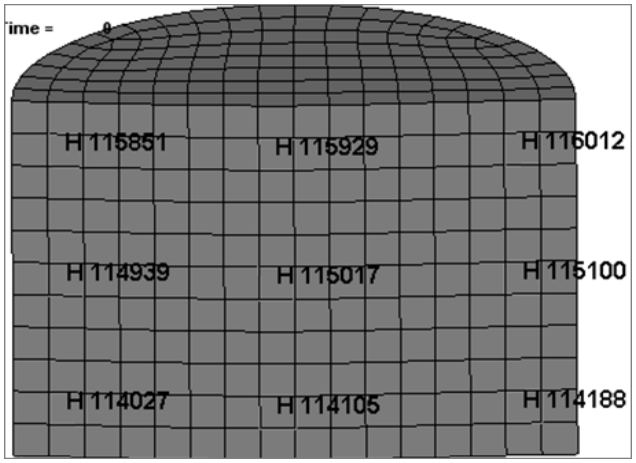

Figure 6.23: 9 elements in the compression sample are chosen. In figure (6.24), the stress-strain curves for these elements are plotted.

strain-stress curve obtained by applying the Hopkinson bar equations to the strain histories of the elements located at the position of gages. Significant differences between the strain-stress curves of different elements are observed. High friction between the interfaces leads to unreliable results; therefore, proper lubrication is necessary for compression tests.

6.4 Dispersion Correction in SHPB and Experimental Verification

In this section[1], the dispersion phenomenon in cylindrical solid bars is reviewed, and the process of dispersion correction is discussed in detail. Here, we are aiming for the analytical solution of the propagation of longitudinal waves in elastic cylindrical bars. We start with the conservation of linear momentum in a

[1]The notations and most of the equations in this section is adopted from "Stress Waves in Solids" by H. Kolsky (1963).

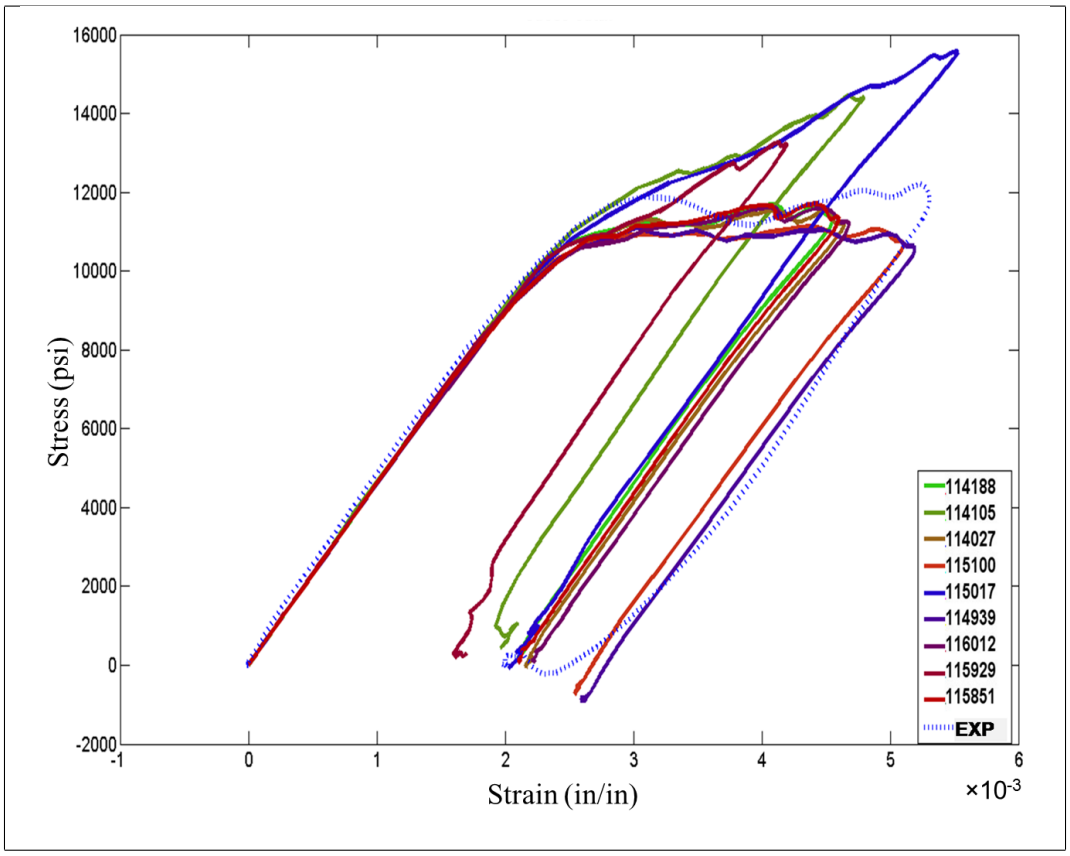

Figure 6.24: The effect of sample-bar friction: the strain-strain curves for the elements shown in figure (6.23) are plotted (solid lines). The dotted line is the stress-strain curve obtained from Hopkinson bar equations using the data from the elements at the strain gages positions. These plots suggest a non-uniform state of deformation throughout the sample when the friction is significant at the bar-sample interface.

continuum:

$$\sigma_{ij,j} + \rho f_i = \rho \dot{v}_i \tag{6.4}$$

For an elastic medium, equation (6.4) reduces to:

$$\sigma_{ij} = C_{ijkl}\varepsilon_{kl} \tag{6.5}$$

where C_{ijkl} is *one* component of the symmetric fourth order *elasticity tensor*, $\mathbf{C}$.

For isotropic elastic solids, equation (6.5) reduces to:

$$\sigma_{ij} = \lambda \varepsilon_{kk}\delta_{ij} + 2\mu\varepsilon_{ij} \tag{6.6}$$

where λ and μ are Lamé constants, and δ_{ij} is the Kronecker delta. In the absence of body forces and thermal effects and for infinitesimal strains $\varepsilon_{ij} = (u_{i,j} + u_{j,i})/2$, equation (6.4) becomes:

$$\mu u_{i,ji} + (\mu + \lambda) u_{i,ij} = \rho \ddot{u} \tag{6.7}$$

$$\text{or} \qquad \mu \nabla^2 \mathbf{u} + (\lambda + \mu)\boldsymbol{\nabla}(\boldsymbol{\nabla} \cdot \mathbf{u}) = \rho \ddot{\mathbf{u}} \tag{6.8}$$

By applying *divergence* ($\boldsymbol{\nabla}\cdot$) and *curl* ($\boldsymbol{\nabla}\times$) operations on both sides of the equation (6.8) two wave equations can be obtained,

$$\nabla^2(\boldsymbol{\nabla} \cdot \mathbf{u}) = \frac{1}{c_1^2}\frac{\partial^2(\boldsymbol{\nabla} \cdot \mathbf{u})}{\partial t^2} \tag{6.9}$$

$$\nabla^2(\boldsymbol{\nabla} \times \mathbf{u}) = \frac{1}{c_2^2}\frac{\partial^2(\boldsymbol{\nabla} \times \mathbf{u})}{\partial t^2} \tag{6.10}$$

where,

$$c_1^2 = \frac{\lambda + 2\mu}{\rho}\ , \ \ c_2^2 = \frac{\mu}{\rho} \tag{6.11}$$

c_1 and c_2 are the speeds of *dilatational or equivoluminal* and *shear or irrotational* waves, respectively. The problem of wave propagation in an infinite elastic bar was first investigated by Pochhammer (1876) and independently by

Chree (1989). The problem is formulated in cylindrical coordinates (r, θ, z). In the case of Hopkinson bar tests, the problem becomes axi-symmetric, for which u_r and u_z are not functions of θ, and u_θ vanishes. We consider the propagation of harmonic waves for which the displacements, u_r and u_z are harmonic functions of z and time:

$$u_r = Ue^{i(pt+\gamma z)} \quad \text{and} \quad u_z = Ze^{i(pt+\gamma z)} \tag{6.12}$$

where U and Z are functions of r. As a result, $p/2\pi$ is the frequency of waves with wavelength of $2\pi/\gamma$. The wave velocity is then, $c = p/\gamma$. If the wave equations (6.9) and (6.10) are written in cylindrical coordinates and the axi-symmetric assumption is applied, we obtain,

$$\frac{\partial^2 \Delta}{\partial r^2} + \frac{1}{r}\frac{\partial \Delta}{\partial r} + h^2\Delta = 0 \tag{6.13}$$

$$\frac{\partial^2 \omega_\theta}{\partial r^2} + \frac{1}{r}\frac{\partial \omega_\theta}{\partial r} - \frac{\omega_\theta}{r^2} + k^2\omega_\theta = 0 \tag{6.14}$$

where, Δ is the dilatation in cylindrical coordinates, and ω_θ is the rotation about θ-axis,

$$\Delta = \frac{1}{r}\frac{\partial (ru_r)}{\partial r} + \frac{1}{r}\frac{\partial u_\theta}{\partial \theta} + \frac{\partial u_z}{\partial z} \qquad and \qquad 2\omega_\theta = \frac{\partial u_r}{\partial z} - \frac{\partial u_z}{\partial r} \tag{6.15}$$

and h and k are given by:

$$h^2 = \rho p^2/(\lambda + 2\mu) - \gamma^2 \qquad and \qquad k^2 = \rho p^2/\mu - \gamma^2 \tag{6.16}$$

Substituting equations (6.12) into (6.13) and (6.14) yields two second order partial differential equations for U and Z, which fall into Bessel problem category and can be easily solved. The emerging constants can be found by substituting U and Z into the boundary condition equations, which in this case are:

$$\sigma_{rr} = \lambda\Delta + 2\mu\frac{u_r}{r} = 0 \qquad at\ r = a \tag{6.17}$$

$$\sigma_{r\theta} = \mu\left[\frac{\partial u_r}{\partial z} + \frac{\partial u_z}{\partial r}\right] = 0 \qquad at\ r = a \tag{6.18}$$

where a is the radius of the bar. Applying these boundary conditions to the solution results in the following algebraic equations:

$$A\left[2\mu\frac{\partial^2 J_0(ha)}{\partial r^2} - \frac{\lambda}{\lambda+2\mu}p^2\rho J_0(ha)\right] + 2B\mu\gamma\frac{\partial J_1(ka)}{\partial r} = 0 \tag{6.19}$$

$$2A\gamma\frac{\partial J_0(ha)}{\partial r} + B\left(2\gamma^2 - \frac{p^2\rho}{\mu}\right)J_1(ka) = 0 \tag{6.20}$$

where A and B are constants. The non-trivial solution of these equations is an algebraic equation, which involves the frequency and wavelength of the harmonic wave, the elastic constants λ and μ, the density ρ and the radius of the bar a. This equation is known as the *frequency equation*. This result indicates that in an infinite elastic bar, harmonic waves with different frequencies travel with different velocities.

Bancroft [91] has given the solution of the frequency problem as a function of wavelength and wave speed for different Poisson's ratios. Here, we numerically solve the frequency equation and find γ with respect to p. Having the radius and material properties of the bar, the frequency equation is solved to obtain the relationship between the wavelength and frequency. Figure (6.25) compares the Bancroft's solution to our numerical results for the Poisson's ratio of 0.3 and two different bar diameters. This result is significant as it explains the common phenomenon of *dispersion* is solid bars. This phenomenon can be seen figure (6.26). In this figure the time-history of the strain is given at four different points on the bar. Notice that only one pulse is traveling in the bar, but for illustration purposes it is plotted four

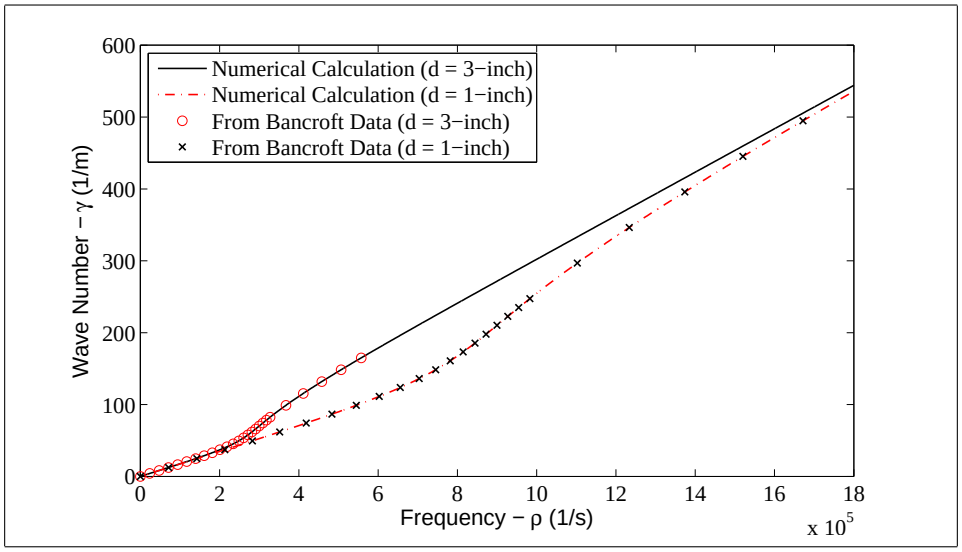

Figure 6.25: The solution of frequency equation for Poisson's ratio 0.3 and two different bar diameters

times on the same plot and at different locations. Nevertheless, the time axis is correct. Note that the shape of the pressure pulse changes as it propagates along the bar. We consider the initial pulse as an infinite sum of harmonic waves. Having different velocities, these waves arrive at a different point on the bar at different times. Consequently, the terms of the corresponding infinite sum at that point are phase shifted. These shifts can be calculated from the frequency equation for any given frequency. Therefore, by having the time-history of a pressure pulse at one point in a solid bar, the shape of the wave can be obtained at any other point by this shifting process, which is known as *dispersion correction*.

We developed a dispersion correction routine in Matlab and verified it by comparing to experimental results. The process is straightforward. For a given pulse, $\mathbf{v}$, and a distance x_0:

- The Fast Fourier Transform (FFT) of the given pulse is calculated, $\mathbf{v}_f = \text{fft}(\mathbf{v})$.

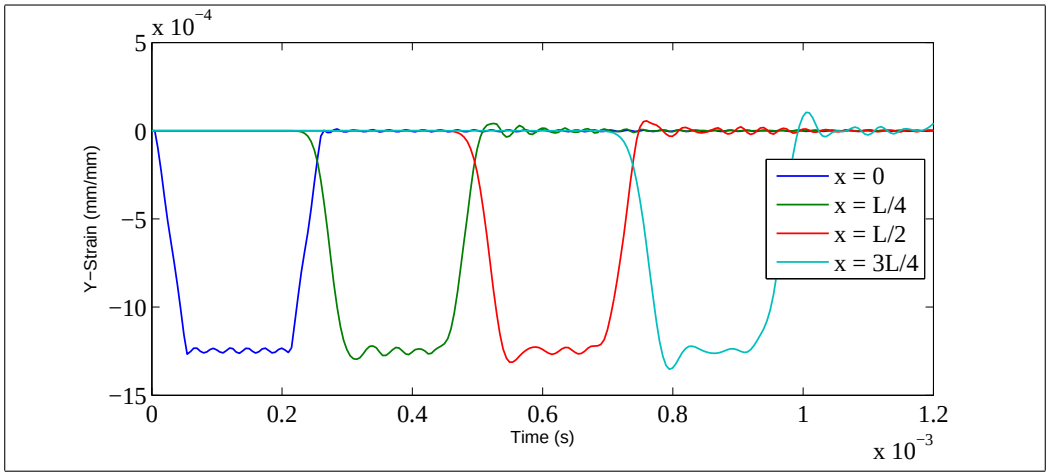

Figure 6.26: Dispersion of waves in an elastic solid bar with the diameter of 3-inch and Poisson's ratio of 0.34

- For each frequency, the phase is properly modified. Assume that the j^{th} element of the vector in Fourier space is

$$\mathbf{v_f}^j = a_j + ib_j \Longrightarrow \phi_j = tan^{-1}(b_j/a_j) \tag{6.21}$$

The frequency associated with the j^{th} component of $\mathbf{v}_f$ is

$$p = \frac{2\pi}{T_{span}}(j-1)$$

where T_{span} is the duration of the pulse. Having the frequency, we can solve the frequency equation and find the corresponding wavelength and γ. The new phase (angle) at a distance x_0 can be evaluated,

$$\phi_j^{new} = \phi_j + \gamma x_0$$

and finally the real and imaginary parts of $\mathbf{v}$ are corrected such that the magnitude remains unchanged:

$$\mathbf{v}_f^j = \sqrt{a^2+b^2}\; e^{i\phi_j^{new}} \tag{6.22}$$

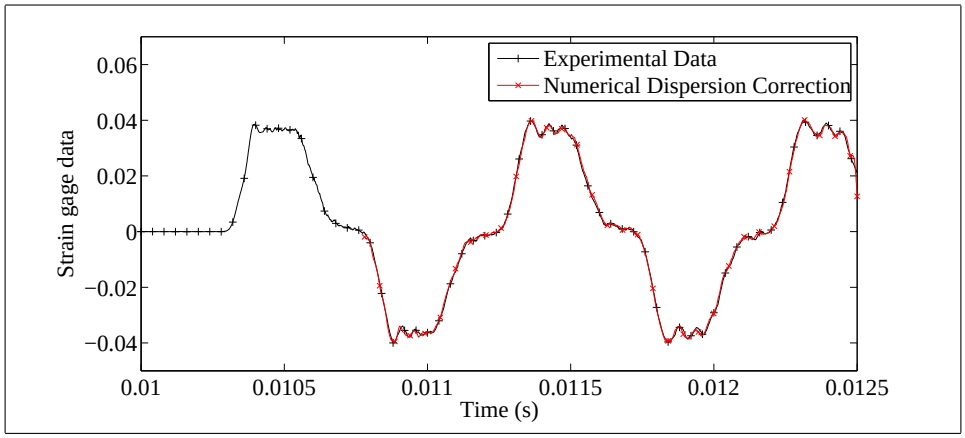

Figure 6.27: Dispersion correction verification - experimental vs. analytical

- An Inverse Fast Fourier Transform (IFFT) is performed on the updated $\mathbf{v}_f$ to obtain the pulse shape at x_0.

In figure (6.27), a pressure pulse from a Hopkinson bar experiment and the dispersion corrected version of that pulse are presented. The pulse is the strain history at the mid-length of a free-ended 96-inch aluminum bar (the incident bar of a Hopkinson bar setup). After the striker impacts the incident bar, it generates a compression wave which travels through the bar and passes the strain gage (first pulse) and is reflected as tension from the free end of the bar making the second pulse. This reflection process continues numerous times before the pulse is damped. The distance traveled by the pulse between two subsequent passings from strain gages is 96-inch. In figure (6.27), the red curve with cross markers is the dispersion corrected version of the input pulse. There is a remarkable match between the experimental and analytical results. Also, this plot verifies the accuracy of our dispersion correction routine.

6.5 Conclusions

A set of high strain rate compression and tension tests on concrete samples were performed, and stress-strain curves were generated from the experimental results. The accuracy and validity of the generated strain-stress curves were explored by a full-scale finite element model. The sample size and friction effects were investigated. A dispersion correction routine was developed and validated by comparing to experimental results.

6.6 Acknowledgments

The experimental work has been conducted at the Center of Excellence in Advanced Materials (CEAM), Mechanical and Aerospace Engineering Department, University of California, San Diego, by the author and Mr. Jon Isaacs, and has been supported by Karagozian & Case Company. The author gratefully acknowledges Mr. J. Magallanes for his contributions to this project. This chapter is prepared for publication by A. Samiee, J. Isaacs, J. Magallanes and S. Nemat-Nasser.

Appendix A

The Procedure of Steel-Polyurea-Steel Experiments

In this appendix, we explain in detail, the methods and instructions to perform blast experiments on steel-polyurea-steel sandwich structures, using a 3-inch Hopkinson Bar in the high-strain rate lab at CEAM/UCSD. These experiments involve a high pressure gas gun and a high-velocity striker, which can be potentially hazardous if not exercised with extreme caution. The major concern in this process is safety; all the guidelines must be followed very closely, carefully and slowly.

A.1 Preparation

To perform these experiments the following components must be prepared and functional. The operator(s) must put on proper footwear covering the entire foot. Sandals and flip-flops are not acceptable.

- Safety goggles and ear muffs.
- Lab book: Should contain enough information about the experiment so that

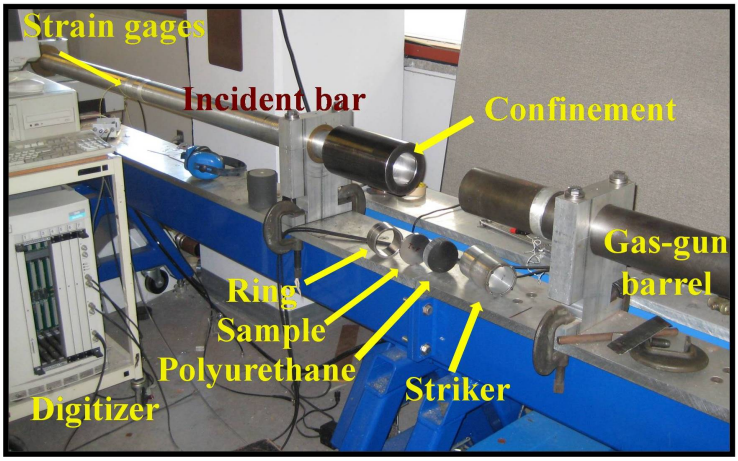

Figure A.1: Hopkinson Bar Setup

the process may be repeated by others in the future. It should indicate where the data is stored, and should have a qualitative description of experimental outcome. The list of the items written in the lab book for these experiments is presented at the end of section A.3.

- Hopkinson Bar: These experiments are performed using a 3-inch Split-Hopkinson Pressure Bar (SHPB). SHPB consists of the following components which are shown in figure (A.1):

  1. Incident bar
  2. Transmission bar
  3. Gas gun
  4. Barrel
  5. Four strain-gages on the bars
  6. Two magnetic coils to measure the velocity of the striker

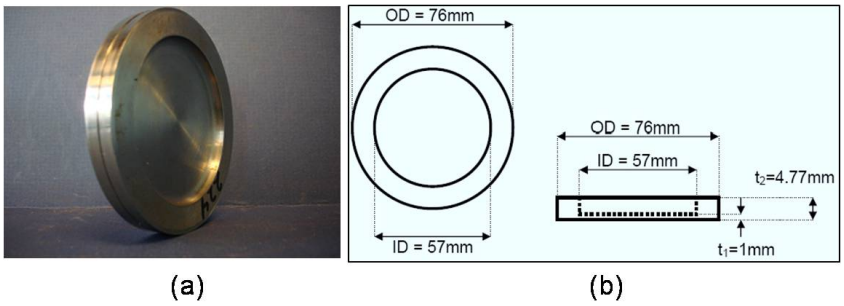

Figure A.2: Sandwich sample geometry

- Digitizer: Output signals from strain gages and magnetic coils are measured and digitized by a Nicolet digitizer. The digitizer is triggered by the signal arriving from the first magnetic coil.

- Nitrogen tank: To pressurize the gas gun up to 200psi.

- Sample: The sample may be a monolithic circular steel plate, a steel-polymer bi-layer or any combination of polymer-steel composite structure. Figure (A.2) illustrates a steel-polyurea-steel sandwich sample. It consists of two monolithic steel plates which are manufactured in a machine shop, consisting of a layer of polyurea cast between the plates. Note that at least two weeks are required for the polyurea to be completely cured.

- Confinement, ring and polyurethane piece: figure (A.1) illustrates the components which are used to place the sample in *the impact zone*. We define the impact zone as region in which the high-speed striker exits the Hopkinson Bar and collides with the polyurethane piece.

- A torque-meter is used to set the brakes in a repeatable and reliable manner.

A.2 Brief Description of the Experiment

The sample is sandwiched between the ring and the polyurethane piece inside the confinement. The confinement is placed on the incident bar and is positioned $\frac{1}{2}$ inch from the end of the barrel. The striker is slid inside the barrel to its position. Gas gun is pressurized to the desired pressure. The brakes are set, and the digitizer is made ready to record the data. Subsequently, the gas gun trigger is set off to accelerate the striker towards the sample through the barrel. The signal arriving from the magnetic coils and the strain gages on the incident bar are digitized and stored. Note that the transmission bar is not involved in these experiments.

A.3 Experiment Procedure

In this section, the experimental process is explained in detail. It is important to follow steps below very closely:

1. Ensure nothing is inside the barrel. This process should be done by two people. First, unscrew the barrel cap (figure A.3), remove it and place it aside. One person should look inside the barrel while the second person moves something visible at the other end of the barrel. Person one must ensure they can clearly observe the moving object at the other end of the barrel.

2. Place the sample in the confinement: Find the front side of the confinement which is marked by a red marker. First, slide the ring inside the confinement. Then, place the sample on the ring and push the polyurethane piece into the confinement, pressing onto the sample with a quarter of an inch clearance from the edge of the confinement. Figure (A.4) illustrates the exploded view

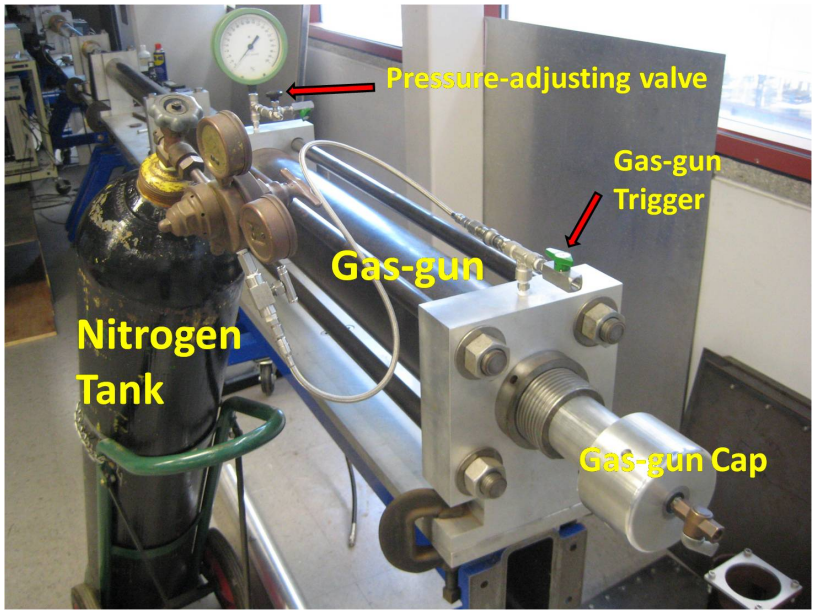

Figure A.3: Gas-gun components

of the components inside the confinement. Some samples might not slide into the confinement easily due to manufacturing issues. If that is the case, try to assemble the system from the back of the confinement which has a slightly larger diameter than the front side.

3. Place the confinement on the incident bar: Find the back side of the confinement and slide the incident bar inside the confinement until it is positioned behind the ring. A black marker can be found on the incident bar which indicates how far the incident bar should penetrate the confinement. When the confinement edge reaches the black marker, the sample is guaranteed to have been placed properly.

4. Adjust the incident bar position: Make use of a $\frac{1}{2}$ inch thick spacer. The space between the end of barrel and the confinement is determined by the spacer. A black arrow is drawn on the incident bar which should point to the

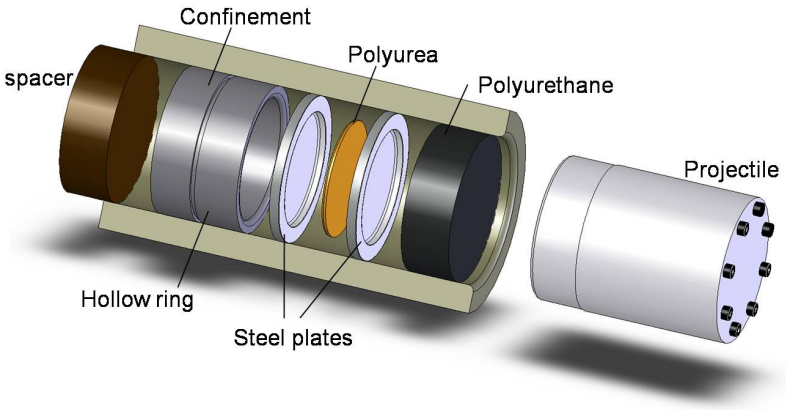

Figure A.4: Assembly of the components inside the confinement

edge of the front incident bar stanchion (or mount), when the incident bar is properly positioned.

5. Set the brakes to 25 lbf-in: Using the torque-meter shown in figure (A.5), fasten the bolts on the incident bar stanchion at the end of the bar to 25 lbf-in. Notice that the incident bar lies on two stanchions. The bolts form the stanchion which is furthest to the sample assembly should be fastened.

6. Place the metal cover on the impact area: The cover should be lifted by two people and placed on top of the area at which the impact takes place.

7. Strain gages are incorporated into a Wheatstone bridge which uses a constant 30.0 voltage on its ends. Use a voltmeter to check the output voltage of the power supplies used for Wheatstone Bridges on each bar.

8. Set the digitizer: The digitizer has to be pre-set by a competent operator for channel settings, signal levels, trigger options, etc. Continue with the following only when the digitizer is ready to function correctly. In the Nicolet

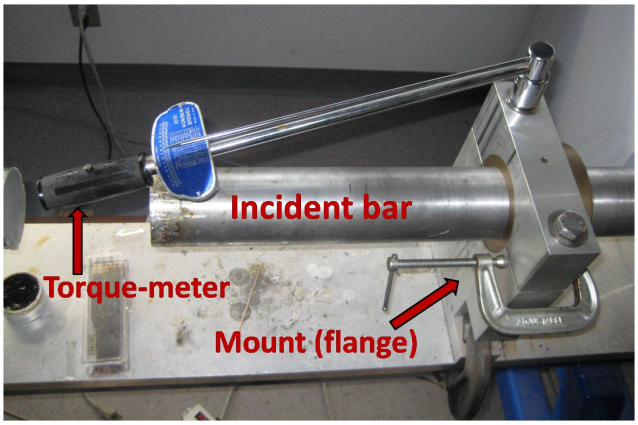

Figure A.5: Brake system and torque-meter

Windows, select the "one shot" option. To ensure that the system is ready, do a manual trigger by pressing Ctrl-T on the keyboard. By doing so, the "one shot" check-mark should disappear and the receiving signal should be flat without much noise and a reasonable voltage level, around zero. After this check, select the "one shot" option again. Now, green and yellow lights on the digitizer should be on. They should remain up until the impact.

9. Prepare the gas gun: Slide the striker inside the barrel and screw the barrel cap in position. Using the copper bar, push the striker to the second black mark on the copper bar. Close all the valves on the gas-gun and attach the nitrogen tank hose to the gas-gun as shown in figure (A.3).

10. Wear safety goggles and ear muffs.

11. Pressurize the gas tank: Double check the valves and ensure they are all closed. Open the nitrogen tank valve and pressurize the gas tank to desired pressure. You can adjust the pressure by using the valve on the pressure gauge.

12. IMPORTANT CHECK-LIST: Double check the following items before advancing to the next step:

    - Safety goggles and ear muffs.
    - Are brakes set?
    - Is the impact zone covered?
    - Are the green and yellow lights on the digitizer on?
    - Is the pressure level correct?
    - Is the striker positioned correctly by the copper bar?

13. Set off the trigger: At this point, everybody in the Lab must step away from the Hopkinson Bar and only the main operator remains next to the gas-gun. After ensuring that everybody in the lab has their safety goggles and ear muffs on, the main operator iterates the following loudly: "Firing... three... two... one!" and opens the green valve which acts as the trigger.

14. Right after the impact unscrew the gas-gun cap and remove it.

15. Save the data.

16. Release the brake by unscrewing the bolts of the incident bar stanchion.

17. Remove the cover from the impact zone and move the incident bar backwards in order to slide the confinement off. Remove the sample, ring and polyurethane piece from the inside of the confinement.

The experimental process is completed at this point. Note that all the major values and observations must be written carefully in the lab book. We write the following in the lab book for these experiments:

- Date
- Sample specifications (dimensions, weight, etc.)
- Striker weight
- Torque applied for the brake
- The folder in which the data is stored
- Time at which the coming signal from the first magnetic coil reaches its peak
- Time at which the coming signal from the second magnetic coil reaches its peak
- Final shape of the sample in terms of fracture

Bibliography

[1] Dennison Bancroft. The velocity of longitudinal waves in cylindrical bars. *Physical Review*, 1941:588–593, 1941.

[2] G.N. Nurick and J.B. Martin. Deformation of thin plates subjected to impulsive loading–a review part ii: Experimental studies. *International Journal of Impact Engineering*, 8(2):171 – 186, 1989.

[3] G.N. Nurick and J.B. Martin. Deformation of thin plates subjected to impulsive loading–a review: Part i: Theoretical considerations. *International Journal of Impact Engineering*, 8(2):159 – 170, 1989.

[4] G.I. Taylor. The distortion under pressure of a diaphragm which is clamped along its edge and stressed beyond its elastic limit. *Underwater Explosion Research, Vol. 3, The Damage Process, Office of Naval Research (1950)*, pages 107–121, 1942.

[5] J.M. Richardson and J.G. Kirkwood. Theory of the plastic deformation of thin plates by underwater explosions. *Underwater Explosion Research, Vol. 3, The Damage Process, Office of Naval Research*, pages 305–421, 1950.

[6] W.E. Baker. Approximate techniques for plastic deformation of structures under impulsive loading, shock. *Vibration Digest*, 7:107117, 1975.

[7] P. S. Symonds and T. Wierzbicki. Membrane mode solutions for impulsively loaded circular plates. *Journal of Applied Mechanics*, 46(1):58–64, 1979.

[8] S. Menkes and H. Opat. Broken beams. *Experimental Mechanics*, 13:480–486, 1973. 10.1007/BF02322734.

[9] R.G. Teeling-Smith and G.N. Nurick. The deformation and tearing of thin circular plates subjected to impulsive loads. *International Journal of Impact Engineering*, 11(1):77 – 91, 1991.

[10] Zhenyu Xue and John W. Hutchinson. Neck retardation and enhanced energy absorption in metal-elastomer bilayers. *Mechanics of Materials*, 39(5):473 – 487, 2007.

[11] M.R. Amini, J. Isaacs, and S. Nemat-Nasser. Investigation of effect of polyurea on response of steel plates to impulsive loads in direct pressure-pulse experiments. *Mechanics of Materials*, 42(6):628 – 639, 2010.

[12] M.R. Amini, J. Simon, and S. Nemat-Nasser. Numerical modeling of effect of polyurea on response of steel plates to impulsive loads in direct pressure-pulse experiments. *Mechanics of Materials*, 42(6):615 – 627, 2010.

[13] M.R. Amini, J.B. Isaacs, and S. Nemat-Nasser. Experimental investigation of response of monolithic and bilayer plates to impulsive loads. *International Journal of Impact Engineering*, 37(1):82 – 89, 2010.

[14] M.R. Amini, A.V. Amirkhizi, and S. Nemat-Nasser. Numerical modeling of response of monolithic and bilayer plates to impulsive loads. *International Journal of Impact Engineering*, 37(1):90 – 102, 2010.

[15] Liang Xue, Willis Mock Jr., and Ted Belytschko. Penetration of dh-36 steel plates with and without polyurea coating. *Mechanics of Materials*, 42(11):981 – 1003, 2010.

[16] Yehia A. Bahei-El-Din, George J. Dvorak, and Olivia J. Fredricksen. A blast-tolerant sandwich plate design with a polyurea interlayer. *International Journal of Solids and Structures*, 43(25-26):7644 – 7658, 2006.

[17] A. V. Amirkhizi, J. Isaacs, J. McGee, and S. Nemat-Nasser. An experimentally-based viscoelastic constitutive model for polyurea, including pressure and temperature effects. *Philosophical Magazine and Philosophical Magazine Letters*, 86:36:5847–5866, 2006.

[18] W. G. Guo Sia Nemat-Nasser. Thermomechanical response of dh- 36 structural steel over a wide range of strain rates and temperatures. *Mechanics of Materials*, 35:1023–1047, 2003.

[19] Sai Sarva, Sia Nemat-Nasser, Jeffrey McGee, and Jon Isaacs. The effect of thin membrane restraint on the ballistic performance of armor grade ceramic tiles. *International Journal of Impact Engineering*, 34(2):277 – 302, 2007.

[20] G.I. Taylor. The distortion under pressure of a diaphragm which is clamped along its edge and stressed beyond its elastic limit. *Underwater Explosion Research, Vol. 3, The Damage Process, Office of Naval Research (1950)*, pages 107–121, 1942.

[21] J.M. Richardson and J.G. Kirkwood. Theory of the plastic deformation of thin plates by underwater explosions. *Underwater Explosion Research, Vol. 3, The Damage Process, Office of Naval Research*, pages 305–421, 1950.

[22] S. K. Ghosh and H. Weber. Experimental-theoretical correlations of impulsively loaded asymmetric rigid-plastic membrane. *Mechanics Research Communications*, 3(5):423 – 428, 1976.

[23] S. R. Bodner and P. S. Symonds. Experiments on viscoplastic response of circular plates to impulsive loading. *Journal of the Mechanics and Physics of Solids*, 27(2):91 – 113, 1979.

[24] G.N. Nurick and J.B. Martin. Deformation of thin plates subjected to impulsive loading–a review part ii: Experimental studies. *International Journal of Impact Engineering*, 8(2):171 – 186, 1989.

[25] G.N. Nurick and J.B. Martin. Deformation of thin plates subjected to impulsive loading–a review: Part i: Theoretical considerations. *International Journal of Impact Engineering*, 8(2):159 – 170, 1989.

[26] W.E. Baker. Approximate techniques for plastic deformation of structures under impulsive loading, shock. *Vibration Digest*, 7:107117, 1975.

[27] P. S. Symonds and T. Wierzbicki. Membrane mode solutions for impulsively loaded circular plates. *Journal of Applied Mechanics*, 46(1):58–64, 1979.

[28] T. Wierzbicki and G. N. Nurick. Large deformation of thin plates under localised impulsive loading. *International Journal of Impact Engineering*, 18(7-8):899 – 918, 1996.

[29] Young-Woong Lee and Tomasz Wierzbicki. Fracture prediction of thin plates under localized impulsive loading. part i: dishing. *International Journal of Impact Engineering*, 31(10):1253 – 1276, 2005.

[30] Young-Woong Lee and Tomasz Wierzbicki. Fracture prediction of thin plates under localized impulsive loading. part ii: discing and petalling. *International Journal of Impact Engineering*, 31(10):1277 – 1308, 2005.

[31] V.H. Balden and G.N. Nurick. Numerical simulation of the post-failure motion of steel plates subjected to blast loading. *International Journal of Impact Engineering*, 32(1-4):14 – 34, 2005. Fifth International Symposium on Impact Engineering.

[32] A. Neuberger, S. Peles, and D. Rittel. Springback of circular clamped armor steel plates subjected to spherical air-blast loading. *International Journal of Impact Engineering*, 36(1):53 – 60, 2009.

[33] M.R. Amini, J. Isaacs, and S. Nemat-Nasser. Investigation of effect of polyurea on response of steel plates to impulsive loads in direct pressure-pulse experiments. *Mechanics of Materials*, 42(6):628 – 639, 2010.

[34] M.R. Amini, J. Simon, and S. Nemat-Nasser. Numerical modeling of effect of polyurea on response of steel plates to impulsive loads in direct pressure-pulse experiments. *Mechanics of Materials*, 42(6):615 – 627, 2010.

[35] M.R. Amini, J.B. Isaacs, and S. Nemat-Nasser. Experimental investigation of response of monolithic and bilayer plates to impulsive loads. *International Journal of Impact Engineering*, 37(1):82 – 89, 2010.

[36] M.R. Amini, A.V. Amirkhizi, and S. Nemat-Nasser. Numerical modeling of response of monolithic and bilayer plates to impulsive loads. *International Journal of Impact Engineering*, 37(1):90 – 102, 2010.

[37] C.M. Roland. *Rubber technologist's handbook*, volume 2. RAPRA, Shrewsbury, UK, 2007.

[38] Zhenyu Xue and John W. Hutchinson. Neck retardation and enhanced energy absorption in metal-elastomer bilayers. *Mechanics of Materials*, 39(5):473 – 487, 2007.

[39] A. V. Amirkhizi, J. Isaacs, J. McGee, and S. Nemat-Nasser. An experimentally-based viscoelastic constitutive model for polyurea, including pressure and temperature effects. *Philosophical Magazine and Philosophical Magazine Letters*, 86:36:5847–5866, 2006.

[40] W. G. Guo Sia Nemat-Nasser. Thermomechanical response of dh- 36 structural steel over a wide range of strain rates and temperatures. *Mechanics of Materials*, 35:1023–1047, 2003.

[41] S. Menkes and H. Opat. Broken beams. *Experimental Mechanics*, 13:480–486, 1973. 10.1007/BF02322734.

[42] R.G. Teeling-Smith and G.N. Nurick. The deformation and tearing of thin circular plates subjected to impulsive loads. *International Journal of Impact Engineering*, 11(1):77 – 91, 1991.

[43] W.G. Knauss. Vicoelastic material characterization relative to constitutive and failure response of an elastomer. *Interim Report to the Office of Naval Research*, CALTECH, Pasadena, CA, 2003.

[44] S. Nemat-Nasser and J.B. Isaacs. Direct measurement of isothermal flow stress of metals at elevated temperatures and high strain rates with application to ta and ta-w alloys. *Acta Mater*, 45:907–919, 1997.

[45] Sia Nemat-Nasser, Weiguo Guo, and Mingqi Liu. Experimentally-based micromechanical modeling of dynamic response of molybdenum. *Scripta Materialia*, 40(7):859 – 872, 1999.

[46] S. Nemat-Nasser and W.G. Guo. Flow stress of commercially pure niobium over a broad range of temperatures and strain rates. *Mater. Sci. Eng.*, 284:202–210, 1999.

[47] LSTC. *LS-DYNA keyword user's manual*. Livermore Software Technology Corporation, 2007.

[48] R.W. Ogden. *Non-Linear Elastic Deformation*. Ellis Horwood Ltd., Chichester, Great Britain, 1984.

[49] S. Nemat-Nasser, A. V. Amirkhizi, and J. Isaacs. Experimental characterization of polyurea. Technical report, CEAM Technical Report to ONR, Dec. 2003.

[50] C.M. Roland. *Rubber technologist's handbook*, volume 2. RAPRA, Shrewsbury, UK, 2007.

[51] Mahmoud Amini, Jon Isaacs, and Sia Nemat-Nasser. Effect of polyurea on the dynamic response of steel plates. *Proceedings of the 2006 SEM Annual Conference and Exposition on Experimental and Applied Mechanics*, 2006.

[52] W.G. Knauss. Vicoelastic material characterization relative to constitutive and failure response of an elastomer. *Interim Report to the Office of Naval Research*, CALTECH, Pasadena, CA, 2003.

[53] C.M. Roland, J.N. Twigg, Y. Vu, and P.H. Mott. High strain rate mechanical behavior of polyurea. *Polymer*, 48:574–578, 2007.

[54] Sai S. Sarva, Stephanie Deschanel, Mary C. Boyce, and Weinong Chen. Stress-strain behavior of a polyurea and a polyurethane from low to high strain rates. *Polymer*, 48(8):2208 – 2213, 2007.

[55] A.L. Florence. A theoretical study of the dynamic plastic behavior of beams and plates with finite deflections. *ASME Journal of Applied Mechanics*, 33:256–260, 1966.

[56] N. Jones. Clamped circular rigid-plastic plates under blast loading. *International Journal of Solids and Structures*, 7:1007–1029, 1971.

[57] Yehia A. Bahei-El-Din, George J. Dvorak, and Olivia J. Fredricksen. A blast-tolerant sandwich plate design with a polyurea interlayer. *International Journal of Solids and Structures*, 43:7644–7658, 2006.

[58] Z. Xue and J.W. Hutchinson. Neck retardation and enhanced energy absorption in metal-elastomer bilayers. *Mechanics of Materials*, 39:473–487, 2007.

[59] The Dow Chemical Company, Isonate 143L; Modified MDI (Dow Chemical, Midland, MI, 2001).

[60] Air Products Chemicals, Inc., Polyurethane Specialty Products (Air Products and Chemicals, Allentown, PA, 2003).

[61] G. Lee. Unpublished communication. pages Effect of processing temperature on dynamic and thermal properties Versathane, NSWC, Carderock, VA (2004).

[62] A. V. Amirkhizi, J. Isaacs, J. McGee, and S. Nemat-Nasser. An experimentally-based viscoelastic constitutive model for polyurea, including pressure and temperature effects. *Philosophical Magazine and Philosophical Magazine Letters*, 86:36:5847–5866, 2006.

[63] S. Menkes and H. Opat. Broken beams. *Experimental Mechanics*, 13:480–486, 1973. 10.1007/BF02322734.

[64] R.G. Teeling-Smith and G.N. Nurick. The deformation and tearing of thin circular plates subjected to impulsive loads. *International Journal of Impact Engineering*, 11(1):77 – 91, 1991.

[65] W. G. Guo Sia Nemat-Nasser. Thermomechanical response of dh- 36 structural steel over a wide range of strain rates and temperatures. *Mechanics of Materials*, 35:1023–1047, 2003.

[66] LSTC. *LS-DYNA keyword user's manual*. Livermore Software Technology Corporation, 2007.

[67] R.W. Ogden. *Non-Linear Elastic Deformation*. Ellis Horwood Ltd., Chichester, Great Britain, 1984.

[68] M.R. Amini, J. Simon, and S. Nemat-Nasser. Numerical modeling of effect of polyurea on response of steel plates to impulsive loads in direct pressure-pulse experiments. *Mechanics of Materials*, 42(6):615 – 627, 2010.

[69] M.R. Amini, J.B. Isaacs, and S. Nemat-Nasser. Experimental investigation of response of monolithic and bilayer plates to impulsive loads. *International Journal of Impact Engineering*, 37(1):82 – 89, 2010.

[70] Sai Sarva, Sia Nemat-Nasser, Jeffrey McGee, and Jon Isaacs. The effect of thin membrane restraint on the ballistic performance of armor grade ceramic tiles. *International Journal of Impact Engineering*, 34(2):277 – 302, 2007.

[71] S.J. Bless, Z. Rosenberg, and B. Yoon. Hypervelocity penetration of ceramics. *International Journal of Impact Engineering*, 5(1-4):165 – 171, 1987. Hypervelocity Impact Proceedings of the 1986 Symposium.

[72] Z. Rosenberg, E. Dekel, V. Hohler, A. J. Stilp, and K. Weber. Hypervelocity penetration of tungsten alloy rods into ceramic tiles: experiments and 2-d simulations. *International Journal of Impact Engineering*, 20(6-10):675 – 683, 1997. Hypervelocity Impact.

[73] P. Lundberg, L. Westerling, and B. Lundberg. Influence of scale on the penetration of tungsten rods into steel-backed alumina targets. *International Journal of Impact Engineering*, 18(4):403 – 416, 1996.

[74] D. L. Orphal, R. R. Franzen, A. C. Charters, T. L. Menna, and A. J. Piekutowski. Penetration of confined boron carbide targets by tungsten long rods at impact velocities from 1.5 to 5.0 km/s. *International Journal of Impact Engineering*, 19(1):15 – 29, 1997.

[75] D. A. SHOCKEY, A. H. MARCHAND, S. R. SKAGGS, G. E. CORT, M. W.BURKETT, and R. PARKER. Failure phenomenology of confined ceramic targets and impacting rods. *Ceramic transactions*, 134:385–402, 2002.

[76] R.L. Woodward, W.A. Gooch, Jr, R.G. O'Donnell, W.J. Perciballi, B.J. Baxter, and S.D. Pattie. A study of fragmentation in the ballistic impact of ceramics. *International Journal of Impact Engineering*, 15(5):605 – 618, 1994.

[77] D. R. Curran, L. Seaman, T. Cooper, and D. A. Shockey. Micromechanical model for comminution and granular flow of brittle material under high strain rate application to penetration of ceramic targets. *International Journal of Impact Engineering*, 13(1):53 – 83, 1993.

[78] The Dow Chemical Company, Isonate 143L; Modified MDI (Dow Chemical, Midland, MI, 2001).

[79] Air Products Chemicals, Inc., Polyurethane Specialty Products (Air Products and Chemicals, Allentown, PA, 2003).

[80] G. Lee. Unpublished communication. pages Effect of processing temperature on dynamic and thermal properties Versathane, NSWC, Carderock, VA (2004).

[81] S. M. Rytov. Acoustical properties of a thinly laminated medium. *Soviet Phys. Acoustics*, 2:68 – 80, 1967.

[82] G. A. Hegemier, G. A. Gurtman, and Adnan H. Nayfeh. A continuum mixture theory of wave propagation in laminated and fiber reinforced composites. *International Journal of Solids and Structures*, 9(3):395 – 414, 1973.

[83] H. Murakami, T.J. Impelluso, and G.A. Hegemier. Development of a mixture model for nonlinear wave propagation in fiber-reinforced composites. *International Journal of Solids and Structures*, 29(14-15):1919 – 1937, 1992.

[84] S. Nemat-Nasser, T. Iwakuma, and M. Hejazi. On composites with periodic structure. *Mechanics of Materials*, 1(3):239 – 267, 1982.

[85] S. Minagawa and S. Nemat-Nasser. Harmonic waves in three-dimensional elastic composites. *International Journal of Solids and Structures*, 12(11):769 – 777, 1976.

[86] S. Nemat-Nasser, F. C. L. Fu, and S. Minagawa. Harmonic waves in one-, two- and three-dimensional composites: Bounds for eigenfrequencies. *International Journal of Solids and Structures*, 11(5):617 – 642, 1975.

[87] S. Minagawa, S. Nemat-Nasser, and M. Yamada. Dispersion of waves in two-dimensional layered, fiber-reinforced, and other elastic composites. *Computers & Structures*, 19(1-2):119 – 128, 1984. Special Memorial Issue.

[88] R. M. Davies. A critical study of the hopkinson pressure bar. *Materials and Structures*, A240:375–457, 1948.

[89] M. Redwood. *Mechanical Waveguiedes; The propagation of acoustic and ultrasonic waves in fluids and solids with boundaries*, volume 2. Pergamon Press, London, UK, 1960.

[90] P.S. Folansbee. The hopkinson bar, mechanical testing. *ASM Handbook, American Society for Metals*, 8:198–203, 1985.

[91] Dennison Bancroft. The velocity of longitudinal waves in cylindrical bars. *Physical Review*, 1941:588–593, 1941.